ANALYTICAL AND EXPERIMENTAL STUDIES OF MODELING AND MONITORING UNCERTAIN NONLINEAR SYSTEMS

by

Hae-Bum Yun

A Dissertation Presented to the
FACULTY OF THE GRADUATE SCHOOL
UNIVERSITY OF SOUTHERN CALIFORNIA
In Partial Fulfillment of the
Requirements for the Degree
DOCTOR OF PHILOSOPHY
(CIVIL ENGINEERING)

August 2007

Dedication

to my family

Acknowledgments

First, I would like to thank to Professor Sami Masri, my advisor and the chair of my Ph.D. committee for his support and guidance in my study. In classrooms, he helped me set up secure foundation of knowledge. Out of classrooms, he showed me how a scholar should live his daily life. I was really honored to have a chance to work with him closely. I also would like to thank to my other Ph.D. committee members, Professors Carter Wellford, Roger Ghanem, Jiin-Jen Lee, and John Caffrey.

Professor John Caffrey deserves special thanks for his comments and assistance in my laboratory works. His expertise and genius on experimental study, which helped me become a more proficient experimentalist. Especially, he gave me many helps in building the magneto-rheological (MR) damper test apparatus (Chapter 5 in this thesis). I also would like to thank to Lance Hill, our supportive lab manager in civil and environmental engineering department.

I was blessed with having my excellent colleagues, Dr. Raymond Wolfe, Dr. Mazen Wahbeh, Dr. Farzad Tasbihgoo, Dr. Reza Nayeri, Dr. Elena Kallinikidou, Dr. Elena Kallinikidou, Miguel Hernandez, Mohammadreza Jahanshahi, and Reza Jafarkhani. We worked closely together on many interesting research topics, and the discussion with them was always inspirational and priceless.

I would like to thank to Professors Robert Nigbor and Ahmed Abdel-Ghaffar, and Li-Hong Sheng for their comments and co-authorship on the published journal paper of the forensic study of cargo ship collision with the Vincent Thomas Bridge (Chapter 6 in this thesis).

The assistance of Professor Nicos Makris and Dr. Cameron Black at the University of California, Berkeley, and Professor Gianmario Benzoni at the University of California, San Diego in the experimental tests using full-scale viscous dampers is appreciated. They are coauthors of the journal papers of the experimental studies using full-scale viscous dampers (Chapters 3 and 4 in this thesis).

The studies reported in this thesis were supported in part by grants from the National Science Foundation (NSF), the National Aeronautics and Space Administration (NASA), the Air Force Office of Scientific Research (AFOSR), and the California Department of Transportation (Caltrans).

Last, but not least, I would like to extend special thanks to my family for their supports and encouragement in completing this work. My parents, Ki-Tae and Byoung-Jin Yun, and my mother-in-law, Il-Jee Lee, have provided their endless supports through my study. Without their supports, I should not be able to fulfil this work. My sister and brother, Hea-Bin and Hae-Duk Yun, deserve my special thanks for their words of encouragement, especially when I was staggering with many burdens in this process. I would like to thank to David and Joy Yun, my son and daughter. Having them during my graduate study was the best memories in my life, and they gave me great pleasures during this long journey of study. Most of all, there is my wife, Myoung-Jae Yun. She has always stood beside me, supported me, and encouraged me. There

are so many things I have owed her since I met her eighteen years ago, and my doctoral degree is one of those many things.

Table of Contents

List of Tables

List of Figures

Abstract

The development of effective structural health monitoring (SHM) methodologies is imperative for the efficient maintenance of important structures in aerospace, mechanical and civil engineering. Based on reliable condition assessment, the owners of monitored structures can expect two important benefits: (1) to avoid catastrophic accidents by detecting various types of structural deterioration during operation, and (2) to establish efficient maintenance means and time schedule to reduce maintenance costs.

A vibration-based SHM methodology is evaluated for change detection in nonlinear systems that can be frequently seen in many engineering fields. The proposed methodology is advantageous over existing SHM methodologies regarding the following aspects: (1) feasible to detect small changes in complex nonlinear systems, (2) possible to make physical interpretation of detected changes, and (3) possible to quantify the uncertainty associated with the change detection.

A series of analytical and experimental studies was performed to investigate various important issues in modeling and monitoring of uncertain nonlinear systems. Different parametric and non-parametric identification methods were compared for monitoring purpose using full-scale nonlinear viscous dampers for seismic mitigation in civil structures. Then, the effects

of uncertainty on change detection performance were investigated. Two types of uncertainty were studied: measurement uncertainty (or measurement noise) and system characteristic uncertainty (or variation of system parameters). For measurement uncertainty, three different types of full-scale nonlinear viscous dampers were used to validate the proposed SHM methodology when the dampers' response was polluted with random noise. For system characteristic uncertainty, a semi-active magneto-rheological damper whose system characteristics were determined through user controllable input current was used. Statistical pattern recognition methods were studied to detect relatively small changes in nonlinear systems with different uncertainty types. The Bootstrap method, a statistical data resampling technique, was also studied to estimate the uncertainty bounds of change detection when the measurement data are insufficient for reliable statistical inference.

A web-based real-time bridge monitoring system was developed and used for a forensic study involving a cargo ship collision with the Vincent Thomas Bridge, a critical suspension bridge in the metropolitan Los Angeles region.

Keywords: structural health monitoring, system identification, Restoring Force Method, artificial neural networks, Hypothesis test, Bootstrap method, statistical pattern recognition, support vector machines, *k*-mean clustering, error analysis, detection theory, Natural Excitation Technique, Eigensystem Realization Algorithm, full-scale viscous dampers, magneto-rheological dampers, suspension bridge, web-based real-time bridge monitoring system, ship-bridge collision.

Chapter 1

Introduction

1.1 Motivation

The development of effective structural health monitoring (SHM) methodologies is imperative for the efficient operation and maintenance of important structures in aerospace, mechanical and civil engineering. With the capability of reliable condition assessment using modern sensing, data networking and data analysis techniques, the operation and maintenance of monitored structures can be improved in the following two ways:

1. To avoid catastrophic accidents by detecting various types of structural deterioration, modification or changes during the operation.

2. To establish efficient means and time schedules for structural maintenance or rehabilitation for the detected or predicted structural changes.

Consequently, the efficiency of SHM methodologies is directly related to the operational costs and safety of monitored systems, and many SHM approaches have been developed for various applications in different science and engineering fields. An example can be found in the *Integrated Vehicle Health Management* (IVHM) program developed by the National Aeronautics and Space Administration (NASA). Using advanced smart sensing, diagnostic and prognostic techniques, and multi-level management and maintenance planning algorithms, the goal of the IVHM systems is to provide both real-time and life-cycle vehicle health information for the second generation Reusable Launch Vehicle (RLV). Consequently, reliable and accurate SHM approaches play critical roles in the development of the IVHM. As shown in the tragedy of the space shuttle *Columbia*, the vehicles need to be monitored with an integrated array of onboard *in-situ* sensing systems rather than periodic, ground based structural integrity inspection (Mancini et al., 2006; Prosser et al., 2004). The health information of the vehicles is continuously updated for estimating critical failure modes as well as routinely updated for estimating life cycle condition trending (National Aeronautics and Space Administration, 2007). Moreover, in operating the space programs, the high program's total cost, which is largely influenced by the efficiency of the operation and maintenance procedures, would be one of the most substantial obstacles to the progress of space exploration (Schwabacher et al., 2002). The combination of continuous and routine assessments of the vehicles' healthiness could reduce the high operational costs through quicker vehicle turn-around (Aaseng, 2001).

Another example of the motivation for developing effective SHM methodologies can be seen in the maintenance of civil infrastructure system. Current practices of highway bridge inspection are based on the *National Bridge Inspection Program* (NBIP) (FHWA, 1972). Since 1972, the NBIP has been managed by the Federal Highway Administration (FHWA) to assess the "health" condition of major highway bridges in the U.S.A. However, because this method mainly relies on visual inspection methods by human inspection crews, the program's cost is expensive, and the inspection results could be subjective and inaccurate. Hence, in order to overcome the limitations of the existing NBIP, the *Long-Term Bridge Performance Program* (LTBP) was recently proposed by the FHWA and approved by the U.S. Congress in 2006 (FHWA, 2006).

The purpose of the LTBP is to develop predictive models for bridge performance and asset-management decision making over 20 years, utilizing powerful sensing, instrumentation, test, monitoring and evaluation techniques, which are available in these days.

A number of structural condition assessment approaches have been developed using modern sensing, communication and computing technologies (Housner et al., 1997). Among them, *vibration-based* structural health monitoring techniques have been employed as promising condition assessment approaches. For numerous applications of critical structures in many engineering fields, numerous modeling approaches have been proposed worldwide to identify the monitored structures using the structures' dynamic response measured with advanced sensing and data acquisition techniques (Fujino et al., 2004; Housner et al., 1997; Ou, 2004; Ou and Li, 2004; Paik et al., 2004; Rodellar, 2004; Spencer and Yang, 2004; Tachibana and Mita, 2006; Yun, 2006). However, none of the proposed methods can become universally applicable to detect various modes and types of changes in complicated, monitored structures due to many limitations. For successful SHM, the developed SHM methodologies should possess the following important features:

1. (Detectability of system changes): Various types and modes of structural changes should be detectable. The monitored structures are frequently complex nonlinear systems. Due to structural deteriorations or changes, the structural characteristics vary over time (i.e., the structures are *time-varying* systems). In general, these changes involve not only the *changes of system parameter values*, but also the *transformation (evolution) into different classes of nonlinear systems*. Unfortunately, the analytical models of the transformed systems are commonly unknown. If the monitored structures are complex nonlinear systems,

then *model-order reduction* would be necessary, especially when the exact system models are unknown, or when the rapid computation time is a significant concern.

2. (Physical interpretations): Although the feasibility of change detection in nonlinear time-varying systems is very important, it is not the only objective for successful SHM. In order to establish effective operation and maintenance strategies for the monitored structures, it is necessary to interpret the physical meanings of the detected changes. Consequently, structural engineers should be provided with some *engineering-based* guidelines to effectively deal with the detected changes. The physical interpretations should involve (1) estimating the effects of the detected changes on the structural "healthiness", at the full-structure level as well as at the component level, (2) characterizing the possible causes of the changes, and (3) locating the changed (or damaged) parts in the entire structures.

3. (Uncertainty quantification): The uncertainty quantification of the detected changes should be possible since the dynamic response of monitored structures are usually influenced by various sources of uncertainty. In general, there are two types of uncertainty affecting the change detection performance: (1) measurement uncertainty of the system response, and (2) system characteristics uncertainty. Since the *measurement uncertainty* is due to various types of noise in the data acquisition processes, this uncertainty is often time-uncorrelated (i.e., white noise). On the other hand, the *system characteristics uncertainty* is often periodic and time-correlated (or colored noise) because this type of uncertainty is usually caused by structural characteristic changes due to various environmental effects, such as daily and yearly temperature changes. Using SHM techniques, it should

be possible to distinguish genuine structural change detection from "noisy" detection, and to estimate the *uncertainty bounds* (or *confidence intervals*) of the detected changes.

As discussed above, developing reliable and practical SHM methodologies is extremely challenging, and, consequently, few current approaches satisfy those requirements. Common limitations of current SHM methodologies include:

1. The system models are over-simplified. The over-simplification is usually made in the following two ways: (1) excessive model-order reduction for nonlinear systems, and (2) lack of knowledge of significant environmental effects. Obviously, these two simplications make the identification results inaccurate (Peeters et al., 2001; Seber and Lee, 2003). In the development of current SHM methodologies, however, the effects of model-order reduction on the corresponding change detection are rarely studied.

2. The modeling approaches are not robust enough to identify time-varying structures. In general, two types of modeling approaches are used in SHM applications: (1) parametric system identification methods and (2) non-parametric system identification methods. Because the modeling approaches of the *parametric identification methods* are based on some physical assumptions of the monitored structures, *a priori* knowledge of the structures is required. Consequently, if the structures change into other classes of nonlinear systems due to unexpected structural changes, the identification results using the "old" models become no longer accurate. The *non-parametric identification methods*, however, are more "flexible" than the parametric methods since the modeling processes of the non-parametric methods are data-driven, and no assumptions about the structures'

physical characteristics are required in its modeling process. Yun et al. (2007) experimentally demonstrated that the non-parametric modeling approaches are more advantageous in monitoring purposes than the parametric approaches.

3. Although current SHM methodologies adopting non-parametric system identification approaches (e.g., artificial neural networks, principal component analysis, etc.) allow detecting the changes in the structural characteristics, the physical interpretations of the detected changes are rarely possible. For the interpretation of the system changes, the parametric identification methods are more advantageous than the non-parametric methods since the identified parameters are usually directly related to the structures' physical characteristics (e.g., mass, spring constant and damping constant in linear lumped-mass vibration model). On the other hand, because the identification models of the non-parametric methods usually do not have direct relationships to the structural characteristics(e.g., weights and biases of the artificial neural networks), it is difficult to interpret the detected changes. Consequently, there exists a trade-off between parametric and non-parametric modeling approaches, and using current SHM methodologies overcome this trade-off, the trade-off can be rarely overcome.

4. Most of current SHM methodologies are deterministic, and the uncertainty bounds of the detected changes are seldom estimated. The estimation of the change detection uncertainty should include various effects of the measurement uncertainty and system characteristics uncertainty as discussed earlier.

1.2 Objectives

The objective of this study is to develop effective modeling and monitoring methodologies for assessing the healthiness of uncertain, nonlinear, dynamic systems. The developed methodologies are evaluated *analytically* and *experimentally* for complex nonlinear systems that can be frequently seen in the aerospace, mechanical and civil engineering fields.

Different vibration-based system identification methods are compared. For effective SHM, the modeling approaches should be able to identify complex nonlinear systems that change in time due to system deterioration, modification, or changes. Here, the system changes involve transformation into different classes of nonlinearities, as well as changes of system parameter values. In the SHM practice, since the system characteristics of the changed systems are usually unknown, the modeling approaches should not based on specific phenomenological models.

Once the changes are detected, physical interpretation should be made on the detected changes to establish effective strategies to deal with the detected changes. Consequently, the modeling approaches of the developed SHM methodologies should be model-independent, but still the physical interpretation of the detected changes should be possible.

For the uncertain response of the nonlinear systems affected by various types of randomness, not only the "genuine" changes of the system characteristics should be detectible, but also the uncertainty bounds on the change detection should be quantifiable. In addition, the quantified detection errors should be analyzed to improve the performance of the developed SHM methodologies.

1.3 Approaches

In order to achieve these research objectives in a logical fashion, a series of investigations were performed in this study, gradually introducing the complexities of the problems mentioned above by conducting the following studies:

1.3.1 Comparison of Modeling Approaches for Full-Scale Nonlinear Viscous Damper

Using a full-scale nonlinear viscous damper that is frequently employed to mitigate seismic and wind-induced vibration in civil structures, the results of a joint study between the University of Southern California (USC) and the University of California, Berkeley (UCB) are presented in this thesis. A series of tests is conducted at UCB with the viscous damper, and the obtained experimental data are analyzed at USC.

Different parametric and non-parametric identification methods are compared to achieve the following important research objectives: (1) to obtain quantitative data on full-scale tests, which are rarely available due to the damper's large size, (2) to obtain information on the accuracy and utility of various modeling approaches, (3) to compare the advantages and limitations of parametric and non-parametric models, (4) to study nonlinear features of full-scale viscous dampers, and (5) to study model dependency on the level of excitation.

1.3.2 Data-Driven Methodologies for Change Detection in Large-Scale Nonlinear Dampers with Noisy Measurements

Once different modeling approaches are compared, the effects of different types of uncertainties on the modeling fidelity of complex nonlinear systems must be investigated. Two types of uncertainties can be considered in the development of SHM methodologies: (1) measurement uncertainty, and (2) system characteristics uncertainty.

Among these two uncertainty types, the effects of measurement uncertainty are firstly investigated. In this experimental study, three different types of large-scale nonlinear viscous dampers are used to understand the various effects of the system nonlinearities on the damper identification results. Aiming for the model-independent change detection discussed in Section 1.2, the goal of this study is to develop a data-driven methodology for identifying various nonlinear viscous dampers.

A joint study is performed between the University of Southern California (USC), the University of California, San Diego (UCSD) and the University of California, Berkeley (UCB). The experimental results of the large-scale viscous dampers tested at UCSD and UCB are discussed. Using the experimental results, an analytical study is performed at USC. In this analytical study, the measured data are artificially polluted with random noise to investigate some aspects of the measurement uncertainty effects. Data-driven system identification methods are applied using the noisy data sets.

In general, the uncertainty quantification of the identification results requires multiple tests, which is not usually possible for *in-situ* monitoring, due to the lack of control of excitation sources. Even if one had the control of the excitation, performing multiple tests with large-scale viscous dampers would be extremely difficult because of the enormous amount of heat converted from the dissipated energy. Consequently, a statistical data recycling technique is studied for the uncertainty quantification, even with a limited number of data sets for the statistical inference.

1.3.3 Model-Order Reduction Effects on Change Detection in Uncertain Nonlinear Magneto-Rheological Dampers

Once the effects of measurement uncertainty are understood, the effects of system characteristics uncertainty should be also investigated. The objective of this study is to investigate various effects on modeling and monitoring nonlinear systems with uncertain system characteristics.

For achieving this objective, passive type viscous dampers used in previous studies cannot be used because a direct control of the dampers' physical characteristics is required for a known amount of "genuine" (or effective) system changes with a known quantity of system uncertainty. Consequently, a semi-active magneto-rheological (MR) damper is used in this study. Multiple sets of damper's response are obtained for Gaussian distributions of MR damper input currents with different means and standard deviations. Here, the mean of the distribution determines the effective system characteristics and the standard deviation of distribution determines the uncertainty of system characteristics.

In order to identify complex nonlinear systems, the model-order reduction of the identified systems is often necessary when the exact system models are unknown, or when a short computation time is an important concern. Hence, the effects of the model-order reduction on the system change detection should also be also studied.

Using powerful statistical pattern recognition and classification algorithms, the detectability of the "genuine" system changes with different levels of system characteristics uncertainties are studied. The classification errors of the change detection are analyzed, and a classifier design approach for the optimal change detection is proposed.

1.3.4 Monitoring the Collision of a Cargo Ship with the Vincent Thomas Bridge

In general, there are two different identification classes considered in vibration-based SHM: the *component-level* and *full structure-level* SHM. Once various important effects on the identification in uncertain nonlinear systems are investigated for developing the component-level SHM, the scope of this study should be expanded to the full structure-level SHM.

The Vincent Thomas Bridge (VTB), an important suspension bridge in southern California, was collided by a cargo ship in 2006. A web-based real-time continuous monitoring system installed on the bridge was successfully measured the bridge's dynamic response before, during and after the collision. Using the valuable data sets obtained, a forensic study is performed to assess the change of the bridge's structural integrity, which is usually difficult to determine with human visual inspection. Global and local bridge characteristics are identified for the condition assessment of the in its vibration signature.

1.4 Scope

This thesis is organized in the following layout: an overview of the structural health monitoring is described in Section 2; the comparison of modeling approaches for full-scale nonlinear viscous dampers is discussed in Section 3; the data-driven methodologies for change detection in large-scale nonlinear dampers with noisy measurements is discussed in Section 4; an experimental study of model-order reduction effects to change detection in uncertain nonlinear systems is discussed in Section 5; and the summary and conclusion of this study are given in Section 7.

Chapter 2

Overview of Structural Health Monitoring

2.1 Components of Structural Health Monitoring Systems

In general, SHM systems consist of three subsystem components: (1) the sensing and instrumentation component, (2) the data networking and archiving component, and (3) the analysis and interpretation component. Using those subsystem components, the general procedure involving SHM is performed following the order shown in Figure 2.1. Important issues and roles of each subsystem component are also summarized in Figure 2.2. In the following section, the objectives and scopes of each component of SHM systems are described.

2.1.1 Sensing and Instrumentation

The role of the sensing and instrumentation component is to obtain physical measurements of the response of monitored structures using various types of sensors and data acquisition systems. In the design of the sensing and instrumentation component, the following important issues need to be considered:

1. Sensor types,

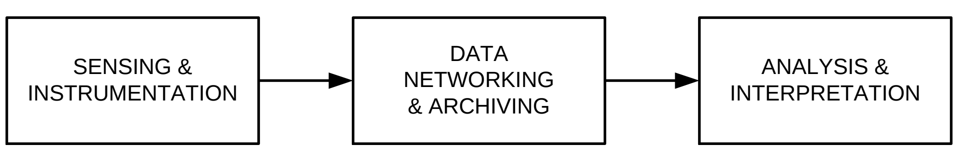

Figure 2.1: General procedure for performing structural health monitoring.

2. Sensor locations and densities,
3. Sampling frequencies and resolutions,
4. Necessary signal conditioning and preliminary data processing techniques,
5. Measurement frequencies, such as continuous, temporal, and single-time monitoring,
6. Excitation types, such as ambient and forced vibration.

2.1.2 Data Networking and Archiving

The data networking and archiving components involve tranceiving and archiving the measured data for further analyses. Typical considerations in the design of the data networking and archiving system component involve:

1. Sensor network types, such as centered or distributed networks,
2. Device network types, including General Purpose Interface Bus (GPIB or IEEE-488), Virtual Instrument Software Architecture (VISA), VME eXtensions for Instrumentation (VXI), PCI eXtensions for Instrumentation (PXI), serial, WI-FI, bluetooth, etc.,
3. Remote data communication types, such as User Datagram Protocol (UDP), modified UDP, Transmission Control Protocol and the Internet Protocol (TCP/IP), etc.,
4. Method of data archiving, and
5. Frequency of data archiving.

2.1.3 Analysis and Interpretation

The objectives of the analysis and interpretation component include the following three important tasks for the effective SHM systems: (1) the identification of monitored systems, (2) detection of changes in monitored systems, and (3) interpretation of detected damage mechanisms and establishment of maintenance strategies. In designing the analysis and interpretation components, the following important issues need to be considered:

System identification

1. Scope
    - regional / system-level / component-level
2. Modeling
    - parametric / non-parametric
    - linear / nonlinear
    - stationary / non-stationary
    - discrete / continuous
    - single-input / multiple-input
    - deterministic / stochastic

System change detection

1. Feasibility of Change Detection
    - Detection resolution

- Estimation of detection uncertainty (or detection confidence)

2. Physical Interpretation of Detected Damage

    - Effects on the structural characteristics
    - Significance in regard to structural healthiness
    - Understanding damage mechanism
    - Damage locations

<u>*Damage mechanism estimation for maintenance strategies*</u>

1. Integration of Damage Detection Results from Multiple Heterogeneous Civil Structures

2. Damage Prediction

    - Prediction of future damage based on the trends of detected damage in time
    - Estimation of prediction uncertainty

3. Reliable Maintenance Strategy

    - Reliable decision-making based on predicted damage development
    - Planing effective budget policy for infrastructure operation and maintenance

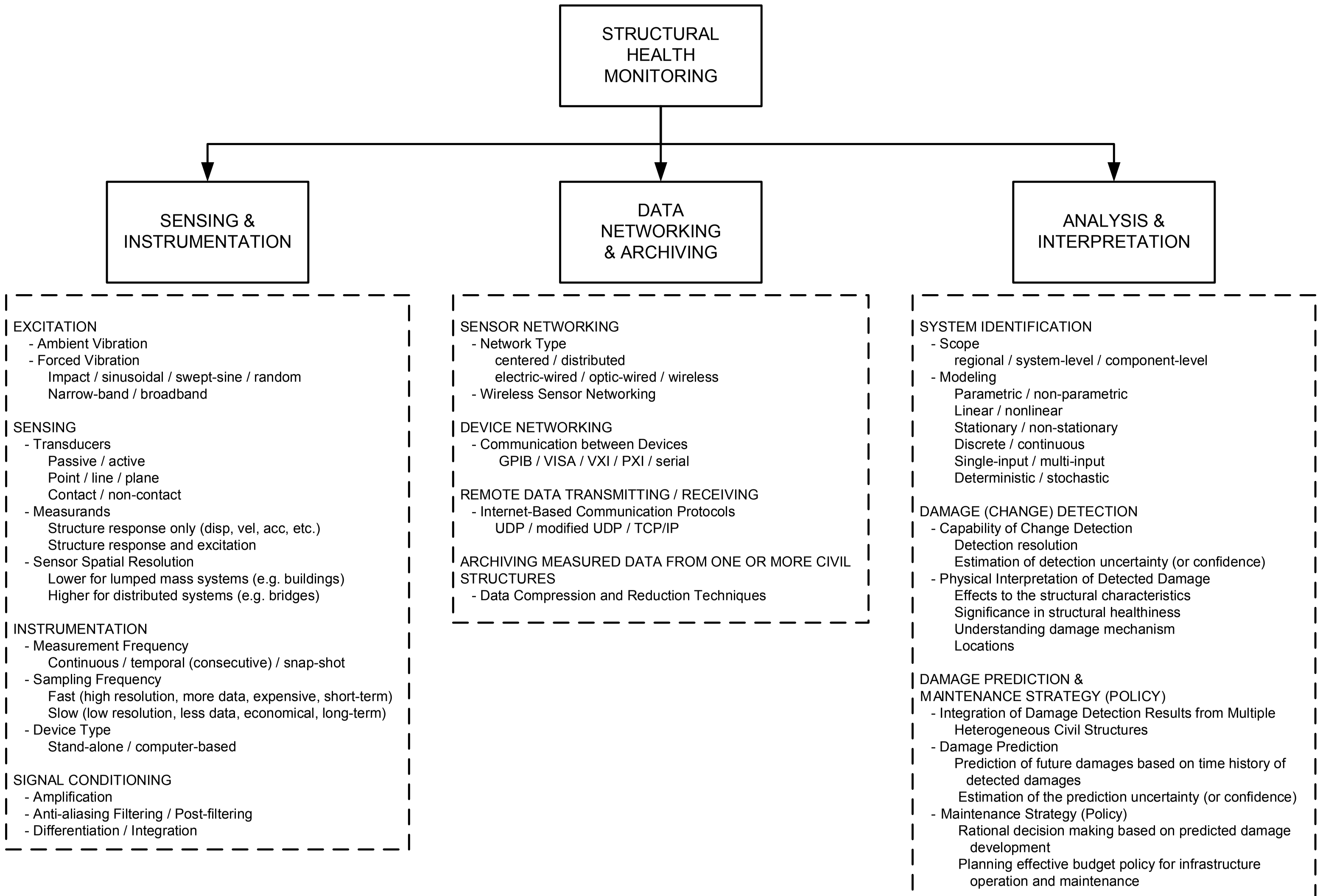

Figure 2.2: Components and scope of structural health monitoring for civil infrastructure.

2.2 Design of the Structural Health Monitoring Systems

The development of effective SHM methodologies is a design process to achieve various *design objectives* of the SHM applications with specified *design constraints* and *specifications*. Consequently, establishing clear objectives and scopes of given applications is crucial for successful SHM. This involves the following two issues:

1. Determining the objectives and scopes of operation and maintenance policies,

2. Determining the objectives and scopes of the modeling and monitoring approaches.

Among them, the former issue is the controlling goal of SHM, while the latter involve practical approaches to achieve those ultimate goals. In the design of the analysis/interpretation component, a number of modeling and monitoring approaches could be used simultaneously to achieve the various design objectives. Consequently, the optimal combinations of modeling and monitoring approaches (or "toolkits") should be determined. For each modeling and monitoring approach in the "toolkits", detailed identification and change detection strategies should be also considered.

Once the analysis/interpretation component is designed, the sensing/instrumentation and data networking/archiving components need to be designed as the next step. The implementation of those two components should be performed to meet the pre-determined objectives of the analysis/interpretation component.

The above discussion indicates that, unlike the procedure for performing SHM in Figure 2.1, the procedure of designing SHM systems should consider the analysis/interpretation component first, then to consider the sensing/instrumentation and data networking/archiving components to meet the goals of SHM applications as illustrated in Figure 2.3. In addition, because the performance of the analysis/interpretation component is more directly related to achieving the ultimate objectives of the SHM system, the analysis/interpretation component needs to be considered more carefully than the sensing/instrumentation and data networking/archiving components.

Many current SHM methodologies, however, tend to put too much emphasis on the sensing/instrumentation and data networking/archiving components. With the advent of modern sensing and data acquisition technologies, the development of the required sensing and data networking systems becomes more feasible in many SHM applications. However, the development of effective analysis and interpretation components for complex nonlinear structures is still very challenging, and it consequently becomes one of the major obstacles to designing reliable SHM. Hence, in this study, the development of the analysis/interpretation methodologies will be more focused. However, the development of an effective sensing/instrumentation and data networking/archiving system for a full-scale suspension bridge is also conducted as a part of the study, and the description of the developed bridge monitoring systems is presented in Section 6.2.3.

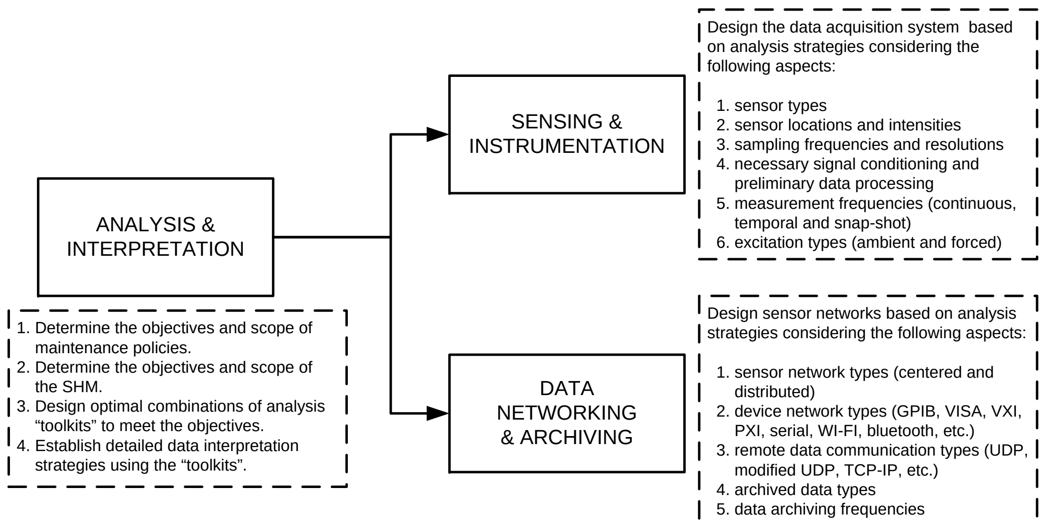

Figure 2.3: Preferred design approach for structural health monitoring procedures.

Chapter 3

Comparison of Modeling Approaches for Full-Scale Nonlinear Viscous Dampers

3.1 Introduction

3.1.1 Motivation

The orifice fluid viscous damper (hereinafter viscous damper) is a passive energy dissipation device that is commonly employed in civil structures to reduce structural vibrations, typically induced by seismic motion or wind. A typical viscous damper consists of a piston rod, seal retainer, acetal resin seal, cylinder, chambers filled with compressible silicon fluid, control valves, rod make-up accumulator, and accumulator housing (Figure 3.1). For effective energy dissipation, the viscous damper employs small orifices on its piston head so that the fluid (usually compressible silicon oil) is forced to pass the orifices, when the piston reciprocates. The relationship between velocity and damping force follows a clear constitutive law at relatively low frequencies (Constantinou et al., 1993).

In general, the viscous damper is utilized in a civil structure to control seismic, wind-induced and thermal expansion motions, and it is usually arranged in one of the following configurations: (1) a diagonal or chevron bracing element of steel or concrete trusses, (2) a part of the wind/rain cable stays of suspension bridges, (3) a part of a tuned mass damper to reduce the structure

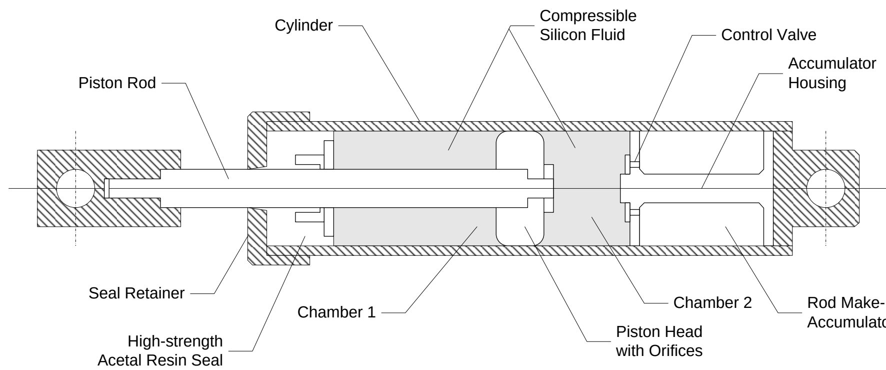

Figure 3.1: Components of a orificed viscous damper (Soong and Dargush, 1997).

vibration, (4) a part of a base isolation system to add energy dissipation, and (5) as a device for allowing free thermal movement. The viscous damper can be used in the construction of a new building, or the retrofit of an existing structure. In the case of structural retrofit, utilizing a viscous damper is frequently the only measure that will not prolong lane closure and traffic interruption (Caltrans, 2003). Thanks to its effective energy dissipation capability and wide range of application, the importance of viscous dampers in vibration control has increased. Various applications of the viscous damper and other passive control devices have been reported worldwide (Aiken, 1996; Chen and Duan, 2000; Housner et al., 1997; Kareem et al., 1999; Kitagawa and Midorikawa, 1998; Ou and Li, 2004; Park and Koh, 2001; Spencer Jr. and Nagarajaiah, 2003; Wolfe et al., 2002).

In the U.S.A., after the Loma Prieta earthquake in 1989, the California Department of Transportation (Caltrans) initiated seismic vulnerability assessment and subsequently retrofitting of all major California toll bridges (Caltrans, 2003). In order to improve the dynamic characteristics of a specific bridge, viscous dampers were employed in some retrofit projects (Sheng and

Lee, 2003). An example is the massive retrofit effort recently completed on the San Francisco-Oakland Bay Bridge, West Spans Suspension Bridge. More than 100 full-scale viscous dampers (max. force: 3115 kN, max. stroke: $\pm$584 mm) were installed at the truss-to-tower connections of the suspended spans as anti-seismic dissipators. Another example of Caltrans' retrofit projects is the Vincent Thomas Bridge, which employed full-scale viscous dampers for limiting the deformation of the suspended trusses (Baker, 1998).

In Europe, full-scale viscous dampers are also widely used for structural vibration control. A recent example of the viscous damper in new bridge construction is the Rion-Antirion Bridge project in Greece. This 2252-m multi-span suspension bridge is constructed on a local active seismic fault, which causes high intensity earthquakes and large tectonic movements. A number of full-scale viscous dampers with a maximum force of 3500 kN and maximum stroke of $\pm$2600 mm were installed between the deck and pier with fuse retainers to reduce the deformation induced by the seismic ground motion (Infanti et al., 2003).

U.S. design provisions for viscous dampers and seismic isolators have been developed by the National Earthquake Hazards Reduction Program (NEHRP). The NEHRP is a joint program of the Federal Emergency Management Agency (FEMA), National Institute of Standards and Technology (NIST), National Science Foundation (NSF), and the United States Geological Survey (USGS). In the recent update of the *NEHRP Recommended Provisions for New Buildings and Other Structures* (BSSC, 2004), a new chapter of "Structures with Damping Systems" (FEMA 450 Ch.15) was added. This chapter specifies provisions of designing the damping system and testing damping devices. The *MCEER/ATC-49 Recommended LRFD Guidelines for the Seismic Design of Highway Bridges* also provides the guidelines and design procedures for seismic isolation (Ch.15) (ATC/MCEER, 2003).

Although the effect of the viscous damper in the design of vibration control is relatively well-known, few studies of structural health monitoring (SHM) techniques for operational and maintenance purposes have been reported on full-scale viscous dampers. The performance of viscous dampers installed on important civil structures must be carefully assessed to judge if the damper is operating as designed. The development of condition assessment techniques includes testing guidelines and identification methods. Due to their massive size and inherent nonlinearity, special considerations should be given in testing and identification of full-scale viscous dampers.

3.1.2 Viscous Damper Tests

Currently, testing of viscous dampers is usually conducted as pre-qualification and quality control tests for structural vibration control purposes. Along these lines, NIST developed three classes of testing guidelines, including a pre-qualification test, prototype test, and quality control test (Shenton, 1994). These test guidelines provide the provisions of project-specific and project-unspecific testing for both prototype and commercialized seismic control devices. Another purpose of testing viscous dampers is to provide basic information concerning the characteristics of the damping devices for the design procedures of vibration control.

The Earthquake Engineering Research Center (EERC) at the University of California, Berkeley has developed testing methods for full-scale viscous dampers and seismic isolation devices (Aiken, 1998; Aiken and Kelly, 1996; Aiken et al., 1993). Aiken classified full-scale testing procedures into quasi-static testing and dynamic testing (Aiken et al., 1993). The quasi-static testing is used when the loading rate and thermodynamic effects are not significant. A typical loading rate in quasi-static testing is 200-300 mm/min (8-12 in/min). The dynamic testing includes dropping a known weight on the end of a vertically mounted viscous damper (drop test), and servo-hydraulic testing (dynamic cyclic test). In the drop test, the relationship of the exciting force and damper response can be obtained. Because no significant energy is input into the damper due to the short impact time, transient temperature effects are not recovered. The dynamic cyclic test provides more opportunities to understand the nonlinearity and thermal properties of the viscous damper. However, because the dynamic cyclic test requires a powerful servo-hydraulic testing facility, the dynamic cyclic test can only be performed at very limited locations (Beck et al., 1994). As a result, there are few available experimental data sets of full-scale viscous dampers.

A monotonic sinusoid excitation is typically used in the dynamic cyclic test. The Highway Innovative Technology Evaluation Center (HITEC) developed nine standardized testing methods for seismic isolators and energy dissipation devices (HITEC, 1996, 1998a,b, 1999). In their study, “off-the-shelf” full-scale viscous dampers were tested with sets of monotonic sinusoidal excitation, and the damper response was recorded. For the identification of a nonlinear system, using a monotonic sinusoid excitation may not reveal the nonlinearity of the system completely, and for this reason, a broadband random excitation is commonly used. For meaningful identification results, the testing time with a broadband random excitation should be longer than that with a monotonic sinusoidal excitation. In the case of full-scale viscous dampers, however, a long testing time frequently generates an enormous amount of heat that is converted from the dissipated energy. Consequently, the temperature of the silicon fluid inside the damper's piston chamber should be controlled to preclude added complexities.

3.1.3 Identification of Viscous Dampers

For the identification of viscous dampers, many analytical models have been developed based on Maxwell models (Constantinou and Symans, 1993; Constantinou et al., 1993; Makris and Constantinou, 1991; Makris et al., 1993). Current identification techniques for viscous dampers are mostly based on these parametric models. Although parametric identification techniques have been successfully used to identify viscous dampers, non-parametric identification techniques are more suitable in SHM (Soong, 1998). This is because, in the SHM context, the system characteristics may continuously vary over time, both quantitatively as well as qualitatively. Therefore, the development of a condition assessment methodology for full-scale viscous dampers using non-parametric identification methods will be a critical step towards establishing the operation and maintenance strategies for vibration-controlled structures.

3.1.4 Objectives and Scope

A joint study between the University of Southern California and the University of California, Berkeley was conducted on a full-scale viscous damper. The research objectives were (1) to obtain quantitative data on full-scale tests, (2) to obtain information on accuracy and utility of various modeling approaches, (3) to compare advantages and limitations of both parametric and non-parametric models, (4) to study nonlinear features of viscous dampers, and (5) to study model dependency on excitation ranges. The 1112 kN (250 kip) full-scale viscous damper was tested using multiple sets of monotonic sinusoidal excitation at the University of California, Berkeley, and the test data were analyzed at the University of Southern California. The research material is organized in the following layout: The experimental studies are discussed in Section 2; an overview of the modeling approaches is presented in Section 3; the parametric and non-parametric identification approaches are presented in Section 4; and the results are discussed in Section 5.

3.2 Experimental Studies

3.2.1 Test Apparatus

The 1112 kN (250 kip) viscous damper was tested in the Earthquake Engineering Research Center (EERC) at the University of California, Berkeley (Figure 3.2). The damper is a sister damper of the eight dampers installed at the 91/5 over-crossing in Orange County, CA. The damper has a mid-stroke length of 1828.8 mm (72 in) and a maximum stroke of $\pm$203.2 mm (8.0 in). The test setup consists of a self-equilibrating reaction frame with a 1335 kN (300 kip) actuator equipped with a 3785 l/min (1000 gpm) proportional valve. The bolted head-piece at the opposite side of the actuator can assume other positions to accommodate dampers with different length. In addition to the load-cell and LVDT, the damper was instrumented with six thermocouple probes along its length (Figure 3.2 (b)).

3.2.2 Test Cases

A total of 15 experiments were performed to obtain the dynamic response of the viscous damper. The experiments were designed to determine the dynamic performance characteristics of the damper at varying velocities and displacements. The damper was subjected to multiple sets of

(a) (b)

Figure 3.2: The 1112 kN (250 kip) viscous damper installed on a damper testing machine at the University of California, Berkeley.

monotonic sinusoidal excitation at peak velocities of ±254.0 mm/s (10.0 in/s), ±317.5 mm/s (12.5 in/s), ±381.0 mm/s (15.0 in/s), and ±444.5 mm/s (17.5 in/s) and peak displacements of ±101.6 mm (4.0 in), ±127.0 mm (5.0 in), ±152.4 mm (6.0 in), and ±177.8 mm (7.0 in). All test cases had a 6-cycle excitation period, except for one having a 10-cycle period. The test specifications are summarized in Table 3.1.

3.2.3 Instrumentation

The damper displacement and force were measured: the force was measured with an in-line load cell, and the displacement between the reaction frame and the clevis was measured with an LVDT. The transducer measurements were sampled at 100 Hz.

3.2.4 Preliminary Data Processing

Once the force and displacement of the damper were measured, the measured displacement was numerically differentiated to obtain the corresponding velocity and acceleration. The records

Table 3.1: Test specifications of the 1112 kN (250 kip) viscous damper. A total of 15 experiments were performed for different levels of peak velocity and peak displacement.

No	Name of data set	Peak velocity	Peak displacement	Freqeuncy	No. cycles
1	UCB1_10_4	±254.0 mm/s (10.0 in/s)	±101.6 mm (4.0 in)	0.398 Hz	6
2	UCB1_10_5	±254.0 mm/s (10.0 in/s)	±127.0 mm (5.0 in)	0.318 Hz	6
3	UCB1_10_6	±254.0 mm/s (10.0 in/s)	±152.4 mm (6.0 in)	0.265 Hz	6
4	UCB1_12_4	±317.5 mm/s (12.5 in/s)	±101.6 mm (4.0 in)	0.500 Hz	6
5	UCB1_12_5	±317.5 mm/s (12.5 in/s)	±127.0 mm (5.0 in)	0.400 Hz	6
6	UCB1_12_6	±317.5 mm/s (12.5 in/s)	±152.4 mm (6.0 in)	0.332 Hz	6
7	UCB1_12_7	±317.5 mm/s (12.5 in/s)	±177.8 mm (7.0 in)	0.284 Hz	6
8	UCB1_15_4	±381.0 mm/s (15.0 in/s)	±101.6 mm (4.0 in)	0.600 Hz	6
9	UCB1_15_5	±381.0 mm/s (15.0 in/s)	±127.0 mm (5.0 in)	0.477 Hz	6
10	UCB1_15_6	±381.0 mm/s (15.0 in/s)	±152.4 mm (6.0 in)	0.400 Hz	10
11	UCB1_15_7	±381.0 mm/s (15.0 in/s)	±177.8 mm (7.0 in)	0.341 Hz	6
12	UCB1_17_4	±444.5 mm/s (17.5 in/s)	±101.6 mm (4.0 in)	0.695 Hz	6
13	UCB1_17_5	±444.5 mm/s (17.5 in/s)	±127.0 mm (5.0 in)	0.557 Hz	6
14	UCB1_17_6	±444.5 mm/s (17.5 in/s)	±152.4 mm (6.0 in)	0.464 Hz	6
15	UCB1_17_7	±444.5 mm/s (17.5 in/s)	±177.8 mm (7.0 in)	0.399 Hz	6

were bandpass-filtered within the frequency range 0.1 - 10 Hz. A sample damper response after data processing is shown in Figure 3.3.

3.3 Overview of Modeling Approaches

3.3.1 Simplified Design Model

Some analytical models of the orifice viscous damper, hereafter referred to as the Simplified Design Model (SDM), have been developed based on Maxwell models by Makris and Constantinou (1991) and Makris et al. (1993). The dynamic performance characteristics of the damper significantly depend on the configuration of the small orifices on the piston head, following a

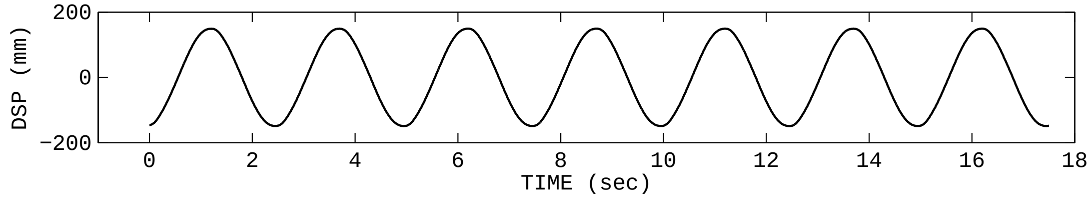

(a) Displacement

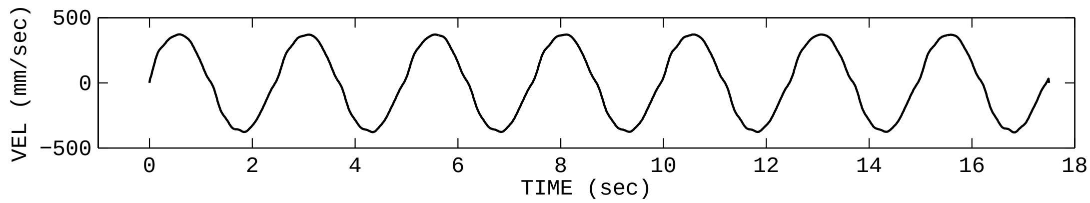

(b) Velocity

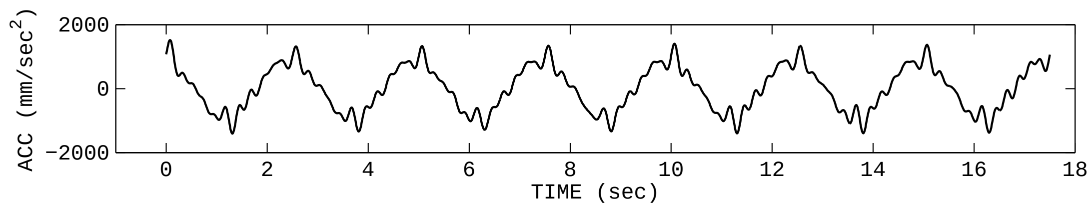

(c) Acceleration

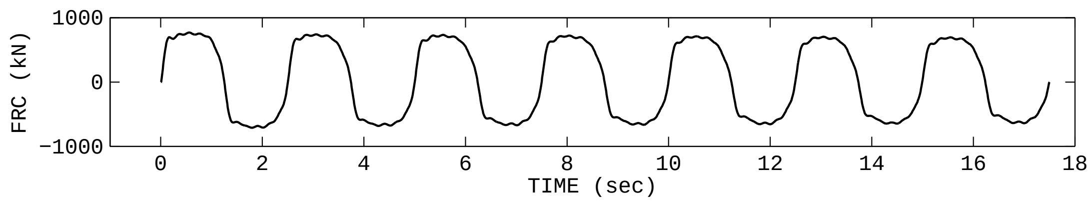

(d) Force

Figure 3.3: Sample time histories of measured damper response after preliminary data processing (UCB1_15_6). The figure illustrates the time histories of the (a) displacement, (b) velocity, (c) acceleration, and (d) force.

nonlinear constitutive law at relatively low frequency (Constantinou and Symans, 1993; Constantinou et al., 1993) as expressed by

$$\hat{f}_d(t) = m\ddot{x} + Csgn(\dot{x})|\dot{x}|^n \tag{3.1}$$

where $\hat{f}_d(t)$ is the designed damping force, $\dot{x}$ is the damper stroke velocity, $\ddot{x}$ is the damper stroke acceleration, m is the "effective" moving mass of the damper, C is the damping coefficient, and n is the exponent ($n = 1$ for linear; $n < 1$ for softening; and $n > 1$ for hardening). The tested viscous damper under discussion was designed for $C = 86.03$ kN·sec^n/mm^n (60 kip·sec^n/in^n) and $n = 0.35$.

For the optimal values of the parameters (i.e., m, C, and n), the Adaptive Random Search (ARS) method (Andronikou et al., 1982; Masri et al., 1980) is employed. Using the ARS method, the optimal values of the parameters are searched within the solution space of a differential equation for minimal normalized mean square error between the measured and identified damper responses. In order to determine the optimal values of m, C, and n, the simplified design model (Equation 3.1) is reformulated as a first order differential equation

$$\underbrace{\begin{pmatrix} \dot{x} \\ \ddot{x} \end{pmatrix}}_{\dot{y}} = \underbrace{\begin{pmatrix} \dot{x} \\ \frac{1}{m}(f(t) - Csgn(\dot{x})|\dot{x}|^n) \end{pmatrix}}_{F(t,y)} \tag{3.2}$$

The solution of Equation 3.2 can be determined, using standard numerical time-marching techniques, if the initial conditions (i.e., $x(0)$ and $\dot{x}(0)$) and the values of the system parameters are specified. The optimal values of the unknown parameters can be found by minimizing the following cost function

$$J(\epsilon) = w_1 \times \frac{100}{N\sigma_x^2}\sum_{i=1}^{N}(x_i - \hat{x}_i)^2 + w_2 \times \frac{100}{N\sigma_{\dot{x}}^2}\sum_{i=1}^{N}(\dot{x}_i - \hat{\dot{x}}_i)^2 \tag{3.3}$$

where x and $\dot{x}$ are the measured displacement and velocity, $\hat{x}$ and $\hat{\dot{x}}$ are the computed displacement and velocity from Equation 3.2, N is the number of data points, σ_x^2 and $\sigma_{\dot{x}}^2$ are variances of the measured responses, and w_1 and w_2 are normalizing weights.

3.3.2 Restoring Force Method

A constant-mass, single-degree-of-freedom nonlinear dynamic system can be represented by the following equation of motion

$$m\ddot{x}(t) + r(x(t), \dot{x}(t)) = f(t) \tag{3.4}$$

where $f(t)$ is the exciting force, m is the mass, and r is the restoring force, which is a nonlinear function of the displacement (x) and velocity ($\dot{x}$). Using the restoring force method (RFM), the restoring force surface can be approximated by a series of two-dimensional Chebyshev polynomials (Masri and Caughey, 1979)

$$r(x, \dot{x}) \approx \hat{r}(x, \dot{x}) = \sum_{i=0}^{MX} \sum_{j=0}^{NY} \bar{C}_{ij} T_i(\bar{x}) T_j(\bar{\dot{x}}) \tag{3.5}$$

where $\bar{x}$ and $\bar{\dot{x}}$ are the normalized displacement and velocity in the range [-1, 1], $\bar{C}_{ij}$ is the normalized Chebyshev coefficient, and T_n is the n^{th} order Chebyshev polynomial. For the tested viscous damper, if the excitation frequency is low (i.e., nearly quasi-static conditions), the inertia term in Equation 3.4 becomes negligible. Then, the damper can be modeled as

$$\hat{f}_r(t) \approx \sum_{i=0}^{MX} \sum_{j=0}^{NY} \bar{C}_{ij} T_i(\bar{x}) T_j(\bar{\dot{x}}) \tag{3.6}$$

where $\hat{f}_r(t)$ is the damping force identified with the RFM. One of the advantages of using the RFM is that the orthogonality is preserved, using the Chebyshev polynomials. That is, with the normalized domain of [-1, 1], the identified Chebyshev coefficient of each term is not affected by the other terms. This feature of the RFM can be very attractive, especially in SHM applications, where the proper order of the expansion is often unknown. In identification, the Chebyshev polynomial is more appropriate to the polynomial type nonlinearity than the piece-wise orthogonal functions. It is also known that the orthogonal polynomials with limited bounds, such as the Chebyshev polynomial, is more accurate than those with unlimited bounds, such as Hermite polynomials. According to de Moivre's Theorem, a Chebyshev series has the following relationship with a power series (Mason and Handscomb, 2003)

$$T_0(x) = 1, \quad T_1(x) = x, \quad T_2(x) = 2x^2 - 1, \ldots, \quad T_{n+1}(x) = 2xT_n(x) - T_{n-1}(x), \ldots \tag{3.7}$$

Using the relationship in Equation 3.7, the viscous damper restoring force can be modeled

$$\hat{f}_p(t) = \sum_{i=0}^{MX} \sum_{j=0}^{NY} a_{ij} x^i \dot{x}^j \tag{3.8}$$

where a_{ij} is a de-normalized power series coefficient, and $\hat{f}_p(t)$ is the damping force identified with power series.

3.3.3 Artificial Neural Networks

The artificial neural networks (ANN) identification technique has been applied successfully to broad classes of nonlinear systems. For the tested viscous damper, a three-layer feedforward neural network (the last layer is the output layer) was constructed and trained with the ARS. Descriptions of the ANN and ARS are given in Masri et al. (1993, 2000, 1999). Using the following three-layer ANN, the viscous damper force can be expressed:

$$\hat{f}_a(t) = \Gamma \left\{ \sum_{j=1}^{N2} \left[w_j \Gamma \left(\sum_{k=1}^{N1} v_{j,k} y_k + b_{v,j} \right) + b_w \right] \right\} \tag{3.9}$$

where w and v are weights, b is bias, $N1$ is the number of nodes in the first layer, $N2$ is the number of nodes in the second layer, Γ is a tangent-sigmoid function, and $\hat{f}_a(t)$ is the damping force identified with the ANN method. Here, the third layer is used as an output layer.

3.4 Identification of the Viscous Damper

3.4.1 Parametric Identification of Simplified Design Model

Identification

For the optimal values of the unknown parameters in Equation 3.1, the parametric identification using a time-marching technique (SDM) was applied. In the ARS, the design values of $C = 86.03$ kN·sec^n/mm^n (60 kip·sec^n/in^n) and $n = 0.35$ were used as the initial values of the unknown parameters. The solution space of the optimization was constrained for positive values of the parameters. The initial values and the bounds of the solution space are summarized in Table 3.2. For each optimization process, 300 global searches and 25 local searches were performed. Three identical optimization processes were conducted with randomly generated initial parameters, and the identified parameters with the least normalized mean-square-error were selected.

Table 3.2: Initial values and boundaries of the unknown parameters in Equation 3.1 for the Adaptive Random Search method. Parameter m is the "effective" moving mass, C is the damping coefficient, and n is the exponent.

Parameter	Initial value	Lower bound	Upper bound
m	14,593.9 kg (1.0 slug)	0.1459 kg (1×10^{-5} slug)	1,459,390 kg (100.0 slug)
C	86.03 kN·sec^n/mm^n (60 kip·sec^n/in^n)	0.14 kN·sec^n/mm^n (1×10^{-1} kip·sec^n/in^n)	143.38 kN·sec^n/mm^n (100 kip·sec^n/in^n)
n	0.35	1×10^{-1}	2.0

A sample identification result of the SDM is illustrated in Figures 3.4 (a) and (d). In the figure, the identified damper response was obtained, using Equation 3.1 for the identified optimal values of the parameters. The m, C, and n were determined for all test cases, and the identified values are summarized in Table 3.3. The mean of the identified m is 735.64 kg with the coefficient of variance of 0.3185. The mean of the identified C is 4.357 kN·sec^n/mm^n, and its coefficient of the variance is 0.0512. The mean of the identified n is 0.391, and its coefficient of variance is 0.0345.

The normalized mean-square-error (NMSE) of the SDM-identification was calculated to evaluate the accuracy of the identification results. The NMSE was calculated as

$$\mathrm{NMSE}(\hat{f}) = \frac{100}{N\sigma_f^2} \sum_{i=1}^{N} (f_i - \hat{f}_i)^2 \tag{3.10}$$

where f is the measured force, $\hat{f}$ is the identified force, N is the number of data points, and σ_f^2 is the variance of the measured force (Worden and Tomlinson, 2001). The identification errors

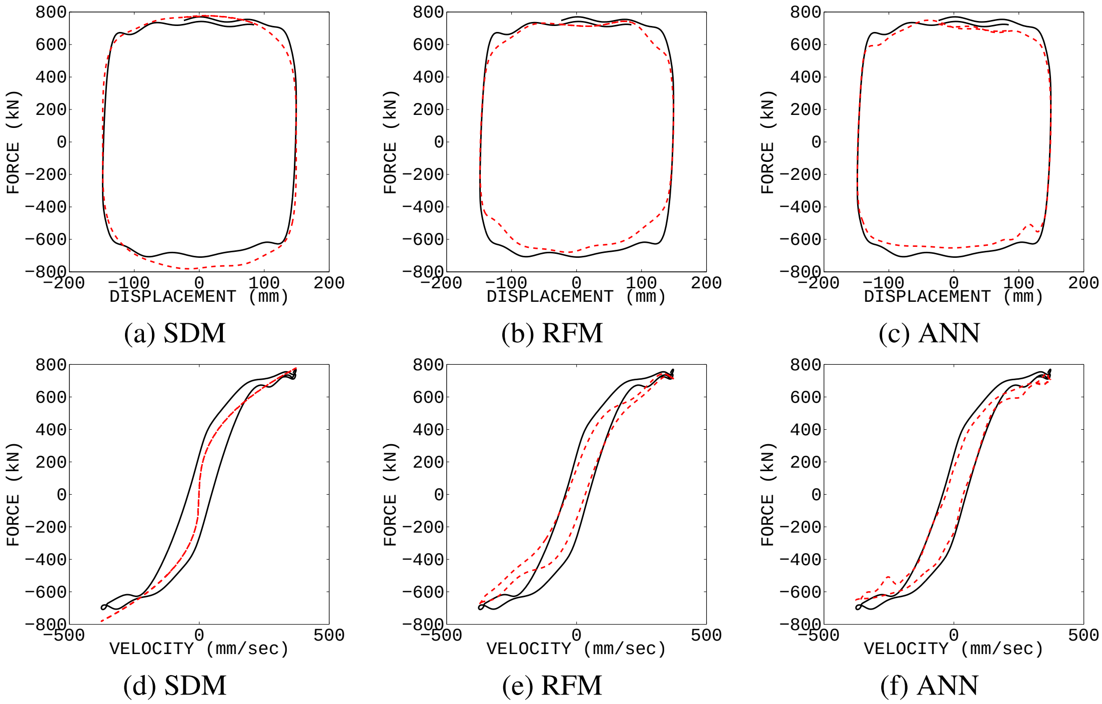

(a) SDM (b) RFM (c) ANN

(d) SDM (e) RFM (f) ANN

Figure 3.4: Sample identification results of the parametric simple design model (SDM), the non-parametric restoring force method (RFM), and the non-parametric artificial neural networks (ANN) for the data set UCB1_15_6. The phase plots show approximately a one-cycle period of the damper response (solid line for measured, and dashed for identified forces). In the figure, the first row shows the relationship between displacement and force, and the second row shows the relationship between velocity and force for each investigated identification method.

for all test cases are summarized in the gray cells in Table 3.4 (a). The mean of the identification error is 3.75% with the coefficient of covariance of 0.28.

Validation

Once the viscous damper was identified using the SDM, the results were validated with the data sets, which had not been used in the identification phase. A total of 196(=14$\times$14) validation processes were performed, and the NMSE's are summarized in Table 3.4 (a). In the table, the identification errors are shown in the grayed cells, and the validation errors are summarized in the white cells. The values in the same column show the errors with respect to the same identified

Table 3.3: Mass, damping constant (C), and exponent (n) identified using the simplified design model (SDM). The system parameters were determined, using the adaptive random search optimization, and for the determined parameters, the governing differential equation of motion was directly solved through the use of conventional time-marching techniques.

No	Name of data set	Mass (kg)	C (kN·sec^n/mm^n)	n
1	UCB1_10_4	567.7	78.5085	0.3773
2	UCB1_10_5	1199.6	70.1302	0.4055
3	UCB1_10_6	1208.4	70.1866	0.4108
4	UCB1_12_4	685.9	74.6388	0.3896
5	UCB1_12_5	777.9	70.7238	0.4030
6	UCB1_12_6	869.8	70.5987	0.4036
7	UCB1_12_7	974.9	71.4950	0.3997
8	UCB1_15_4	567.7	78.5085	0.3773
9	UCB1_15_5	594.0	75.4005	0.3862
10	UCB1_15_6	785.2	69.6316	0.4076
11	UCB1_15_7	645.1	72.1798	0.3967
12	UCB1_17_4	494.7	79.7295	0.3732
13	UCB1_17_5	522.5	79.4230	0.3747
14	UCB1_17_6	519.5	77.2283	0.3789
15	UCB1_17_7	621.7	76.9658	0.3799
	avg	735.64	74.366	0.3909
	cov	0.3185	0.0512	0.0345

parameters (i.e., C and n), and the values in the same row show the errors with respect to the same data set. The mean of the averaged validation errors for the same identified parameters is 3.79% with the coefficient of variance of 0.098. The mean of the averaged validation errors for the same data set is 3.79% with the coefficient of variance of 0.31.

3.4.2 Nonparametric Identification Using Restoring Force Method

Identification

An optimal Chebyshev order of the RFM-identification was determined using the tested damper response. The damper was identified with the order of $n = 1, 2, 3, \ldots, 15$, and the determined NMSE's are plotted in Figure 3.5 in semi-log scale. The NMSE decreases for $1 < n \leq 9$, and increases for $9 < n \leq 15$ due to over-fitting. Because Figure 3.5 is plotted in semi-log scale,

Table 3.4: Identification and validation results of the simplified design model (SDM), the restoring force method (RFM), and the artificial neural networks (ANN). The values are the normalized mean-squared errors (NMSE) of the estimated force versus the measured force. For each identification method, the identification errors are shown in grayed cells, and the validation errors are shown in white cells. The values in the same row show the errors with respect to the same data set, while the values in the same column show the errors with respect to the same identified coefficients (i.e., the damping constant (C) and exponent (n) for the SDM, the normalized Chebyshev coefficients for the RFM, and the trained weights and biases for the ANN).

(a) Simplified Design Model (Parametric)

Data No.	Data No. (w.r.t. Same Identified C and n)																
	1	2	3	4	5	6	7	8	9	10	11	12	13	14	15	avg	cov
1	**4.60**	4.99	5.65	4.71	4.91	4.93	4.81	4.60	4.62	5.05	4.72	4.56	4.59	4.49	4.51	4.78	0.063
2	3.15	**3.55**	4.17	3.27	3.47	3.49	3.37	3.15	3.18	3.61	3.29	3.11	3.15	3.07	3.08	3.34	0.087
3	2.62	2.77	**3.13**	2.64	2.72	2.73	2.68	2.62	2.61	2.80	2.64	2.62	2.62	2.60	2.60	2.69	0.051
4	5.32	5.79	6.50	**5.45**	5.69	5.72	5.58	5.32	5.35	5.86	5.48	5.27	5.31	5.22	5.23	5.54	0.061
5	3.60	4.01	4.64	3.71	**3.92**	3.95	3.83	3.60	3.63	4.07	3.74	3.57	3.59	3.53	3.54	3.80	0.078
6	2.94	3.31	3.90	3.03	3.23	**3.26**	3.15	2.94	2.96	3.37	3.06	2.91	2.93	2.87	2.88	3.12	0.088
7	1.94	2.42	3.06	2.08	2.33	2.35	**2.22**	1.94	1.99	2.49	2.13	1.90	1.93	1.88	1.89	2.17	0.149
8	5.35	6.01	6.85	5.55	5.88	5.92	5.75	**5.35**	5.42	6.10	5.61	5.29	5.33	5.24	5.26	5.66	0.078
9	3.86	4.42	5.16	4.02	4.31	4.34	4.19	3.86	**3.91**	4.50	4.07	3.81	3.84	3.77	3.79	4.12	0.092
10	3.03	3.79	4.66	3.26	3.66	3.69	3.50	3.03	3.13	**3.89**	3.35	2.95	3.00	2.92	2.94	3.39	0.144
11	2.23	2.74	3.39	2.37	2.64	2.67	2.53	2.23	2.29	2.81	**2.43**	2.20	2.22	2.18	2.19	2.48	0.135
12	5.38	6.22	7.17	5.63	6.05	6.10	5.89	5.38	5.47	6.31	5.72	**5.29**	5.35	5.25	5.28	5.77	0.093
13	3.78	4.52	5.38	4.00	4.38	4.42	4.23	3.78	3.87	4.62	4.08	3.71	**3.76**	3.68	3.71	4.13	0.115
14	2.82	3.55	4.37	3.04	3.41	3.45	3.27	2.82	2.91	3.64	3.13	2.76	2.80	**2.74**	2.76	3.17	0.145
15	2.38	3.18	4.06	2.63	3.04	3.08	2.88	2.38	2.49	3.29	2.73	2.31	2.36	2.29	**2.76**	2.76	0.181
avg	3.53	4.09	4.81	3.69	3.98	4.01	3.86	3.53	3.59	4.16	3.75	3.48	3.52	3.45	3.47		
cov	0.33	0.30	0.27	0.32	0.30	0.30	0.31	0.33	0.33	0.29	0.31	0.33	0.33	0.33	0.33		

(b) Restoring Force Method Identification (Non-parametric)

Data No.	Data No. (w.r.t. Same Identified C and n)																
	1	2	3	4	5	6	7	8	9	10	11	12	13	14	15	avg	cov
1	**1.50**	2.11	2.39	2.38	1.47	1.67	2.76	3.18	2.37	2.72	4.49	3.69	3.94	4.11	4.08	2.86	0.35
2	1.86	**1.61**	1.57	2.24	1.24	1.09	1.92	3.19	2.13	2.23	3.51	3.98	4.01	3.77	3.60	2.53	0.41
3	2.37	2.00	**1.56**	2.21	1.04	0.78	1.58	2.71	1.60	1.43	2.52	3.28	3.08	2.69	2.47	2.09	0.35
4	2.55	3.00	2.58	**1.68**	1.06	1.35	2.39	1.30	0.94	1.25	2.54	1.40	1.50	1.78	2.11	1.83	0.36
5	2.91	3.41	2.77	2.37	**1.07**	1.25	2.16	1.80	1.07	0.89	2.13	1.57	1.32	1.30	1.30	1.83	0.42
6	3.19	3.11	2.32	2.40	1.03	**0.91**	1.70	2.01	1.06	0.72	1.72	1.96	1.55	1.26	1.13	1.74	0.44
7	3.08	3.13	2.34	2.87	1.12	0.92	**1.65**	2.59	1.35	0.75	1.83	2.44	1.91	1.46	1.07	1.90	0.42
8	3.66	4.51	3.82	2.45	1.60	2.01	3.09	**1.24**	1.00	1.19	2.46	0.72	0.69	1.07	1.43	2.06	0.59
9	3.94	4.44	3.52	2.66	1.52	1.76	2.63	1.52	**1.02**	0.87	1.90	1.05	0.77	0.81	0.98	1.96	0.61
10	3.83	4.26	3.28	3.02	1.47	1.52	2.25	2.06	1.23	**0.74**	1.68	1.59	1.10	0.88	0.75	1.98	0.62
11	4.69	4.83	3.61	3.48	1.86	1.78	2.48	2.37	1.45	0.81	**1.63**	1.85	1.22	0.87	0.68	2.24	0.60
12	4.47	5.54	4.75	3.21	2.17	2.66	3.76	1.61	1.40	1.51	2.86	**0.74**	0.63	1.08	1.40	2.52	0.61
13	4.91	5.80	4.78	3.68	2.25	2.61	3.55	2.00	1.54	1.29	2.48	1.04	**0.66**	0.83	0.96	2.56	0.64
14	5.24	5.76	4.58	3.85	2.28	2.44	3.28	2.26	1.59	1.11	2.12	1.38	0.83	**0.73**	0.73	2.54	0.65
15	5.31	5.82	4.59	4.26	2.39	2.43	3.20	2.77	1.86	1.16	2.16	1.84	1.15	0.89	**0.68**	2.70	0.60
avg	3.57	3.95	3.23	2.85	1.57	1.68	2.56	2.17	1.44	1.25	2.40	1.90	1.62	1.57	1.56		
cov	0.34	0.37	0.35	0.25	0.32	0.38	0.27	0.29	0.30	0.46	0.32	0.54	0.70	0.69	0.68		

(c) Artificial Neural Networks Identification (Non-parametric)

Data No.	Data No. (w.r.t. Same Identified C and n)																
	1	2	3	4	5	6	7	8	9	10	11	12	13	14	15	avg	cov
1	**0.31**	0.48	0.54	2.49	0.47	0.57	0.67	2.82	1.13	0.86	0.79	1.37	2.39	1.23	1.57	1.18	0.69
2	0.97	**0.28**	0.29	5.57	0.73	0.73	0.57	5.65	1.96	1.34	1.01	2.79	4.01	1.78	2.40	2.01	0.89
3	0.89	0.39	**0.27**	6.54	0.85	0.97	0.43	7.19	2.00	1.29	1.03	3.32	4.25	1.73	2.42	2.24	0.98
4	0.47	0.70	0.71	**0.39**	0.39	0.51	1.10	0.52	0.55	1.02	0.84	0.97	1.20	1.13	1.67	0.81	0.46
5	0.54	0.55	0.40	1.47	**0.26**	0.41	0.50	1.94	0.52	0.46	0.44	0.96	1.25	0.53	0.66	0.73	0.64
6	0.84	0.48	0.36	2.46	0.40	**0.24**	0.37	3.29	0.77	0.40	0.38	1.43	1.92	0.64	0.81	0.99	0.91
7	0.98	0.37	0.41	6.26	0.72	0.78	**0.19**	7.40	1.43	1.17	0.72	2.89	3.48	1.29	1.50	1.97	1.11
8	0.52	0.99	0.51	0.44	0.35	0.43	1.19	**0.22**	0.32	1.33	0.71	0.48	0.71	0.88	1.54	0.71	0.56
9	0.49	0.73	0.45	0.58	0.32	0.42	0.75	0.56	**0.27**	0.74	0.45	0.66	0.57	0.42	0.72	0.54	0.30
10	0.83	0.56	0.43	2.42	0.46	0.40	0.42	3.28	0.92	**0.31**	0.44	1.44	2.02	0.78	0.78	1.03	0.85
11	1.01	0.64	0.55	2.05	0.43	0.33	0.43	2.86	0.77	0.47	**0.29**	1.28	1.51	0.46	0.50	0.91	0.81
12	0.51	1.49	0.67	1.70	0.57	0.75	1.18	0.66	0.43	1.76	0.63	**0.20**	0.30	0.42	1.39	0.84	0.62
13	0.50	1.28	0.82	1.43	0.48	0.67	0.91	0.92	0.45	1.37	0.41	0.41	**0.19**	0.29	0.75	0.73	0.53
14	0.68	0.94	0.61	1.75	0.37	0.39	0.62	2.13	0.48	0.57	0.30	1.00	0.70	**0.17**	0.31	0.74	0.74
15	1.00	0.83	0.68	2.08	0.51	0.44	0.52	2.03	0.79	0.53	0.28	1.14	1.02	0.33	**0.20**	0.83	0.69
avg	0.70	0.71	0.51	2.51	0.49	0.54	0.66	2.77	0.85	0.91	0.58	1.36	1.70	0.81	1.15		
cov	0.34	0.48	0.31	1.26	0.35	0.37	0.47	0.84	0.65	0.50	0.45	0.69	0.77	0.64	0.61		

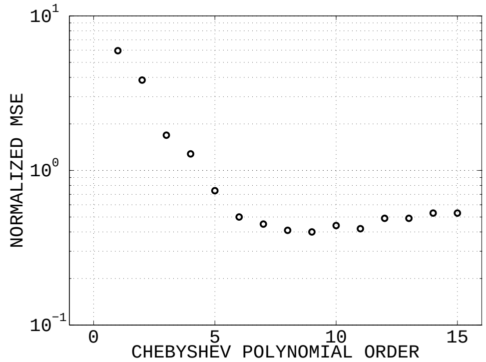

Order	NMSE (%)	Order	NMSE (%)
1	5.95	9	0.40
2	3.84	10	0.44
3	1.69	11	0.42
4	1.28	12	0.49
5	0.74	13	0.49
6	0.50	14	0.53
7	0.45	15	0.53
8	0.41		

Figure 3.5: The normalized mean square error (NMSE) for different Chebyshev polynomial orders for the data set UCB1_15_6. The LHS-figure shows the NMSE in semi-log scale. The RHS-table shows the NMSE values in the figure.

the accuracy of the identification results is negligible with NMSE of 0.34% for $5 \leq n \leq 9$. Therefore, the Chebyshev order $n = 5$ was repeatedly used for all analyzed data sets.

The RFM-identification was performed for all test cases. A sample result of the RFM-identification is shown in Figures 3.4 (b) and (e). The mean and standard deviation of the NMSE are $(1.16 \pm 0.41)\%$, and the NMSE's for all test cases are summarized in the gray cells in Table 3.4 (b).

The normalized Chebyshev coefficients were determined for all test cases (Table 3.5). The coefficients associated with the first order damping, the third order damping, and the first order stiffness are the most dominant terms in the RFM-identification, and the other terms are either negligible or cancel each other out. The means and standard deviations of the dominant Chebyshev coefficients are (716.3 ± 53.5) kN for the first order damping, (-45.05 ± 4.801) kN for the third order damping, and (88.29 ± 38.90) kN for the first order stiffness. A sample normalized Chebyshev coefficients is illustrated in Figure 3.6 (a).

The de-normalized power series coefficients were also calculated using the de Moivre's Theorem (Table 3.5). The means and the standard deviations of the power series coefficients are

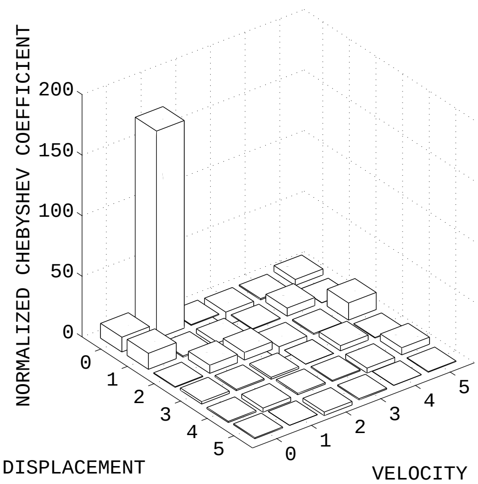

(a) normalized Chebyshev coefficients

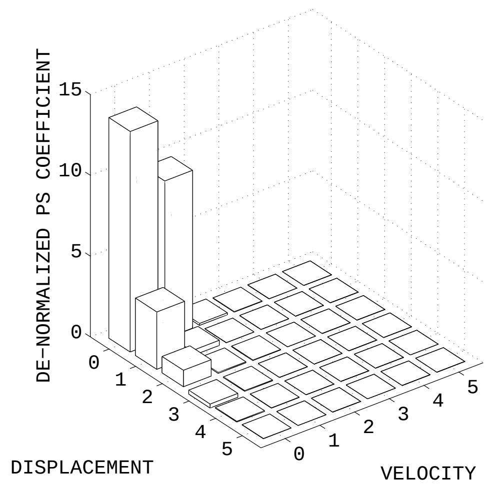

(b) de-normalized power series coefficients

Figure 3.6: An example of normalized Chebyshev coefficients ($\bar{C}_{ij}$) and de-normalized power series coefficients (a_{ij}) for the tested viscous damper (UCB1_15_6).

(1.782 ± 0.234) kN sec/mm for the first order damping, (4.047 ± 2.822) kN sec^3/mm^3 for the third order damping, and (10.72 ± 5.641) kN/mm for the first order stiffness. Unlike the Chebyshev polynomial expansion, the orthogonality property is not valid among the power series terms. A sample de-normalized power series coefficients is shown in Figure 3.6 (b).

Validation

The RFM-identification results were validated using the data sets, which had not been used in the identification phase. A total of 196 (=14×14) validation processes were performed, and the normalized mean-square errors between the measured and estimated forces are summarized in Table 3.4 (b). In the table, the values in one row are the validation errors with respect to one data set, while the values in one column are the validation errors with respect to the same identified normalized Chebyshev coefficients. The means and standard deviations of the averaged

Table 3.5: Normalized Chebyshev coefficients ($\bar{C}_{ij}$) and de-normalized power series coefficients (a_{ij}) of the tested viscous damper for the restoring force method (RFM).

No	Name of data set	$\bar{C}_{01}$	$\bar{C}_{03}$	$\bar{C}_{10}$	a_{01}	$a_{03}(10^{-6})$	$a_{10}(10^{-1})$
1	UCB1_10_4	630.3	−37.89	184.0	2.186	−0.403	25.32
2	UCB1_10_5	621.5	−39.36	85.99	2.000	7.960	9.887
3	UCB1_10_6	669.8	−44.62	95.09	2.310	8.881	9.364
4	UCB1_12_4	669.9	−39.51	122.0	1.716	5.318	17.30
5	UCB1_12_5	707.1	−45.69	81.75	1.810	8.574	9.454
6	UCB1_12_6	683.3	−47.97	40.93	1.865	1.973	5.946
7	UCB1_12_7	684.9	−46.83	99.65	1.884	2.292	7.423
8	UCB1_15_4	739.4	−41.75	120.2	1.651	5.166	17.82
9	UCB1_15_5	727.5	−44.27	63.87	1.578	4.428	8.669
10	UCB1_15_6	761.8	−50.33	58.64	1.710	5.586	6.242
11	UCB1_15_7	756.6	−52.88	128.5	1.755	3.442	9.914
12	UCB1_17_4	767.7	−39.19	88.35	1.610	1.492	14.46
13	UCB1_17_5	770.2	−45.11	63.35	1.538	1.715	7.784
14	UCB1_17_6	781.7	−48.11	53.22	1.564	2.431	6.090
15	UCB1_17_7	772.3	−52.24	38.75	1.554	1.854	5.074
	avg	716.3	-45.05	88.29	1.782	4.047	10.72
	cov	0.075	0.107	0.434	0.131	0.697	0.526

validation errors vary from (1.44 ± 0.43)% to (3.95 ± 1.45)% for the same identified normalized Chebyshev coefficient set, and from (1.74 ± 0.77)% to (2.86 ± 1.01)% for the same data set.

3.4.3 Nonparametric Identification Using Artificial Neural Networks

Training

The artificial neural network (ANN) identification was performed with the measured viscous damper response. Three-layer feedforward neural networks were constructed with 15 nodes in the first layer and 10 nodes in the second layer. The third layer was used as the output layer. The adaptive random search method was employed to train the neural networks with 10 global searches and 500 local searches. Three identical training processes were performed with randomly generated initial weights, and the best identification result (i.e., the result with minimal NMSE) was chosen.

A sample ANN-identification result is illustrated in Figures 3.4 (c) and (f). The mean and standard deviation of the ANN-identification are $(0.25 \pm 0.06)\%$. The NMSE of the ANN-identification for all test cases are summarized in the grayed cells in Table 3.4 (c).

<u>Validation</u>

The trained neural networks using the ANN identification method were validated with the data sets, which had not been used in the training phase. A total of 196 validation processes were performed, and the normalized mean-square errors (NMSE) are summarized in Table 3.4 (c). In the table, the values in one row are the validation error for one data set, and the values in one column are the validation errors for the same trained neural networks. The means and standard deviations of the NMSE vary from $(0.49 \pm 0.17)\%$ to $(2.77 \pm 2.33)\%$ for the same trained neural networks, and from $(0.54 \pm 0.16)\%$ to $(2.24 \pm 2.19)\%$ for the same data set.

3.5 Discussion

3.5.1 Constitutive Law

The frequency-dependent damping properties of the tested viscous damper were studied to investigate the dependence of the estimated peak damper force with the corresponding displacement and velocity range. Figure 3.7 shows that the relationship between the peak force and the peak velocity follows the constitutive law at all tested peak displacements. The identified peak forces are also plotted in the table. The peak forces identified with the SDM ($\bigcirc$) are less than the measured peak forces by 3.0% on average. The peak forces identified with the RFM ($\Box$) are less than the measured peak forces by 5.1% on average, and the peak forces identified with the

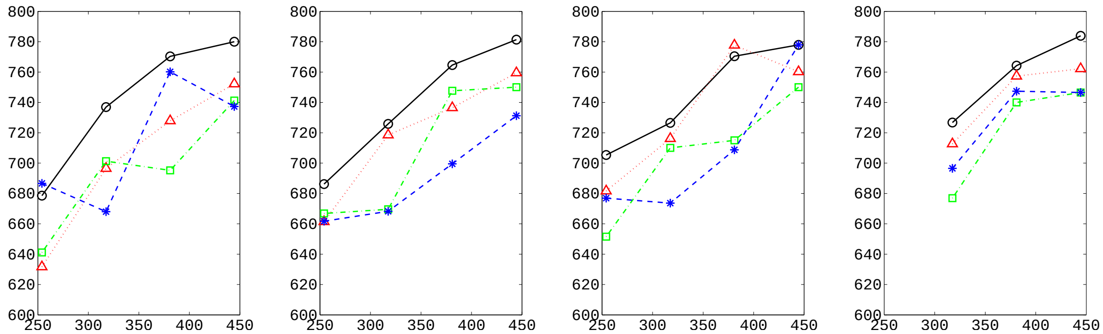

(a) $\pm$101.6 mm (4.0 in) (b) $\pm$127.0 mm (5.0 in) (c) $\pm$152.4 mm (6.0 in) (d) $\pm$177.8 mm (7.0 in)

Figure 3.7: Relationship of peak velocities and peak forces at different peak displacements. ($\bigcirc$: measured, $\triangle$: SDM, $\square$: RFM, $*$: ANN). For each peak displacement level (i.e., (a), (b), (c), and (d)), the x-axis shows the peak velocity and the y-axis shows the force.

ANN ($*$) are less than the measured peak forces by an average of 4.8%. Consequently, the peak force of the tested damper can be identified successfully by using all investigated identification methods.

3.5.2 Fidelity of Identified Models

Parametric Simplified Design Model

The parametric SDM-identification results show that the hysteresis in the velocity-force phase is not modeled accurately (Figure 3.4 (d)), while the damping energy can be modeled accurately in the displacement-force phase plot (Figure 3.4 (a)).

Table 3.3 shows that the identified damping constant (C) and exponent (n) are reasonably close to the design values; the mean of the identified damping constant is 74.37 kN·sec^n/mm^n, which is about 86% of the design value 86.03 kN·sec^n/mm^n; the mean of the exponent is 0.39, which is about 112% of the design value 0.35.

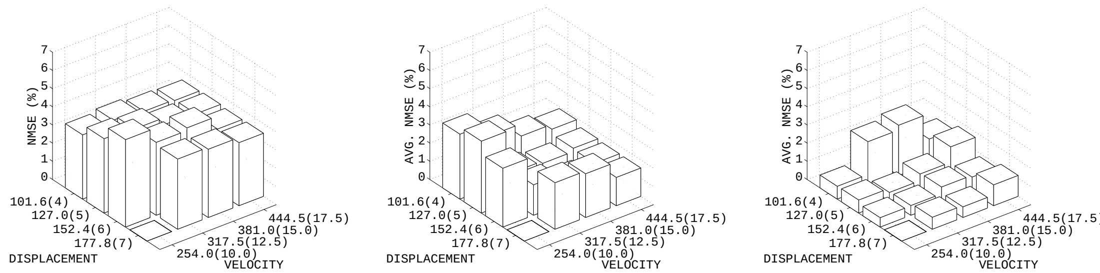

(a) SDM (b) RFM (c) ANN

Figure 3.8: Normalized mean-square errors between the measured and the identified forces with parametric simplified design model (SDM), and non-parametric restoring force method (RFM) and artificial neural networks (ANN). In the figure, the data set for x = 254.0 mm/sec and $\dot{x}$ = 177.8 mm is missing.

Figure 3.8 (a) shows that the NMSE increases as the peak velocity or the peak displacement increases. According to Soong and Dargush (1997), the simplified design model is more appropriate for a lower excitation frequency because of the smaller contribution of relaxation time in the Maxwell equation. Therefore, the NMSE of the SDM-identification increases when the peak velocity increases. In addition, using the simplified design model, because the damper response is modeled as a function of velocity only, the displacement-related nonlinearity of the damper cannot be modeled properly.

Non-parametric Restoring Force Method

In the non-parametric restoring force method (RFM) identification, the response of the damper is modeled relatively accurately (Figures 3.4 (b) and (e)). The NMSE of the RFM-identification is 2.22%, which is less than the 3.75% NMSE of the SDM-identification. Thus, the tested damper is modeled more accurately with the RFM than the SDM. In contrast to the SDM-identification case, the NMSE of the RFM-identification becomes smaller with larger peak velocity (Figure 3.8 (b)). That is, the accuracy of the RFM-identification increases, when the viscous damper is identified using data sets with higher frequency excitations. This result implies that, in the RFM-identification, the tested viscous damper is modeled more accurately with a high frequency excitation.

The normalized Chebyshev coefficients show that the first order damping, third order damping and the first order stiffness terms are the dominant terms in the RFM-identification. The identified force components corresponding to these dominant terms are illustrated in Figure 3.9. Figure 3.9 (a) shows that the first order damping coefficient ($\bar{C_{01}}$) is the most important one in modeling the damping energy. Figure 3.9 (d) shows that the "effective" damping constant of the viscous damper is modeled by the $\bar{C}_{01}$. Therefore, the damping characteristics of the viscous damper are mainly governed by the first order damping coefficient.

The plot in Figure 3.9 (e) clearly shows the nonlinear characteristic of the viscous damper. As summarized in Table 3.5, the third order Chebyshev coefficient ($\bar{C}_{03}$) has a negative value for all test cases. The negative value is due to the "softening" of the damping force ($\alpha < 1$). Had the tested viscous damper had linear or "hardening" characteristics, the third order damping coefficient would have been close to zero, or have taken a positive.

Figure 3.9 (c) shows that the contribution of the $\bar{C}_{10}$ to the total damping energy is negligible, as indicated by the slight slope. However, Figure 3.9 (e) reveals that the first order stiffness coefficient is important to model the damper hysteresis in the velocity-force phase plot.

Figure 3.10 shows the $\bar{C}_{01}$ and $\bar{C}_{03}$ coefficients at different peak velocities and peak displacements. The $\bar{C}_{01}$ increases by 20.8% on average, as the peak velocity increases (Figure 3.10 (a)), while the $\bar{C}_{01}$ remains constant for different displacements (Figure 3.10 (b)). These results imply that the nonlinearity of the first order damping depends on the peak velocity, rather than

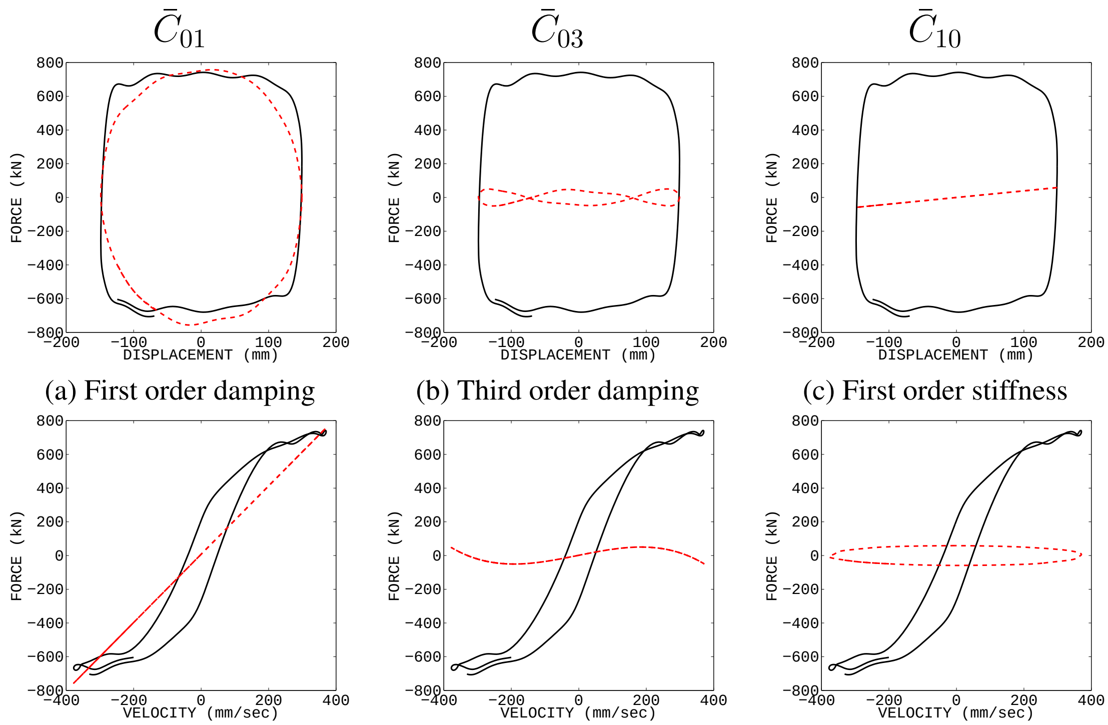

(a) First order damping (b) Third order damping (c) First order stiffness

(d) First order damping (e) Third order damping (f) First order stiffness

Figure 3.9: Sample phase plots for the first order damping, the third order damping and the first order stiffness terms of the identified force using the restoring force method. The solid line represents the measured (total) force and the dashed line represents the termwise identified force. The first row shows the relationship between displacement and force, and the second row shows the relationship between velocity and force.

the peak displacement. As was previously shown, in the RFM-identification, the "effective" damping constant of the damper is mainly modeled by the first order damping term. Consequently, these results also imply that the "effective" damping constant varies with different peak velocities, rather than with different peak displacements.

The $\bar{C}_{03}$ decreases about 20.7% on average as the peak displacement increases (Figure 3.10 (d)), while the $\bar{C}_{03}$ remains constant at different peak velocities (Figure 3.10 (c)). Therefore, unlike the $\bar{C}_{01}$, the nonlinearity of the third order damping depends on peak displacement, rather than peak velocity. Previously, it was also shown that the softening of the damper is modeled

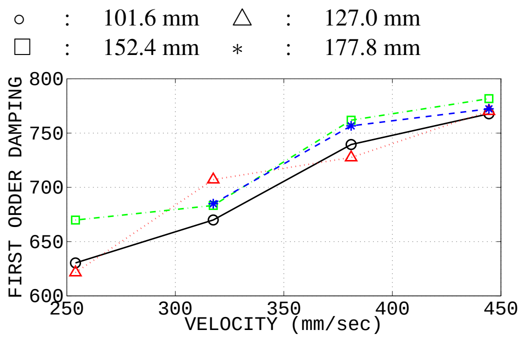

(a) Peak vel vs. 1^{st} order damping coef.

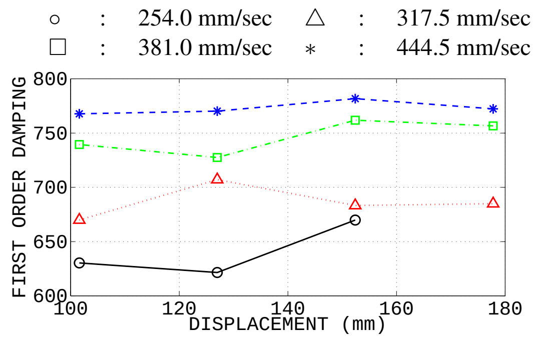

(b) Peak disp vs. 1^{st} order damping coef.

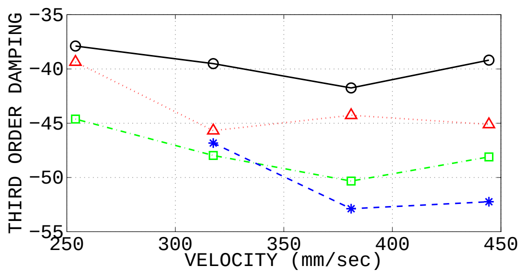

(c) Peak vel vs. 3^{rd} order damping coef.

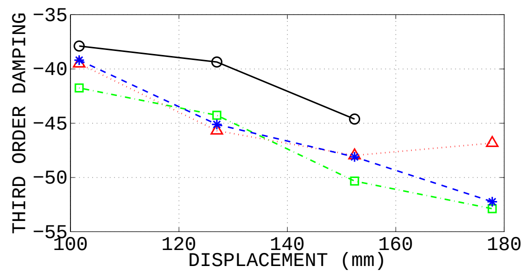

(d) Peak disp vs. third order damping coef.

Figure 3.10: The normalized Chebyshev coefficients of the first and third order damping at different peak velocities and peak displacement, respectively. (a) and (c) show the relationship between peak velocity and the normalized Chebyshev coefficient for different peak displacements. (b) and (d) show the relationship between peak displacement and the normalized Chebyshev coefficient for different peak velocities.

with the $\bar{C}_{03}$ in the RFM-identification. Therefore, the decrease of the $\bar{C}_{03}$ at a larger peak displacement would imply that the magnitude of the damper's softening increases as the peak displacement increases.

Non-parametric Artificial Neural Networks

In the non-parametric artificial neural networks (ANN) identification, the response of the tested viscous damper is modeled fairly accurately (Figures 3.4 (c) and (f)). With the given identification parameters, the NMSE of the ANN-identification is the smallest among the investigated identification methods. In the training phase, the averaged NMSE of the ANN identification is

0.23%, which is approximately five times less than the averaged NMSE of the RFM in identification phase, 1.16%. The ratio of the NMSE in the validation phase to the NMSE in the training phase (NNMSE) of the ANN is not as that of the RFM. The averaged NNMSE of the ANN is 4.45, and the averaged NNMSE of the RFM is 2.20. This result shows that the relative accuracy of the ANN in the validation phase is less than the corresponding accuracy of the RFM.

Computation Time

A fair comparison of computation times of the investigated methods is difficult, because the computation time is a complicated function of many parameters used in each method. However, it was noticed that the optimization-based methods (the SDM and the ANN) require a longer computation time than the quadrature-based method (the RFM) due to the fundamental differences in the identification methods. In general, the optimization-based methods would require more time, when the error surface is more complex.

3.5.3 Identification Using the Data Sets with Concatenated Sinusoidal Excitation

Using a single-frequency sinusoidal excitation, the dynamic response of a linear system can be fully identified. However, for a nonlinear system, such as the nonlinear viscous damper under discussion, the dynamic characteristics, in general, can not be accurately identified with a single-frequency sinusoidal excitation, since the dynamic response depends on the amplitude and frequency of the excitation. On the other hand, for a full-scale viscous damper, using a broadband random excitation (which is much better from the identification point of view) could generate an excessive amount of heat for an extended testing period.

An alternative way to identify a nonlinear viscous damper is to use combined data sets of the damper responses for multiple single-frequency sinusoidal excitation. The combined data set can be obtained by concatenating multiple sets of damper response with different frequency and amplitude characteristics. Because the time sequential order of the combined data set should not affect the identification results, the combined data are randomly shuffled in time. Identification approaches that use error functions based on the solution of the governing differential equations require sequential ordering in time of the measured data and simulated ones. However, if "static" data comparison is used (i.e., by directly using the assumed model form), then the elements of the reference data set can be arbitrarily shuffled in time.

The influence on the identification results when using the time-shuffled concatenated data was studied. A concatenated data set was prepared by adding 14 data sets (among a total of 15 data sets) in series, and the time-order of the concatenated data set was randomly shuffled. The RFM- and ANN-identifications were performed using the concatenated data set. The RFM- and ANN-identification was validated with the data set, which had not been used in the identification (or training) phase. The same procedures were repeated to validate the RFM- and ANN-identification results using all 15 tested data sets. A sample validation result for the RFM and the ANN is shown in Figure 3.11.

In the RFM, the mean and standard deviation of the averaged NMSE is $(1.39 \pm 0.28)\%$ for the identification and $(2.46 \pm 1.42)\%$ for the validation. In the ANN, the mean and standard deviation of NMSE is $(0.43 \pm 0.06)\%$ for the training and $(0.64 \pm 0.23)\%$ for the validation. In the identification (or training) phase, the averaged NMSE with concatenated data set is greater than that with the single data set: for the RFM, $(1.16 \pm 0.41)\%$ with single data set and $(1.39 \pm 0.28)\%$

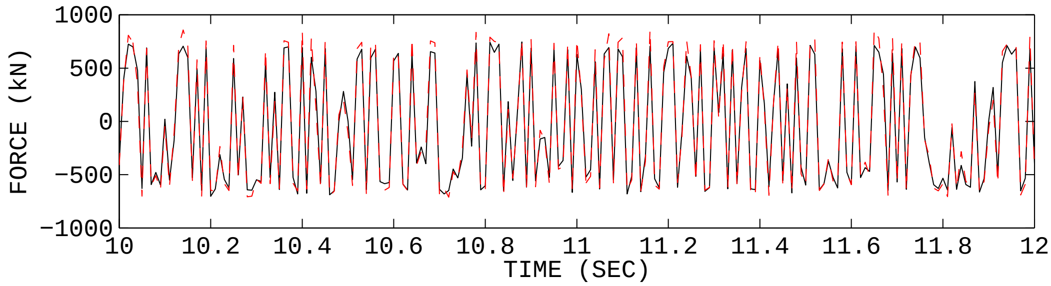

(a) Restoring force method (RFM)

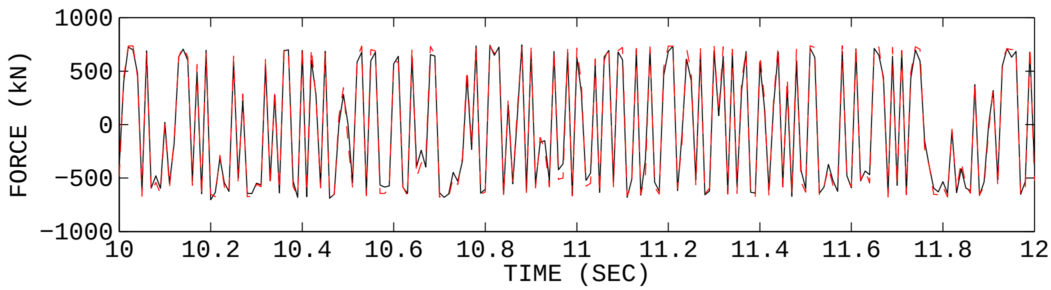

(b) Artificial neural networks (ANN)

Figure 3.11: The "static" validation results of the RFM-identification (a) and ANN-identification (b) procedures for the data set UCB1_15_6 randomly shuffled in its sequential order. The solid line is for the measured force, and the dashed line is for the identified force.

with the concatenated data set, and for the ANN, $(0.25 \pm 0.06)\%$ with single data set and $(0.43 \pm 0.06)\%$ with the combined data sets. In the validation phase, however, the averaged NMSE with the concatenated data set for the ANN is less than that with single data set, while the averaged NMSE's with single and concatenated data sets for the RFM are approximately the same: for the RFM, $(2.22 \pm 0.85)\%$ with single data set and $(2.46 \pm 1.42)\%$ with concatenated data set, and for the ANN, $(1.08 \pm 0.72)\%$ with single data set and $(0.64 \pm 0.23)\%$ with concatenated data set. The averaged NMSEs with single and concatenated data sets are summarized in Table 3.6. Note that the accuracy of the ANN identification model to generalize; increases with the combined data set, while the accuracy of the RFM identification is not improved with the concatenated data set.

Table 3.6: The averaged normalized mean-square error of the restoring force method (RFM) and the artificial neural networks (ANN) identifications using a single and concatenated damper response data sets. The table shows the mean and standard deviation of the averaged normalized mean-square error.

Phase	Restoring force method				Artificial neural networks			
	Single		Concat.		Single		Concat.	
	mean	stdv	mean	stdv	mean	stdv	mean	stdv
Identification	1.16	0.41	1.39	0.28	0.25	0.06	0.43	0.06
Validation	2.22	0.85	2.46	1.42	1.08	0.72	0.64	0.23

3.5.4 Significance of Inertia Effects

The quasi-static approximation in Equation 3.6 is valid when the inertia effect is negligible in the dynamic response of the damper. The peak velocity of the excitation used in this study is within the range of 254.0 mm/s to 444.5 mm/s (10.0 in/s to 17.5 in/s), which is greater than the typical excitation velocity in a quasi-static testing, 3 mm/s to 5 mm/s (0.12 in/s to 0.20 in/s). Therefore, the significance of the inertia effect to the damper response should be evaluated.

The significance of the inertia effects was assessed, using the SDM-identification method; a formal parametric identification procedure was performed in which the governing differential equation of motion was directly solved through the use of conventional time-marching techniques. The mass term was explicitly included in the governing equations, and the damper restoring force was modeled by the expression of Equation 3.1. Table 3.7 shows the significance of the inertia effects at different peak velocities and peak displacements. For all 15 data sets, the variability of the identified mass around the mean value of 735.6 kg is 31.9%. It is important to note that the “effective” mass in the actual tests includes not only the weight of the moving internal components of the damper and a portion of the squeezed fluid, but also a part of the

Table 3.7: Estimated significance of inertia effects in the SDM-identification. In the table, $||\hat{f}||$ is the norm of the SDM-identified force, $||\hat{f}_{\ddot{x}}||$ is the norm of the inertia term of the SDM-identified force, and $||f||$ is the norm of the measured force.

No	Name of data set	Mass (kg)	$\|\|\hat{f}_{\ddot{x}}\|\|/\|\|\hat{f}\|\|$ (%)	$\|\|\hat{f}_{\ddot{x}}\|\|/\|\|f\|\|$ (%)
1	UCB1_10_4	567.7	0.0504	0.0524
2	UCB1_10_5	1199.6	0.0841	0.0902
3	UCB1_10_6	1208.4	0.0685	0.0730
4	UCB1_12_4	685.9	0.0835	0.0877
5	UCB1_12_5	777.9	0.0763	0.0811
6	UCB1_12_6	869.8	0.0704	0.0746
7	UCB1_12_7	974.9	0.0698	0.0743
8	UCB1_15_4	567.7	0.0951	0.0990
9	UCB1_15_5	594.0	0.0786	0.0819
10	UCB1_15_6	785.2	0.0852	0.0942
11	UCB1_15_7	645.1	0.0611	0.0642
12	UCB1_17_4	494.7	0.1060	0.1104
13	UCB1_17_5	522.5	0.0895	0.0930
14	UCB1_17_6	519.5	0.0759	0.0784
15	UCB1_17_7	621.7	0.0776	0.0810
	avg	735.6	0.0781	0.0824
	cov	0.319	0.17	0.17

external hardware attachments utilized in performing the test. Once the "effective" moving mass was identified, the significance of the inertia term was measured as

$$\frac{||\hat{f}_{\ddot{x}}||}{||\hat{f}||} \times 100(\%), \qquad \frac{||\hat{f}_{\ddot{x}}||}{||f||} \times 100(\%) \tag{3.11}$$

where $||\hat{f}_{\ddot{x}}||$ is the norm of the inertia term of the identified force, $||\hat{f}||$ is the norm of the identified force, and $||f||$ is the norm of the measured force. The significance of the inertia effects is also summarized in Table 3.11 for all test cases. The mean of the $||\hat{f}_{\ddot{x}}||/||\hat{f}||$ is 0.0781% with the coefficient of variance of 0.17. The mean of $||\hat{f}_{\ddot{x}}||/||f||$ is 0.0824% with the coefficient of variance of 0.17. Therefore, the induced inertia forces are negligible, confirming the earlier conclusion to ignore inertia terms.

3.6 Summary and Conclusions

The goal of this study was to investigate the applicability of a set of parametric and non-parametric identification methods to measurements obtained from a full-scale nonlinear viscous damper. Such models can be used for structural health monitoring purposes. Two non-parametric identification methods, the restoring force method and the artificial neural networks, were studied and the results were compared with the parametric simplified design model of the full-scale viscous damper. The nonlinear full-scale viscous damper used in this study was successfully identified with the simplified parametric model, as well as with the restoring force method and the artificial neural networks. The identification results show that the normalized Chebyshev coefficients can be used to interpret the nature and relative contribution of the linear and non-linear characteristics of the viscous damper. A comparison of the investigated identification methods is shown in Table 3.8.

Table 3.8: A comparison of investigated system identification methods for applications in structural health monitoring.

Identification Methods	Advantages	Disadvantages
Simplified Model (parametric)	- Most accurate if the exact system model is known. - Direct physical interpretation is possible using the identified parameters.	- *A priori* knowledge of the system is required. - The identified parameters become significantly biased when the initial model is incorrect.
Restoring Force Method (non-parametric)	- No *a priori* knowledge of the system is required. - The same model can be used when the system changes into different nonlinear classes. - It is applicable to a wide range of nonlinearities. - Both Chebyshev and power series coefficients can be identified. - Physical interpretation of some of the identification results is possible with identified coefficients.	- The identification yields an approximating model. - Only limited physical interpretation of identification results is possible.
Artificial Neural Networks (non-parametric)	- No *a priori* knowledge of the system is required. - It is applicable to a wide range of nonlinearities. - Change detection of the system is possible through monitoring the regression error of the trained networks.	- Change detection is possible, but physical interpretation of the detected changes are not generally possible.

Chapter 4

Data-Driven Methodologies for Change Detection in Large-Scale Nonlinear Dampers with Noisy Measurements

4.1 Introduction

4.1.1 Motivation

Large-scale orifice viscous dampers are frequently used in modern civil structures to mitigate seismic or wind-induced vibration. Among various types of dampers, orifice viscous dampers (hereinafter viscous dampers) provide excellent efficiency of energy dissipation — the orifice damper employs small orifices on its piston head, so that the silicon fluid sealed inside the damper chamber is forced to pass through the orifices when the damper piston reciprocates. Consequently, the dynamic properties of an orifice viscous damper largely depend on the geometric characteristics of the orifice design. Soong and Constantinou (1994) and Soong and Dargush (1997) provide detailed descriptions of orifice viscous dampers.

Due to their importance in applications involving civil structures, many government agencies require a series of quality assurance tests for large-scale dampers before the dampers are installed in actual civil structures (HITEC, 1996, 1998a,b, 1999). After installation, the condition assessment of the installed dampers is commonly performed in two ways: visual inspection, and monitoring the internal pressure of the damper's silicon fluid. First, visual inspection is usually conducted by trained inspectors, searching for noticeable damage on the damper surface, often evident by fluid leakage. The second method employs a pressure gauge to measure the internal pressure levels of the dampers. Thus, with a pressure change, the inspectors can presume that the damper has changed during the operation. If the pressure change were significant, the damper would be removed from the structure and delivered to testing facilities to find possible causes of the change. However, none of the current practices are adequate for reliable condition assessment. The visual inspection is often subjective. Although pressure monitoring is obviously a more advanced method than visual inspection, the direct relationships between the pressure level and engineering characteristics of the nonlinear dampers are difficult to identify. Moreover, no current practices of damper monitoring are appropriate when a number of dampers are employed in a structure. For example, after a major seismic retrofit of the west spans of the San Francisco Oakland Bay Bridge in 2004, more than 100 large-scale viscous dampers are employed. In this case, more systematic and efficient condition assessment methodologies are required.

As an alternative approach for damper condition assessment, a vibration-based structural health monitoring technique is proposed in this study. Yun et al. (2007) demonstrated that the non-parametric Restoring Force Method (RFM) is a very promising tool for the condition assessment of large-scale nonlinear viscous dampers. Comparing one parametric (the simplified damper design model) and two non-parametric identification methods (the Restoring Force

Method and Artificial Neural Networks), they demonstrated that the RFM has significant advantages than other methods because (1) no *a priori* knowledge of the system is needed, (2) the same non-parametric model is applicable to a wide-range of nonlinearities, and (3) the physical interpretation of the identification results is possible, which is generally impossible with other non-parametric identification methods, such as Artificial Neural Networks.

Recent progress in sensing and internet-based data communication technologies allow the development of real-time remote monitoring systems for civil infrastructure system. Yun et al. (2007) have developed a reliable real-time web-based continuous bridge monitoring system that has been applied to a critical bridge (the Vincent Thomas Bridge) in the Los Angeles, California, metropolitan region to perform forensic studies of various earthquakes, as well as a recent ship-bridge collision. Therefore, by combining the technology of a web-based monitoring system with the Restoring Force Method, a feasible methodology can be developed for a real-time remote condition assessment of large-scale nonlinear viscous dampers.

In the development of the monitoring system, the following practical and challenging problems must be considered: First, the effects of measurement noise on the results of change detection must be considered, since sensor readings can be more significantly affected by noise in the *in-situ* measurements than in laboratory testing, due to various sources of noise. In many cases of *in-situ* monitoring, only the displacement or acceleration is measured, depending on the measurement feasibility, and then other necessary response states are numerically obtained through digital signal processing techniques using the measured response. In such cases, the effects of measurement noise are not simply additive, and propagate throughout the response states, which are numerically obtained from noisy measurements. Consequently, the developed methodology should be able to deal with those complicated noise effects. Second, the results of the change detection will be affected by the measurement uncertainty. Therefore, the uncertainty of the detected change due to the measurement noise must be quantified for reliable condition assessment. However, the uncertainty quantification requires multiple tests, which is not usually possible for the *in-situ* monitoring due to lack of control of excitation sources. Even if one had the control of the excitation, performing multiple tests with full-scale viscous dampers is extremely difficult because of an enormous amount of heat converted from the dissipated energy.

Having the proposed condition assessment methodology will provide contributions in the following three ways:

1. Enabling the interpretation of physical significance of detected changes, one can quantify the significance of the changes at the full-structure level as well as at the component level. This attribute remains even when the dampers' evolving properties change into different classes of nonlinearity, due to various types of deterioration.

2. With more reliable condition assessment methodologies, one can minimize unnecessary removal of undamaged dampers. Damper removal from civil structures is time-consuming and expensive due to their large physical size.

3. Since the methodology proposed in this study is data-driven and model independent, the same approach is applicable to other types of nonlinear components, such as different types of energy dissipating devices, base isolators, and nonlinear joints.

4.1.2 Objective

The objective of this study is to develop a data-driven methodology for change detection in large-scale nonlinear viscous dampers. A joint study was performed between the University of Southern California (USC), the University of California at San Diego (UCSD) and the University of California at Berkeley (UCB). Three different large-scale nonlinear viscous dampers were tested at UCB and UCSD. The damper experiments were designed to introduce different types of nonlinearity in a systematic way. Three large-scale viscous dampers used in the experimental study involved different nonlinear features. In the experiments, two different excitation types were tested, including monotonic sinusoidal and broadband random excitations.

Using the experimental results, an analytical study was performed at USC. A data-driven change detection methodology for the tested large-scale dampers was investigated using the non-parametric Restoring Force Method. In order to study the effects of measurement uncertainty, the damper data were intentionally polluted with random noise. As a statistical data recycling technique, the Bootstrap method was investigated for uncertainty quantification, even with insufficient data for meaningful statistical inferences. Using the developed change detection methodology, the aim was to achieve the following:

1. Ability to detect even small (genuine) changes in the nonlinear dampers;

2. Ability to interpret the physical meaning of detected changes; and

3. Ability to quantify the uncertainty associated with the detected changes.

4.1.3 Scope

This chapter is organized as follows: the experimental studies using three large-scale nonlinear dampers are discussed in Section 4.2; the data-driven identification approach using the Restoring Force Method is discussed in Section 4.3; the uncertainty estimation and statistical change detection of the large-scale viscous dampers are discussed in Section 4.4; and the Bootstrap method as a data recycling technique and its uncertainty estimation are discussed in Section 4.5.

4.2 Experimental Studies

4.2.1 Test Apparatus

Three different large-scale nonlinear viscous dampers were tested at two different test facilities: the 66.7 kN (15 kip) viscous damper was tested at the Earthquake Engineering Research Center (EERC) of the University of California, Berkeley (Figure 4.1 (a)), and the 2001.6 kN (450 kip) and 2891.3 kN (650 kip) viscous dampers were tested at the Seismic Response Modification Device (SRMD) facility of the University of California, San Diego (Figure 4.1 (b)).

The 66.7 kN damper with the maximum velocity of 431.8 mm/sec (Damper A) has the smallest size among the tested dampers in this study. The damper was designed using a simplified Maxwell model (Constantinou and Symans, 1993; Constantinou et al., 1993; Den Hartog, 1956; Makris and Constantinou, 1991; Makris et al., 1993) as

$$r(x, \dot{x}) = C \ \mathrm{sgn}(\dot{x})|\dot{x}|^n \tag{4.1}$$

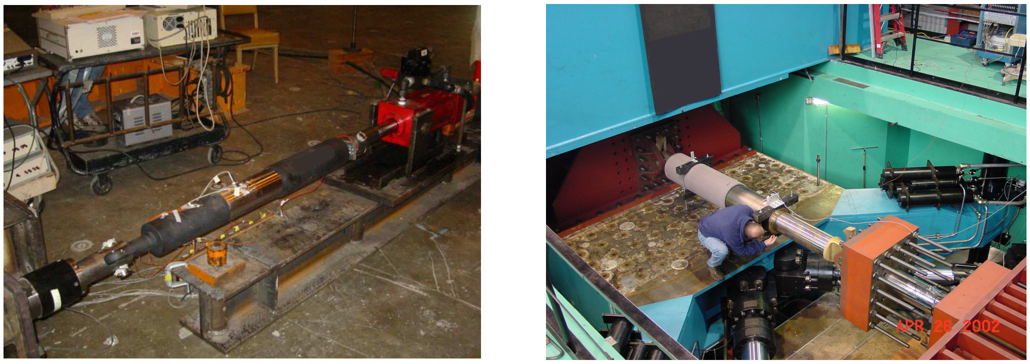

(a) Test at the University of California, Berkeley (UCB)

(b) Test at the University of California, San Diego (UCSD)

Figure 4.1: Test facilities for large-scale viscous dampers at the University of California, Berkeley(UCB), and the University of California, San Diego (UCSD) used in this study.

where r is the restoring force, C is the damping constant, and n is the nonlinear damping exponent. This simplified design model is valid when the excitation frequency is low. In this case, the inertia term of the damper response becomes insignificant, and consequently, $f(t) \approx r(x, \dot{x})$, where f is the measured force. Yun et al. (2007) demonstrated that the inertia term of the large-scale damper response would be negligible at a low velocity. The design parameters of Damper A are $C = 1.12$ kN $\cdot$ sec^n/mm^n and $n = 1.0$, which makes the damper response approximately linear. The 2001.6 kN damper at the maximum velocity of 215.9 cm/sec (Damper B) was designed with the parameters $C = 398.93$ kN$\cdot$sec^n/cm^n and $n = 0.3$. The 2891.3 kN damper at the maximum velocity of 40.6 cm/sec (Damper C) was designed with $C = 957.44$ kN$\cdot$sec^n/cm^n and $n = 0.3$. Hence, the restoring force of Dampers B and C will be "softening" with $n < 1.0$.

4.2.2 Test Protocols and Preliminary Data Processing

Test with Damper A

Damper A was subjected to broadband random excitation with a lowpass cutoff frequency of 5.0

Hz. During the experiment, the acceleration ($\ddot{x}$) and force (f) of the damper were measured with a sampling frequency of 1 kHz. The measured force of Damper A under broadband random excitation is shown in Figure 4.2 (a). Once $\ddot{x}$ and f were measured, preliminary data processing was performed to obtain the displacement (x) and velocity ($\dot{x}$) required for the damper identification. The data processing was performed in accordance with the following procedures:

1. The measured $\ddot{x}$ and f were de-trended and zero-phase filtered with the cutoff frequencies of 0.1 $\sim$ 10.0 Hz, and a cosine-tapered window was applied to the time-histories of $\ddot{x}$ and r.

2. The filtered $\ddot{x}$ was integrated to obtain the corresponding velocity $\dot{x}$. The same filter and time-history window were applied to $\dot{x}$.

3. The processed $\dot{x}$ was numerically integrated to obtain the corresponding displacement x. The same filter and time-history window were also applied to x.

The test protocols, preliminary data processing and phase plots of the resulting Damper A response are summarized in Table 4.1.

Test with Dampers B and C

Dampers B and C were subjected to monotonic sinusoidal excitation with an excitation frequency of 0.2 Hz for both dampers. Unlike Damper A, x and f (but not the $\ddot{x}$) were measured during the experiments. The sampling frequency of the measurement was 100 Hz. Figures 4.2 (b) and (c) show the measured force of Dampers B and C, respectively. In the figures, notice that the force amplitude of Damper B is constant, while that of Damper C decreases. Both dampers were subjected to the sinusoidal excitation with a constant frequency and constant peak amplitudes over time.

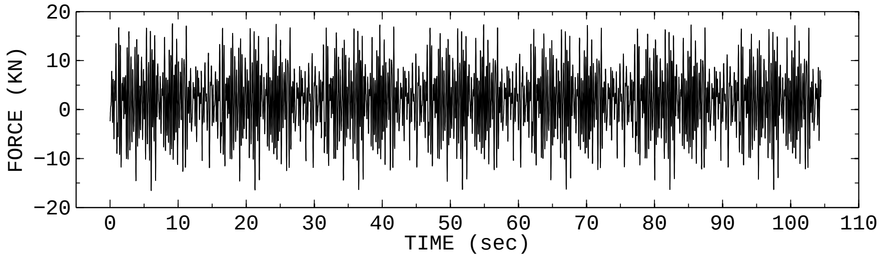

(a) Damper A (close to linear and time-invariant)

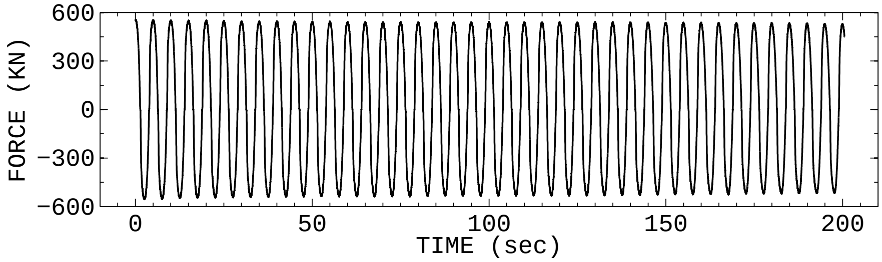

(b) Damper B (damping "softening" and time-invariant)

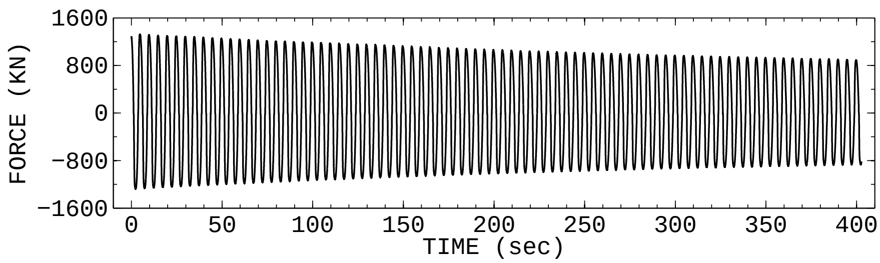

(c) Damper C (damping "softening" and time-varying)

Figure 4.2: Time histories of the measured forces for different large-scale nonlinear viscous dampers with displacement-controlled excitations. (a) The force of Damper A was measured under broadband random excitation. (b) The force of Damper B was measured under monotonic sinusoidal excitation with a constant frequency of 0.2 Hz and constant peak amplitudes of ± 50.8 mm. (c) The force of Damper C was measured under monotonic sinusoidal excitation with a constant frequency of 0.2 Hz and constant peak amplitudes of ± 25.4 mm.

Once x and f are measured for Dampers B and C, preliminary data processing was performed to obtain the velocity ($\dot{x}$) using the following procedures:

1. The measured x and f were de-trended and zero-phase filtered with the cutoff frequencies of 0.05 $\sim$ 5.0 Hz. Then, a cosine-tapered window was applied to the time histories of the filtered response, x and f.

2. The displacement x was differentiated to obtain the corresponding $\dot{x}$. The same filter and time-history window were applied to the obtained $\dot{x}$.

The test protocols, preliminary data processing and phase plots of Dampers B and C are summarized in Table 4.1.

4.3 Non-Parametric Identification

4.3.1 Overview of Restoring Force Method

The Restoring Force Method (RFM) is a non-parametric identification method for nonlinear systems, using a series expansion of two-dimensional Chebyshev polynomials (Masri and Caughey, 1979). Using the RFM, the restoring force of a single-degree-of-freedom (SDOF) nonlinear dynamic system can be modeled as

$$r(x, \dot{x}) = \sum_{i=0}^{P} \sum_{j=0}^{Q} \bar{C}_{ij} T_i(\bar{x}) T_j(\bar{\dot{x}}) \tag{4.2}$$

where $r(x, \dot{x})$ is the restoring force of the nonlinear dynamic system, $\bar{C}_{ij}$ is the normalized Chebyshev coefficient, $T_i(\bullet)$ is the i^{th} order Chebyshev polynomial, P and Q are the highest orders of the Chebyshev polynomial of the normalized displacement ($\bar{x}$) and velocity ($\bar{\dot{x}}$), respectively, within the range of [-1, 1].

Once the $\bar{C}_{ij}$ are identified, the $\bar{C}_{ij}$ can be converted into the equivalent power series coefficients using the following relationship (Mason and Handscomb, 2003):

$$T_0(y) = 1, \quad T_1(y) = y, \quad T_2(y) = 2y^2 - 1, \ldots, \quad T_{k+1}(y) = 2yT_k(y) - T_{k-1}(y), \ldots \tag{4.3}$$

Table 4.1: Summary of test protocols and preliminary data processing parameters for the three large-scale nonlinear viscous dampers used in this study.

Parameters	Damper A	Damper B	Damper C
Nominal output force kN (kips)	66.7 (15)	2001.6 (450)	2891.3 (650)
Max. velocity rating cm/s (ips)	43.2 (17)	215.9 (85)	40.6 (16)
Designed parameters for damping, kN (sec/cm)^n	$C = 1.12$, $n = 1.0$	$C = 398.93$, $n = 0.3$	$C = 957.44$, $n = 0.3$
Excitation type	Broadband random	Monotonic sinusoidal	Monotonic sinusoidal
Excitation frequency	≤ 5.0 Hz	0.2 Hz	0.2 Hz
Nonlinearity	Close to linear	Polynomial, hysteretic	Polynomial, hysteretic
Time-invariancy	Time-invariant	Time-invariant	Time-varying
Measured response	$\ddot{x}$, f	x, f	x, f
Performed Data processing	Integration for $\dot{x}$ Double integration for x	Differentiation for $\dot{x}$	Differentiation for $\dot{x}$
x vs. f	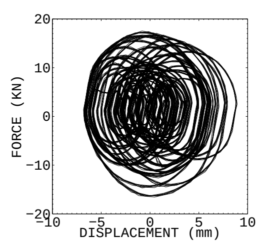	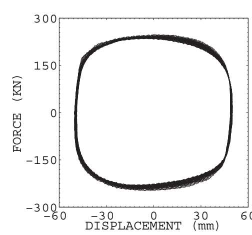	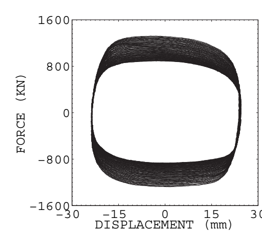
$\dot{x}$ vs. f	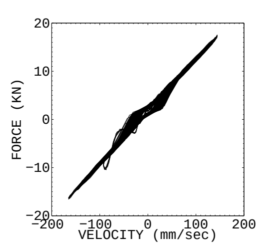	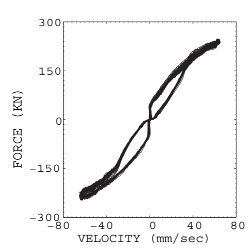	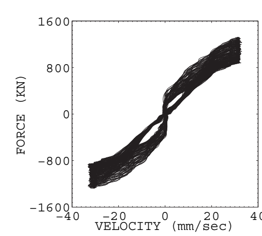

The converted power series coefficients are called the normalized power series coefficients ($\bar{a}_{ij}$). With the de-normalization of $\bar{x}$ and $\bar{\dot{x}}$, the de-normalized power series coefficients (a_{ij}) can be obtained. Using these coefficients, Equation 4.2 can be also expressed as

$$r(x, \dot{x}) = \sum_{i=0}^{P} \sum_{j=0}^{Q} \bar{C}_{ij} T_i(\bar{x}) T_j(\bar{\dot{x}}) = \sum_{i=0}^{P} \sum_{j=0}^{Q} \bar{a}_{ij} \bar{x}^i \bar{\dot{x}}^j = \sum_{i=0}^{P} \sum_{j=0}^{Q} a_{ij} x^i \dot{x}^j \tag{4.4}$$

4.3.2 Identification of Nonlinear Viscous Dampers

It was known that the force characteristics for Dampers A and B do not change over time under stationary displacement-controlled excitation. For example, as shown in Figure 4.2 (b), the measured force of Damper B is *stationary* over time under the *stationary* sinusoidal excitation with a constant frequency of 0.2 Hz and constant peak amplitudes of ±50.8 mm. Consequently, since the outputs (i.e., measured force) of Dampers A and B do not depend explicitly on time, the dampers are *time-invariant systems* under *stationary* excitation. On the other hand, as shown in Figure 4.2 (c), the measured force of Damper C decreases over time although the sinusoidal excitation has a constant frequency of 0.2 Hz and constant peak amplitudes of ±25.4 mm. Hence, Damper C is a *time-varying system* since the output of Damper C depends on time under *stationary* excitation. For these two classes of nonlinear systems (time-invariant and time-varying), different procedures were applied in the damper identification. Detailed identification procedures for each class are described below.

Identification results of time-invariant systems

Using the *time-invariant* systems of Dampers A and B, the RFM identification was applied for the entire domain of the measured time histories. In both cases, the order of the series expansion

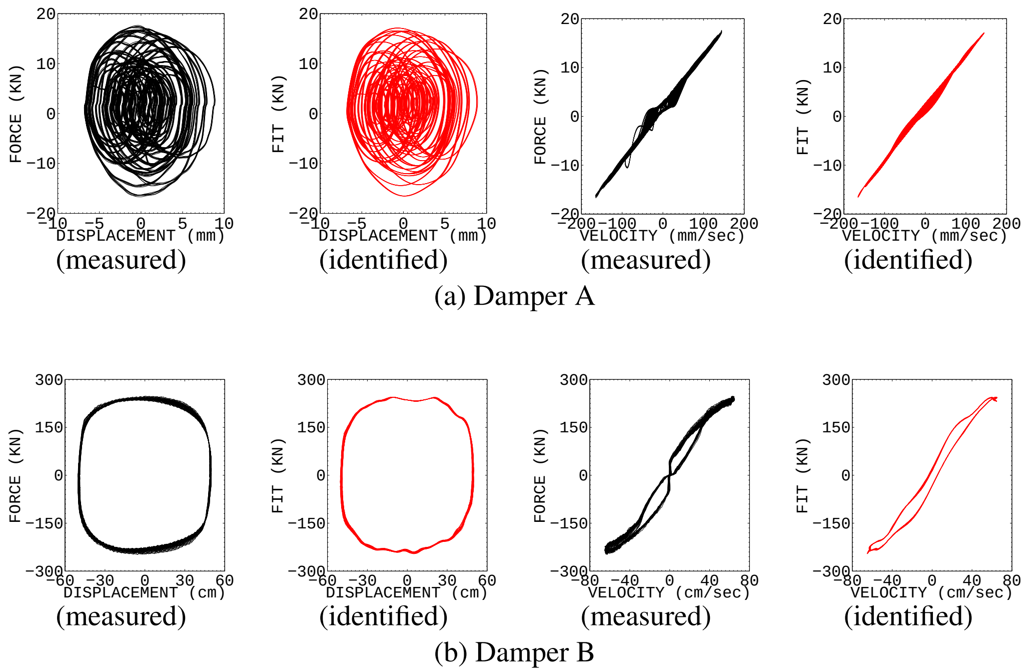

Figure 4.3: The identification results for Dampers A and B using the Restoring Force Method.

was five. The identification results for Dampers A and B are shown in Figure 4.3. The quality of the RFM identification was measured with the normalized mean-square errors (NMSE) as

$$\text{NMSE} = \frac{1}{n\sigma_f^2}\sum_{i=1}^{n}(f_i - \hat{f}_i)^2 \tag{4.5}$$

where n is the number of data points, f is the measured force, $\hat{f}$ is the identified force, and σ_f is the standard deviation of the measured force (Worden and Tomlinson, 2001). Considering Damper A, excellent identification results were obtained with the NMSE of 0.82% as illustrated in Figure 4.3 (a). For Damper B, "softening" hysteresis were successfully identified (Figure 4.3 (b)). However, the identification failed to accurately model the nonlinearity near the damper's neutral position (i.e., $x \approx 0$ and $\dot{x} \approx 0$). The NMSE for the Damper B identification was 3.0%.

The identified RFM coefficients for Dampers A and B are summarized in Table 4.2. For the normalized Chebyshev coefficients ($\bar{C}_{ij}$), the first order damping coefficient ($\bar{C}_{01}$) is dominant for both Dampers A and B: 27.99 for Damper A and 257.00 for Damper B. Notice that Damper B is designed for a larger damping capacity than Damper A (refer Table 4.1). The third order damping coefficient of Damper B ($\bar{C}_{03} = -13.17$) is negative because the designed damping exponent is less than one ($n = 0.3$), while the $\bar{C}_{03}$ of Damper A is close to zero ($\bar{C}_{03} = 0.30$) because Damper A was designed for $n = 1.0$ (Equation 4.1). The stiffness-related coefficients ($\bar{C}_{10}$ for the linear stiffness and $\bar{C}_{30}$ for the cubic stiffness) are relatively small compared to the damping coefficient ($\bar{C}_{01}$) for both dampers, which indicates that the contribution of the stiffness terms is less significant in the identification than the damping terms (i.e., $\bar{C}_{01}$ and $\bar{C}_{03}$). These results are reasonable for viscous dampers.

The identified power series coefficients ($\bar{a}_{ij}$ and a_{ij}) also show the damper nonlinearity without *a priori* knowledge of the dampers. For Damper A, the cubic damping coefficient ($\bar{a}_{03} = 4.21$) is ignorable, compared to the linear damping ($\bar{a}_{01} = 25.82$). This result indicates that the damping characteristic of Damper A is closed to linear rather than "softening". On the other hand, the significance of the cubic damping coefficient ($\bar{a}_{03} = 148.20$) with respect to the linear damping coefficient ($\bar{a}_{01} = 203.10$) becomes larger for Damper B. However, since the $\bar{a}_{03}$ is still smaller than the $\bar{a}_{01}$, the force of Damper B is "softening". The identified RFM coefficients for Dampers A and B are summarized in Table 4.2.

Identification results of time-varying system

In order to identify a *time-varying* nonlinear system of Damper C, the time histories of the damper data (i.e., x, $\dot{x}$ and f) were partitioned into eight windows as illustrated in Figure 4.4.

Table 4.2: Summary of the identified coefficients using the Restoring Force Method.

Coefficients	Damper A	Damper B	Damper C				
			mean	stdv	max	min	entire
$\hat{\bar{C}}_{10}$	1.24E-2	40.27	37.59	21.01	55.79	-1.48	51.27
$\hat{\bar{C}}_{01}$	27.99	257.00	516.48	64.64	625.80	436.66	526.6
$\hat{\bar{C}}_{30}$	0.63	2.80	3.75	2.06	7.04	0.98	10.90
$\hat{\bar{C}}_{03}$	0.30	-13.17	-26.70	3.47	-21.67	-30.63	-52.09
$\hat{\bar{a}}_{10}$	-1.41	66.32	31.02	56.63	100.30	-59.67	72.60
$\hat{\bar{a}}_{01}$	25.82	203.10	430.40	41.33	490.90	373.30	507.9
$\hat{\bar{a}}_{30}$	-0.55	10.33	101.20	48.11	155.90	38.70	17.38
$\hat{\bar{a}}_{03}$	4.21	148.20	244.66	115.71	387.80	89.29	117.0
$\hat{a}_{10}$	-0.19	1.33	1.33	2.37	4.18	-2.47	3.02
$\hat{a}_{01}$	0.27	3.12	13.17	1.24	14.92	11.38	15.37
$\hat{a}_{30}$	2.11E-5	7.38E-5	7.08E-3	3.38E-3	1.08E-2	2.90E-3	1.37E-3
$\hat{a}_{03}$	3.68E-6	5.34E-4	6.94E-3	3.37E-3	1.08E-2	2.35E-3	3.04E-3
NMSE (%)	0.82	5.03	0.50	0.09	0.66	0.39	1.92

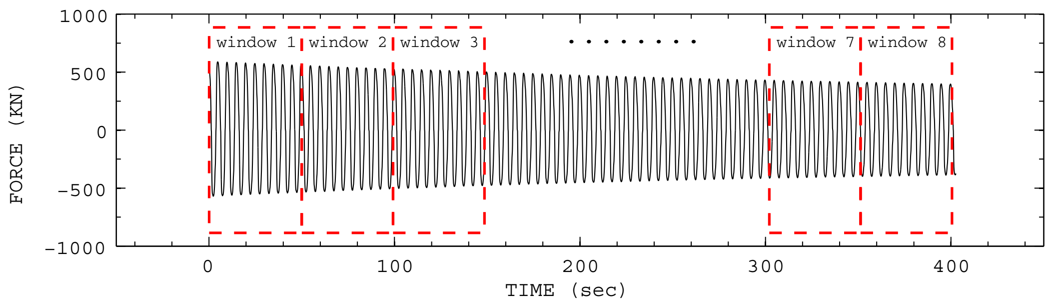

Figure 4.4: Partitioning the time history of the measured force of Damper C for the Restoring Force Method identification.

The time history partition was designed to have ten cycles per window. Then, the RFM identification was performed for each time-history window. Damper C was accurately identified, and the mean and standard deviation of the NMSE for the eight windows were 0.50% and 0.09%, respectively. The identified normalized Chebyshev coefficients and normalized power-series coefficients for the eight windows are illustrated in Figure 4.5. For the normalized Chebyshev coefficients ($\bar{C}_{ij}$), the linear damping ($\bar{C}_{01}$) is dominant with the mean value of 516.48, while the

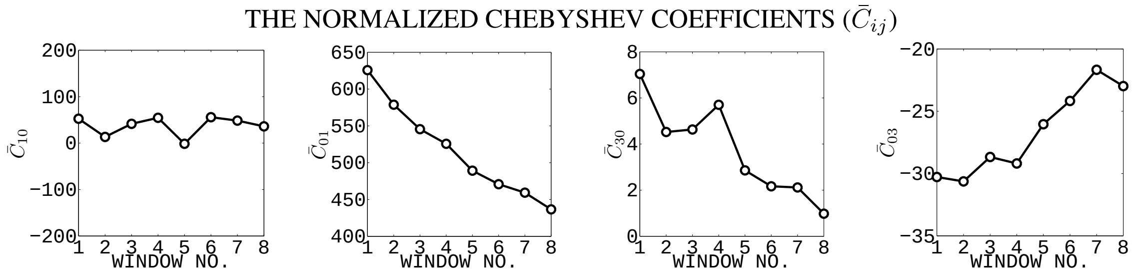

(a) 1st stiffness (b) 1st damping (c) 3rd stiffness (d) 3rd damping

(e) 1st stiffness (f) 1st damping (g) 3rd stiffness (h) 3rd damping

Figure 4.5: The identified coefficients of Damper C for different time-history windows.

cubic stiffness ($\bar{C}_{30}$) is negligible with the mean value of 3.75. The linear damping coefficient ($\bar{C}_{01}$) decreases as the measured force decreases (Figure 4.5 (b)), while the linear stiffness ($\bar{C}_{10}$) remains constant (Figure 4.5 (a)). The cubic damping coefficient ($\bar{C}_{03}$) decreases as the damper reciprocates. For the normalized power-series coefficients ($\bar{a}_{ij}$), the first order damping ($\bar{a}_{01}$) and third order damping ($\bar{a}_{03}$) decrease (Figures 4.5 (f) and (h)), while the first order stiffness ($\bar{a}_{10}$) and third order stiffness remain constant (Figures 4.5 (e) and (g)). These results indicate that the degrading force of Damper C is due to the change of damping characteristics rather than stiffness characteristics over time.

The identified RFM coefficients for Damper C are summarized in Table 4.2. In the table, the mean, standard deviation, maximum and minimum values of the RFM coefficients identified for the eight identification windows in Figure 4.4 are shown. For a comparison purpose, Damper

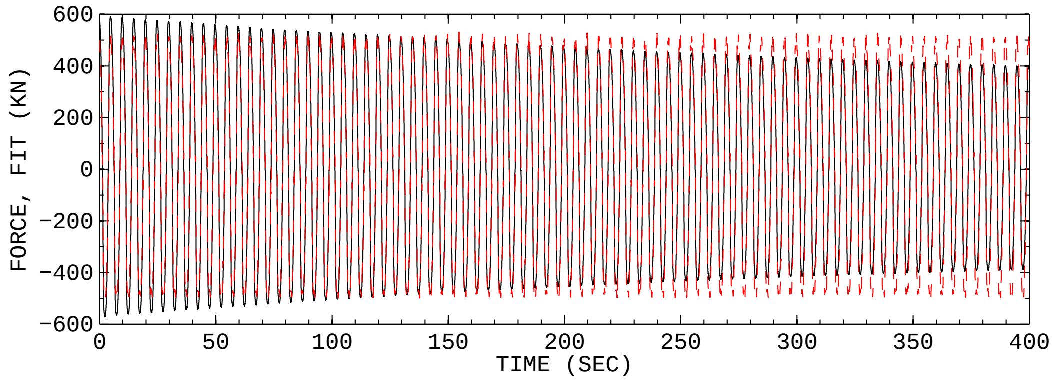

Figure 4.6: The measured and identified forces for the time-varying system of Damper C under the stationary sinusoidal excitation with a constant frequency of 0.2 Hz and constant peak displacements of ± 25.4 mm using the entire domain of measured time histories of displacement, velocity and force. In the figure, the measured force is in the solid line, and the identified force is in the dashed line.

C was also identified using the entire domain of measured time histories, and the corresponding identified RFM coefficients for the entire time domain are also shown in the last column of Table 4.2. The table shows that the dominant coefficients for the entire time-history data are within the range of the minimum and maximum for the partitioned time-history data (e.g., $-1.48 \leq 51.27 \leq 55.79$ for the $\bar{C}_{10}$ and $436.66 \leq 526.60 \leq 625.80$). The NMSE of the former is also about 3.5 times greater than the latter. The measured and identified forces using the entire time domain are compared in Figure 4.6. The figure illustrates that the identified force estimates the average of the degrading measured force over time.

Findings from the identification results

Based on above results, several important conclusions can be drawn. First, two different types of nonlinear dampers were accurately identified without using *a priori* knowledge about the identified dampers. This is because the identification procedures of the RFM are data-driven and model-independent. Although no *a priori* knowledge was used in the identification, the identified Chebyshev and power series coefficients still contain the information concerning the dominant physical characteristics of the identified dampers. Consequently, in the development of the change detection methodology, these coefficients can be used as "change indicators" (or "features" in pattern recognition sense). Moreover, knowing which coefficients the changes were observed in, one can interpret the physical meanings of the detected changes. Hence, guidelines to deal with the detected changes can be established for field applications. An excellent example can be found in the identification results of Damper C. Again, without *a priori* knowledge of the time-varying damper, the identified coefficients show that the decreasing measured force is due to degradation of the damping efficiency (decreasing damping coefficients) in time rather than the changes of damper stiffness (constant stiffness coefficients).

Notice that although the identified normalized Chebyshev coefficients ($\bar{C}_{ij}$) are related to the dampers' stiffness or damping characteristics, they are not exactly equivalent to the actual spring or damping constants of the dampers. For physical interpretation purposes, the normalized power series coefficients ($\bar{a}_{ij}$) and de-normalized power series coefficients (a_{ij}) can be used as more convenient indices. However, the $\bar{C}_{ij}$ have many advantages over $\bar{a}_{ij}$ and a_{ij}, because of the orthogonal property of the Chebyshev polynomials. The orthogonal property of $\bar{C}_{ij}$ can reduce the complexity of the uncertainty quantification of change detection with noisy measurements. Detailed discussion of this issue is provided in Section 4.4.3.

4.4 Uncertainty Estimation of Damper Identification

4.4.1 Data Generation of Noisy Response

In order to study the effects of measurement noise on the damper identification, the sensor measurements of Dampers A, B and C were polluted with 5% additive zero-mean Gaussian noise

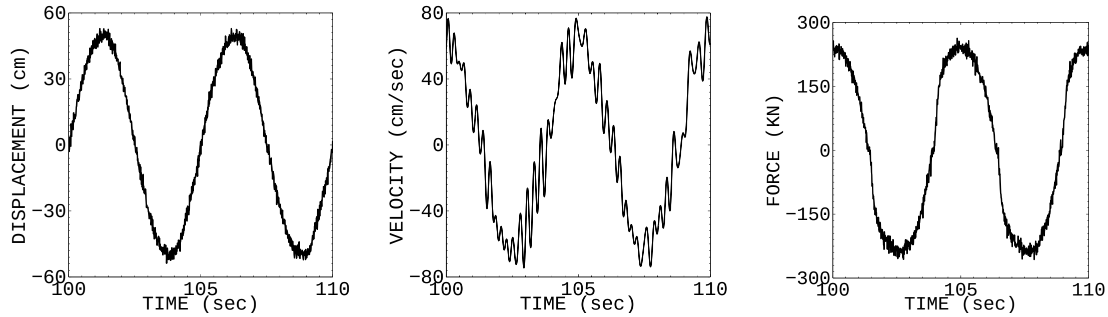

Figure 4.7: Sample time histories of noisy response of Damper B. The displacement and force were polluted with 5% additive zero-mean Gaussian noise with respect to the measured response states, and then the velocity was obtained with numerical differentiation following the data processing procedures discussed in Section 4.2.2.

with respect to the root-mean-square (RMS) of the measurement states: the acceleration ($\ddot{x}$) and force (f) for Damper A, and the displacement (x) and force (f) for Dampers B and C. Once the measurement states were polluted, the necessary damper response for the RFM identification was obtained numerically with the noisy measurements: x and $\dot{x}$ for Damper A, and $\dot{x}$ for Dampers B and C. Hence, the uncertainty of the noisy measurements propagated throughout the numerically obtained response. The detailed data processing procedures were the same as those described in Section 4.2.2. A total of 3000 noisy data sets were generated for all tested dampers. Sample time histories of noisy data sets for Damper B are shown in Figure 4.7.

4.4.2 Damper Identification with Noisy Response

Once the 3000 noisy data sets were obtained for each damper, the RFM identification was performed, and the corresponding Chebyshev coefficients ($\bar{C}_{ij}$) and power series coefficients ($\bar{a}_{ij}$ and a_{ij}) were identified. The NMSE of the RFM identification was relatively low for all tested dampers: the mean and standard deviation of the NMSE for Damper A were 1.33% and 0.79%, respectively; those for Damper B were 3.91% and 2.54%, respectively; and those for Damper C were 4.59% and 2.98%, respectively.

For the linear damping ($\bar{C}_{01}$), which was the dominant term in the identification, the mean of $\bar{C}_{01}$ for Damper A was 16.84, which was 61.16% compared to the identified $\bar{C}_{01}$ of 27.99 using the "clean" data set, while the means of $\bar{C}_{01}$ for Dampers B and C were 278.06 and 562.48, respectively, which were 108.19% and 108.91%, compared to the identified $\bar{C}_{01}$ of 257.00 and 516.48, respectively, using the "clean" data set. Hence, the discrepancy between the identified $\bar{C}_{01}$ for "clean" and "noisy" data was larger with Damper A than with Dampers B and C.

The statistics of identified coefficients for Dampers A, B and C using the RFM are summarized in Table 4.3. The table shows that the coefficients of variance (cv) of $\bar{C}_{01}$ and the cubic damping ($\bar{C}_{03}$) for Dampers B and C are almost identical: the cv of $\bar{C}_{01}$ for Dampers B and C were 0.03 and 0.03, respectively, and the cv of $\bar{C}_{03}$ were -0.15 and -0.18, respectively. This result is expected since the "softening" characteristics of Dampers B and C are similar with the same designed damping exponent ($n = 0.3$). On the other hand, Damper A has a different cv (cv of $\bar{C}_{03} = -5.00$) because the designed damping exponent for Damper A was $n = 1.0$. Hence, physical interpretation using the identified coefficient was still valid even with the noisy measurements.

4.4.3 Statistical Change Detection of Time-Varying Damper

Statistical independence of the RFM coefficients

In Section 4.3.2, it was shown that the identified RFM coefficients can be used as excellent "change indicators". A question is left: among three kinds of RFM coefficients, which one

Table 4.3: Statistics of the identified RFM coefficients for the multiple tests and 3000 noisy data sets. The mean, standard deviation and coefficient of variation are shown. In this table, only significant coefficients are shown, including the linear stiffness ($\bar{C}_{10}$, $\bar{a}_{10}$, a_{10}), linear damping ($\bar{C}_{01}$, $\bar{a}_{01}$, a_{01}), cubic stiffness ($\bar{C}_{30}$, $\bar{a}_{30}$, a_{30}), and cubic damping ($\bar{C}_{03}$, $\bar{a}_{03}$, a_{03}). The * indicates the coefficients of Damper C are the averaged values for eight time-history windows shown in Figure 4.4.

(a) Normalized Chebyshev Coefficients ($\hat{\bar{C}}_{ij}$)

Coefficients	Damper A			Damper B			Damper C*		
	mean	stdv	cv	mean	stdv	cv	mean	stdv	cv
$\hat{\bar{C}}_{10}$	0.67	0.19	0.28	26.23	14.26	0.54	55.19	32.17	0.58
$\hat{\bar{C}}_{01}$	16.84	0.16	0.01	278.06	8.60	0.03	562.48	17.17	0.03
$\hat{\bar{C}}_{30}$	0.14	0.14	1.00	-6.05	14.09	-2.33	-6.17	28.40	-4.60
$\hat{\bar{C}}_{03}$	-0.02	0.10	-5.00	-62.46	9.14	-0.15	-112.19	20.71	-0.18

(b) Normalized Power Series Coefficients ($\hat{\bar{a}}_{ij}$)

Coefficients	Damper A			Damper B			Damper C*		
	mean	stdv	cv	mean	stdv	cv	mean	stdv	cv
$\hat{\bar{a}}_{10}$	1.55	0.69	0.45	110.49	115.28	1.04	286.46	245.46	0.86
$\hat{\bar{a}}_{01}$	18.23	0.74	0.04	642.43	86.03	0.13	1093.50	198.68	0.18
$\hat{\bar{a}}_{30}$	-1.20	2.32	-1.93	-190.07	360.35	-1.90	-473.24	786.05	-1.66
$\hat{\bar{a}}_{03}$	-2.63	2.26	-0.86	-747.97	322.88	-0.43	-982.85	669.23	-0.68

(c) De-normalized Power Series Coefficients ($\hat{a}_{ij}$)

Coefficients	Damper A			Damper B			Damper C*		
	mean	stdv	cv	mean	stdv	cv	mean	stdv	cv
$\hat{a}_{10}$	1.42E-1	6.27E-2	0.44	2.00	2.09	1.05	10.98	7.85	0.71
$\hat{a}_{01}$	1.17E-1	5.56E-3	0.05	7.25	0.90	0.12	26.25	3.63	0.14
$\hat{a}_{30}$	-6.04E-4	2.36E-3	-3.91	-1.10E-3	2.12E-3	-1.93	-2.56E-2	4.24E-2	-1.66
$\hat{a}_{03}$	-8.17E-7	6.69E-7	-0.82	-1.05E-3	4.35E-4	-0.41	-1.31E-2	8.32E-3	-0.64

(d) Normalized Root-Mean-Square of Identification Errors

Coefficients	Damper A			Damper B			Damper C*		
	mean	stdv	cv	mean	stdv	cv	mean	stdv	cv
NMSE	1.33E-2	7.90E-3	0.59	3.91E-2	2.54E-2	0.65	4.59E-2	2.98E-2	0.65

is most useful for change detection in a *probabilistic* sense. The advantage of using the de-normalized power series coefficients (a_{ij}) is that direct physical interpretation is possible because the a_{ij} preserves the physical units (e.g., the unit of a_{10} for Damper B is kN/mm, that is the same as the linear spring constant). The advantage of using the normalized power series coefficients ($\bar{a}_{ij}$) is that although the direct physical interpretation is not convenient due to using the normalized displacement ($\bar{x}$) and velocity ($\bar{\dot{x}}$), $\bar{a}_{ij}$ measures the relative contribution of each power series term to the identified restoring force. However, when measurement uncertainty exists, the identified a_{ij} and $\bar{a}_{ij}$ are not statistically independent because the basis functions of the power series expansion (i.e., $x^i \dot{x}^j$ and $\bar{x}^i \bar{\dot{x}}^j$) are not orthogonal. Consequently, for the uncertainty quantification of the system changes, the testing dimension of the statistical Hypothesis Test (HT) becomes too high because the a_{ij} and $\bar{a}_{ij}$ are multivariate coefficients. For example, in this study, there are 36 identified coefficients with the highest series order of five for the displacement and velocity. For a_{ij} and $\bar{a}_{ij}$, because each of the coefficients are not statistically independent, the HT should be performed with the testing dimension of 36 (maximum). In Figure 4.8 (a), the scatter plot between the first order damping ($\bar{a}_{01}$) and linear stiffness ($\bar{a}_{10}$) shows no significant statistical correlation. However, a strong correlation is observed between the linear damping ($\bar{a}_{01}$) and cubic damping ($\bar{a}_{03}$).

On the other hand, the normalized Chebyshev coefficients ($\bar{C}_{ij}$) preserves the *statistical independence* because the basis function of Chebyshev polynomials are *orthonormal* (Mason and Handscomb, 2003). In Figure 4.8 (b), both scatter plots illustrate that no significant statistical correlations are observed between the identified Chebyshev coefficients. With the statistical independence property, the testing dimension of the HT dramatically reduces to *one*. That

<table>
<tr><th>Coefficient type</th><th colspan="2">Scatter plots</th></tr>
<tr><td>(a) Normalized power series Coefficients ($\bar{a}_{ij}$)</td><td>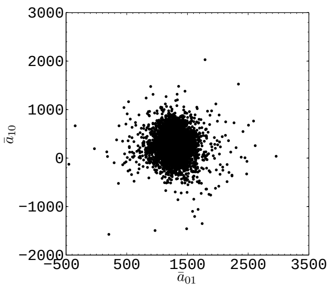

($\rho = -0.04$)</td><td>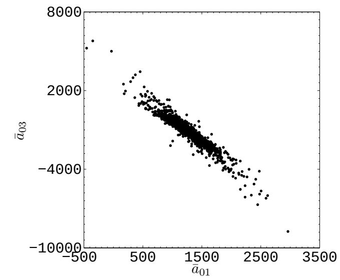

($\rho = -0.96$)</td></tr>
<tr><td>(b) Normalized Chebyshev Coefficients ($\bar{C}_{ij}$)</td><td>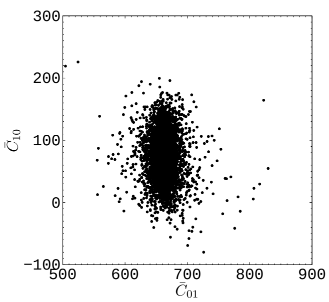

($\rho = -0.08$)</td><td>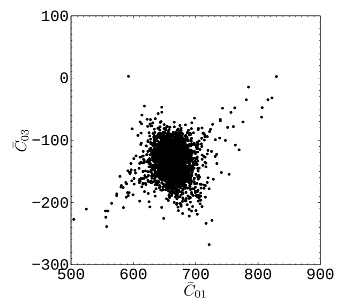

($\rho = 0.05$)</td></tr>
</table>

Figure 4.8: Sample scatter plots of the normalized Chebyshev coefficients and normalized power series coefficients for the noisy response of Damper C (Window 1 in Figure 4.4). The magnitude of the linear correlation coefficient (ρ) between two identified coefficients is also shown in the table.

is, the HT can be performed for each individual Chebyshev coefficient to detect possible system changes. Hence, the normalized Chebyshev coefficients were used in the statistical change detection in this study.

Statistical change detection using identified coefficients

Using the 3000 sets of the identified, normalized Chebyshev coefficients ($\bar{C}_{ij}$), the distributions of the identified $\bar{C}_{ij}$ were obtained. The histograms of the identified first order damping coefficient ($\bar{C}_{01}$), the dominant coefficient in the Damper C identification, for different time-history windows are shown in Figure 4.9. The bin width of the histograms was determined using the normal reference rule (or Scott's rule) (Scott, 1979, 1992), optimized for the Gaussian distribution as

$$h = 3.5 \; S_X \; N^{-1/3} \tag{4.6}$$

where h is the bin width (or smoothing factor), S_x is the sample standard deviation of a statistic of interest X, and N is the sample size. The probability density functions (pdf) of $\bar{C}_{01}$ were estimated with the Gaussian distribution assumption and are shown in Figure 4.9. In the figure, the mean of the distributions decrease in time, while the standard deviations of the distributions remain approximately constant. The pseudo-constant deviation is the justification as to why the noise amplitudes were fixed at 5% RMS with respect to the measurement states among the windows (Section 4.4.1). After obtaining the distributions of identified coefficients, one can achieve the three objectives of this study that were discussed in Section 4.1.2. First, with the mean of the distribution, one can accurately check if the damper has had a genuine system change. Second, one can interpret the physical meaning of the detected changes. In Sections 4.3.2 and 4.4.2, it was shown that the actual changes in Damper C are due to the degradation of the damping efficiency rather than stiffness efficiency. Third, with the standard deviations of the distributions determined, one can quantify the uncertainty of the detected changes. Using the RFM identification procedure, these objectives can be achieved without knowing the underlying physical characteristics of the identified system.

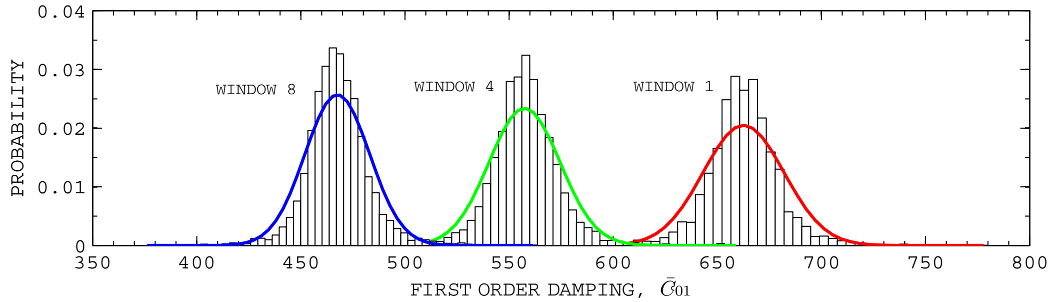

Figure 4.9: Histograms and probability density functions (pdf) of the first order damping normalized Chebyshev coefficient ($\bar{C}_{ij}$) for different time-history windows. The bin width (or smoothing factor) of the histogram was determined using the normal reference rule (or Scott's rule). The pdf's were estimated with the assumption of the normal distribution.

Using the extracted coefficient distributions, the statistical HT was performed to detect the changes in the distribution means. This test can be performed with the test statistics of two-tailed T-distribution (Hogg and Tanis, 1997; Mendenhall and Sincich, 1995):

$$H_0 : (\mu_1 - \mu_2) = 0, \qquad z = \frac{\bar{y}_1 - \bar{y}_2}{\sigma_{(\bar{y}_1 - \bar{y}_2)}} \approx \frac{\bar{y}_1 - \bar{y}_2}{\sqrt{\frac{s_1^2}{n_1} + \frac{s_2^2}{n_2}}} \tag{4.7}$$

where H_0 is the null-hypothesis, $\bar{y}_1$ and $\bar{y}_2$ are the identified Chebyshev coefficients for two different identification windows, μ_1 and μ_2 are the means of the coefficient distributions from two identification windows, σ_1 and σ_2 are the standard deviations of the coefficient distributions from two identification windows, and s_1 and s_2 the sample standard deviations of the coefficient distributions from two identification windows. In the HT's, the change of the distribution mean was observed with all windows (Windows 1 to 8) with a 95% confidence level.

4.5 Bootstrap Estimation of the Identification Uncertainty

The uncertainty quantification usually requires many data sets — in Section 4.4, 3000 data sets were used to measure the identification uncertainty. However, collecting sufficient data sets of large-scale viscous dampers for reliable statistical estimation is very difficult and expensive. Statistical data recycling techniques have been applied successfully in many fields of engineering and science for the error generalization of identification results using insufficient data sets. In this section, the Bootstrap method is used to measure the uncertainty of the damper change detection with a single data set. The Bootstrap estimates of the identification uncertainty with a single data set will be compared with the uncertainty estimates with the multiple data sets discussed in Section 4.4.

4.5.1 Overview of the Bootstrap Method

The Bootstrap method is a statistical data recycling technique for the uncertainty estimation of any kind of identification parameters. This method is commonly used where the estimation of parameter uncertainty is needed, but an insufficient amount of data is available for a statistically reliable uncertainty quantification. Excellent introductory literature on the Bootstrap method can be found in the work of Efron (1979); Efron and Tibshirani (1993), Davison and Hinkley (1997), and Martinez and Martinez (2002).

The Bootstrap method starts with a very simple assumption. An arbitrary parameter (θ) identified using an independently and identically distributed (*i.i.d*) random data set, $\mathbf{y} = (y_1, y_2, \cdots, y_n)^T$ with the underlying true distribution (F) can be modeled as

$$\theta = t(F) \tag{4.8}$$

where $t(\bullet)$ is a nonlinear function of F. Without knowing F, the uncertainty of θ is commonly determined with multiple data sets, $\{\mathbf{y}_1, \mathbf{y}_2, \cdots, \mathbf{y}_M\}$, drawn from the same distribution F as

$$s_\theta = \sqrt{\frac{1}{M-1}\sum_{i=1}^{M}(\theta_i - m_\theta)^2} \tag{4.9}$$

where s_θ is the sample standard deviation of θ, m_θ is the sample mean of θ, M is the number of multiple tests, and θ_i is the parameter identified in the i^{th} test.

Instead of performing multiple tests for the uncertainty quantification, the Bootstrap method recycles a single data set, $\mathbf{y}$ with the empirical distribution ($\hat{F}$). The data recycling is performed with the random selection of a sample (y_k, where $1 \leq k \leq n$) from $\mathbf{y}$ for n times *with replacement*. With replacement, the probability of each sample to be selected is $1/n$. Performing these procedures B times, one can obtain multiple Bootstrap replicates, $\{\mathbf{y}_1^*, \mathbf{y}_2^*, \cdots, \mathbf{y}_B^*\}$. The Bootstrap estimate of the parameter uncertainty is determined as

$$s_\theta^* = \sqrt{\frac{1}{B-1}\sum_{i=1}^{B}(\theta_i^* - m_\theta^*)^2} \tag{4.10}$$

where s^*_θ is the Bootstrap standard error of θ, θ^*_i is the parameter identified in the i^{th} Bootstrap replicate of the data set, B is the number of the Bootstrap replicates, and m^*_θ is the Bootstrap estimate of θ defined as

$$m^*_\theta = \frac{1}{B}\sum_{i=1}^{B}\theta^*_i \tag{4.11}$$

In order that $s_\theta \approx s^*_\theta$, the empirical distribution $\hat{F}$ should be close to the true distribution F. Therefore, the following two conditions should be satisfied for the Bootstrap estimation of the standard error:

1. The random data **y** is $i.i.d.$
2. The empirical distribution $\hat{F}$ is close to the true distribution F.

In the context of the damper identification problem under discussion, however, since the noisy measurement states $(\ddot{x}, f)$ for Damper A and (x, f) for Dampers B and C are time-correlated (i.e., the data are not $i.i.d$), the standard Bootstrap method described above needs to be modified to deal with the time-dependency. Many modified algorithms have been developed and introduced: model-based resampling (Efron and Tibshirani, 1986; Kreiss and Franke, 1992), block resampling (Carlstein, 1986; Hall, 1985; Shi, 1991), phase scrambling (Theiler et al., 1992; Timmer, 1998), and periodogram resampling (Davison and Hinkley, 1997). Detailed descriptions of each of these methods can be found in Davison and Hinkley (1997), and Härdle et al. (2003). Among these methods, one of the most widely used method is the model-based resampling, because of its simple procedure and good theoretical behavior when the time-series model is correct. Consequently, in this study, the model-based resampling method was employed for the uncertainty estimation of the time-dependent data. In Section 4.5.2, a detailed Bootstrap resampling procedure is proposed and described in detail for the cases that the displacement and force were measured (Damper A), and that the acceleration and force were measured (Dampers B and C).

4.5.2 Bootstrap Resampling of Noisy Response Data

Single data sets of Dampers A, B and C were recycled with the Bootstrap method using the following procedures:

Approach when displacement is measured

A single data set of noisy (5% RMS) displacement (x) and force (f) for Dampers B and C was resampled with the Bootstrap method as follows:

1. The same data processing procedures for Dampers B and C in Section 4.2.2 were performed to obtain the triplet $(x, \dot{x}, f)$.

2. The RFM identification was performed with the noisy $(x, \dot{x}, f)$. The identification residual (e) was obtained as $e = f - \hat{f}$, where $\hat{f}$ is the identified force using the RFM.

3. The auto-regression (AR) was performed for the time histories of x and e. The corresponding AR estimate of x is $\hat{x}$. The AR orders were determined so as to satisfy the conditions that ε_x and ε_e become *i.i.d*, where ε_x is the AR residual of x, and ε_e is the AR residual of e. The detailed procedure for determining the optimal AR orders for the ε_x and ε_e is described later in this section.

4. The Bootstrap resampling was performed with the ε_x and ε_e to obtain the Bootstrap replicates of the ε_x and ε_e (ε_x^* and ε_e^*, respectively).

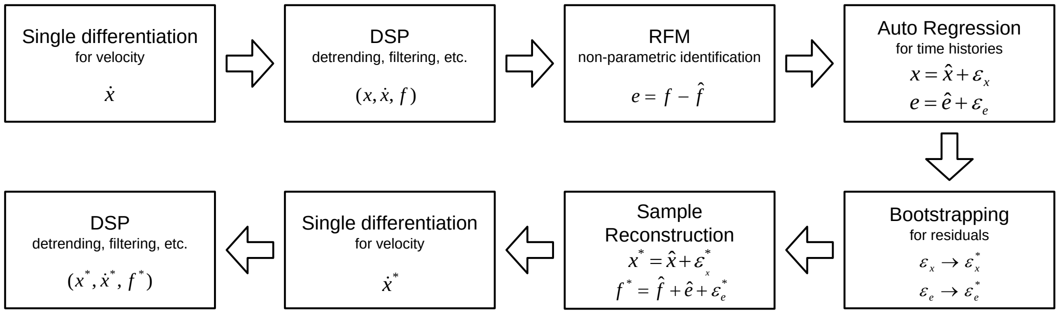

Figure 4.10: Bootstrap resampling procedures for Dampers B and C with measured displacement (x) and force (r).

5. The Bootstrap replicates of the displacement (x^*) and force (f^*) were obtained with the sample reconstruction as $x^* = \hat{x} + \varepsilon_x^*$ and $f^* = \hat{f} + \hat{e} + \varepsilon_e^*$.

6. The Bootstrap version of the velocity $(\dot{x}^*)$ was obtained through the differentiation of x^*. In this procedure, the same filter and time-history window as those discussed in Section 4.2.2 were applied.

A total of 3000 Bootstrap replicates $(x^*, \dot{x}^*, f^*)$ were obtained. The Bootstrap resampling procedures for Dampers B and C are also illustrated schematically in Figure 4.10.

A sample comparison of the original and Bootstrap-resampled data is shown in Figures 4.13. The Bootstrap resampled data show slightly larger dispersion than the original data in the phase plots. The RFM identification was performed with the 3000 Bootstrap replicates, and the corresponding RFM coefficients were identified. The Bootstrap standard errors of 3000 identified coefficient sets were estimated using Equation 4.10, and compared to the standard deviations of multiple tests. Table 4.4 shows a comparison of the error estimations of the RFM identified coefficients with multiple tests. In the table, the error estimates with the Bootstrap method are larger than those with multiple tests: 7% $\sim$ 42% for Damper B and -0.2% $\sim$ 53% for Damper

Table 4.4: Bootstrap estimations of standard errors for the coefficients identified using the Restoring Force Method. The Bootstrap estimates are compared with the standard deviations through the multiple tests shown in Table 4.3. The sample size is 3000 for both the Bootstrap and multiple test estimates.

Coefficients	Damper A			Damper B			Damper C		
	Multiple	Bootstrap	Ratio	Multiple	Bootstrap	Ratio	Multiple	Bootstrap	Ratio
$\bar{C}_{10}$	0.19	0.32	1.68	14.26	17.35	1.22	32.17	42.14	1.31
$\bar{C}_{01}$	0.16	0.31	1.94	8.60	12.22	1.42	17.17	26.21	1.53
$\bar{C}_{30}$	0.14	0.32	2.29	14.09	18.63	1.32	28.40	37.81	1.33
$\bar{C}_{03}$	0.10	0.20	2.00	9.14	12.49	1.37	20.71	27.47	1.33
$\bar{a}_{10}$	0.69	1.44	2.09	115.28	149.10	1.29	245.46	311.77	1.27
$\bar{a}_{01}$	0.74	1.64	2.22	86.03	104.55	1.22	198.68	235.09	1.18
$\bar{a}_{30}$	2.32	4.76	2.05	360.35	474.97	1.32	786.05	983.70	1.25
$\bar{a}_{03}$	2.26	5.67	2.48	322.88	395.84	1.23	669.23	823.17	1.23
a_{10}	6.27E-2	7.13E-2	1.14	2.09	2.67	1.28	7.85	11.60	1.48
a_{01}	5.56E-3	1.01E-2	1.82	0.90	1.06	1.18	3.63	4.58	1.26
a_{30}	2.36E-3	7.03E-4	0.30	2.12E-3	2.71E-3	1.28	4.24E-2	5.14E-2	1.21
a_{03}	6.69E-7	1.30E-6	1.94	4.35E-4	4.66E-4	1.07	8.32E-3	8.13E-3	0.98
NMSE (%)	7.90E-3	2.05E-2	2.59	2.54E-2	3.02E-2	1.19	2.98E-2	2.98E-2	1.00

C. Hence, it can be seen that the Bootstrap estimation of the identification error is more conservative than the results obtained through estimation with multiple tests. In addition, the results indicate that the Bootstrap method is applicable to the time-varying system (Damper C), as well as the time-invariant system (Damper B).

Approach when acceleration is measured

Using a single data set of noisy (5% RMS) measurements of the acceleration ($\ddot{x}$) and force (f) for Damper A, the Bootstrap method was applied as follows:

1. The same data processing procedures for Damper A in Section 4.2.2 were performed to obtain the triplet $(x, \dot{x}, f)$.

2. The RFM identification was performed with the noisy $(x, \dot{x}, f)$. The identification residual (e) was obtained as $e = f - \hat{f}$, where $\hat{f}$ is the identified force using the RFM.

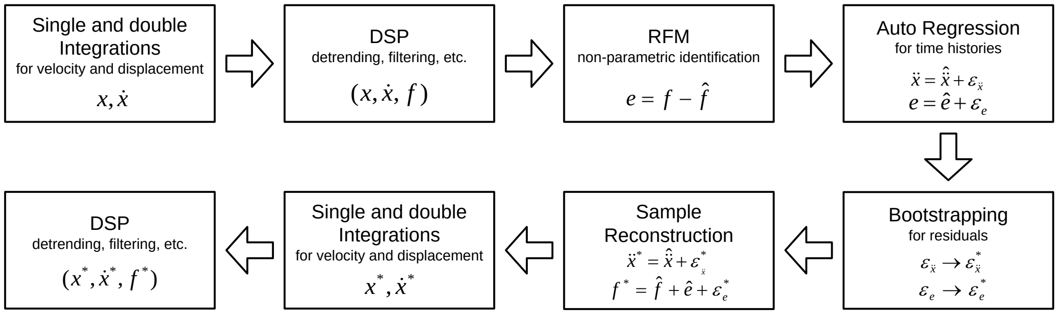

Figure 4.11: Bootstrap resampling procedures for Damper A with measured acceleration ($\ddot{x}$) and force (r).

3. The AR was performed for the time-histories of $\ddot{x}$ and e. The AR estimate of $\ddot{x}$ is $\hat{\ddot{x}}$. The AR orders of $\hat{\ddot{x}}$ and $\hat{e}$ were determined so as to satisfy the conditions that $\varepsilon_{\ddot{x}}$ and ε_r become *i.i.d*, where $\varepsilon_{\ddot{x}}$ is the AR residual of $\ddot{x}$, and ε_e is the AR residual of e. The detailed procedure for determining the optimal AR orders is described below.

4. The Bootstrap resampling was performed with $\varepsilon_{\ddot{x}}$ and ε_e to obtain the Bootstrap replicates of $\varepsilon_{\ddot{x}}$ and ε_e ($\varepsilon_{\ddot{x}}^*$ and ε_e^*, respectively).

5. The Bootstrap replicates of the acceleration ($\ddot{x}^*$) and force (f^*) were obtained with the sample reconstruction as $\ddot{x}^* = \hat{\ddot{x}} + \varepsilon_{\ddot{x}}^*$ and $f^* = \hat{f} + \hat{e} + \varepsilon_e^*$.

6. The $\ddot{x}^*$ was integrated and then double-integrated for the Bootstrap version of the velocity ($\dot{x}^*$) and displacement (x^*), respectively. The same filter and time-history window were applied to $\dot{x}^*$ and x^* as described in Section 4.2.2.

A total of 3000 Bootstrap replicates $(x^*, \dot{x}^*, f^*)$ were generated. The Bootstrap resampling procedures for Damper A are also illustrated in Figure 4.11.

A sample comparison between the original and Bootstrap-resampled data for Damper A is shown in Figure 4.13 (a). Unlike Dampers B and C, the range of the Bootstrap-resampled displacement is approximately twice larger than that of the original displacement in the displacement-force plot, while the velocity-force plots of two data sets are almost identical.

Issues involving the auto-regression procedure

The above results indicate that using the measured acceleration, the Bootstrapping for the velocity through single-integration was successful, but the Bootstrapping for the displacement through double-integration failed. In the model-based Bootstrap method, the resampling results are largely dependent on the performance of the AR identification. The AR is performed to remove the trends of the time-series data, and with successful AR, the corresponding AR residuals ($\varepsilon_{\ddot{x}}$ and ε_e for Damper A, and ε_x and ε_e for Dampers B and C) become $i.i.d.$ Figure 4.12 shows the significance of the time-correlation for different AR orders. The significance of the time-correlation is commonly measured with the correlation coefficient (ρ) in a lag plot. Here, the *lag* is defined as a fixed time distance. For example, for the vector $\varepsilon_e = \{\varepsilon_{e_1}, \varepsilon_{e_2}, \ldots, \varepsilon_{e_n}\}$ for Damper B, the ε_{e_2} and ε_{e_5} have a lag with order *three*. Hence, in the lag plot (usually with order one), which has the x-axis of ε_{e_i} and the y-axis of $\varepsilon_{e_{i-1}}$ ($i = 2, 3, \ldots, n$), the correlation coefficient $\rho(\varepsilon_{e_i}, \varepsilon_{e_{i-1}})$ measures the serial correlations of the ε_e in time. In Figure 4.12 (a), the $\rho(\varepsilon_{e_i}, \varepsilon_{e_{i-1}})$ asymptotically approaches to zero as the AR order increases. However, Figure 4.12 (b) illustrates that the $\rho(\varepsilon_{x_i}, \varepsilon_{x_{i-1}})$ approaches to zero as the AR order approaches from 1 to 40. Then, the $\rho(\varepsilon_{x_i}, \varepsilon_{x_{i-1}})$ increases as the AR order increases more than 40. This result indicates that the AR regression for the identification residual (e) becomes overfitted when the AR order is greater than 40. Consequently, the AR order of 40 was used in the Bootstrap resampling for Damper B. The same procedure of determining the optimal AR order was applied for Dampers A and C.

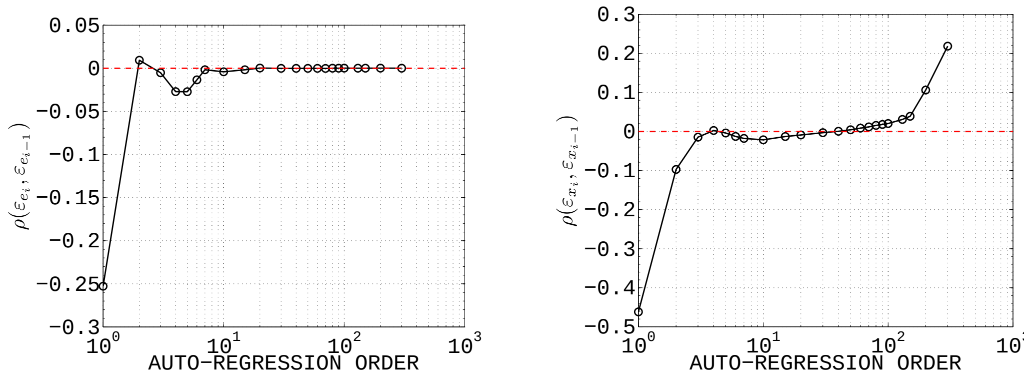

(a) Residual of the Identified force residual (ε_e)

(b) Displacement residual (ε_x)

Figure 4.12: Time-correlations of the auto-regression (AR) residuals of the identified restoring force residual (ε_e) and the displacement (ε_x) for different AR orders. The time-correlations were measured with the correlation coefficients of the order-one lags for ε_e and ε_x. The definition of the order-one lags is explained in the text.

Although the serial correlations in time were carefully removed with the optimal AR orders, however, perfect removal of the time correlations is almost impossible. Consequently, a slight amount of time-correlation will affect the results of differentiation or integration. In this study, the results indicate that the unremoved trend does not significantly affect to the results of the single differentiation ($x^* \rightarrow \dot{x}^*$) and integration ($\ddot{x}^* \rightarrow \dot{x}^*$). However, the unremoved trend significantly influences the results of the second integration ($\dot{x}^* \rightarrow x^*$) as the example of Damper A. Consequently, the Bootstrapping for the displacement becomes unsuccessful. Therefore, in the application of the Bootstrap method to noisy measurements, it is recommended that the force as well as the displacement of the damper be directly measured.

4.6 Summary and Conclusions

An experimental study was conducted to develop a probabilistic change detection methodology for *in-situ* monitoring of nonlinear viscous dampers with measurement uncertainty. It was found that the coefficients identified using the Restoring Force Method can be used as excellent indicators (or features) (1) to detect the changes of nonlinear systems, (2) to interpret the physical meaning of the detected changes, and (3) to quantify the uncertainty of the detected system changes.

The Bootstrap method was also investigated for uncertainty quantification of the detected changes when the measurement data are insufficient for reliable statistical inference. Using the Bootstrap method, the uncertainty of the identification was estimated reasonably accurately even with a single data set when the displacement and force were measured.

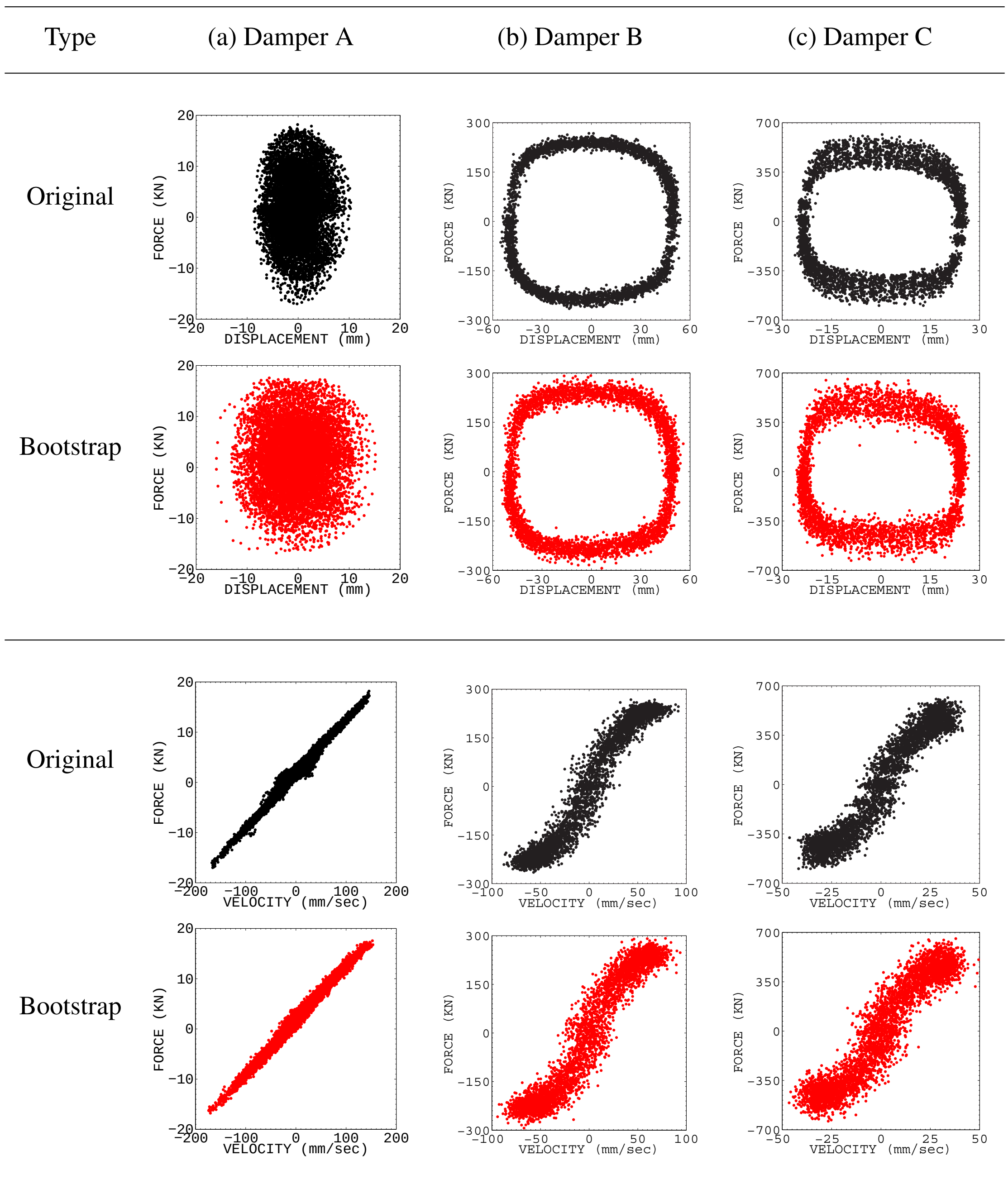

Figure 4.13: A comparison of the original and Bootstrap-resampled data for different nonlinear dampers. The upper half of the figure shows displacement-force plots, while the lower half shows the velocity-force plots.

Chapter 5

Model-Order Reduction Effects on Change Detection in Uncertain Nonlinear Magneto-Rheological Dampers

5.1 Introduction

5.1.1 Motivation

The development of an effective structural health monitoring (SHM) methodology is imperative for two major purposes: (1) to avoid catastrophic structural failure by detecting various types of structural deterioration, modification or changes during the operation, and (2) to reduce maintenance cost by establishing effective means and time schedules for structural maintenance or rehabilitation for the detected or predicted changes. However, the development of an effective SHM methodology is very challenging, especially when monitored structures are complex nonlinear systems and their system characteristics are uncertain. The *system characteristics uncertainty* can be frequently found due to uncertain system parameters or various environmental effects on system characteristics.

Current SHM approaches, however, have the following limitations for the condition assessment of nonlinear structures with system characteristics uncertainty:

1. The system models are commonly over-simplified. The over-simplification can be conducted in two ways: (1) excessive model-order reduction of complex nonlinear systems and (2) ignorance of significant environmental effects. The excessive model-order reduction makes the identification results inaccurate. Moreover, the effects of model-order reduction to the change detection are rarely studied. Detected structural changes could be also significantly biased with ignoring the changes of environmental effects (Peeters et al., 2001).

2. The modeling approaches are not "flexible" enough to identify timely changing (or deteriorating) structures. Because *parametric* identification approaches require *a priori* knowledge of the monitored structures, if the structures change into another classes of nonlinear systems, the system identification using the "old" models are no longer valid. *Non-parametric* approaches, however, are more "flexible" than the parametric approaches by identifying the time-varying systems with no assumption about the structures' physical characteristics. Yun et al. (2007) experimentally demonstrated that non-parametric modeling approaches are more advantageous in monitoring purposes

3. Although many current methodologies can detect changes of structural characteristics, physical interpretations of detected changes are rarely possible with current *non-parametric* approaches. Some necessary physical interpretations for effective SHM are discussed earlier.

4. Most of current SHM methodologies are based on deterministic models, and uncertainty of detected structural changes is rarely estimated. The estimation of change detection uncertainty should include the effects of the measurement and system parameter uncertainty as discussed earlier.

5.1.2 Objectives

The objectives of this part of study was to develop a reliable change detection methodology for uncertain nonlinear systems. An experimental study was conducted to test the validity of the developed methodology. A complex nonlinear system with system parameter uncertainty was used in this experimental study. The effects of model-order reduction of the nonlinear system on the performance of the change detection methodology were investigated.

5.1.3 Methodology and Scope

Approach of experimental study

For the experimental study of change detection in uncertain nonlinear systems, a single degree-of-freedom (SDOF) magneto-rheological (MR) damper was used. MR dampers are semi-active energy dissipating devices (Dyke et al., 1996; Ehrgott and Masri, 1992, 1994; Spencer et al., 1997, 1998; Yang et al., 2004). The MR dampers typically consist of a piston rod, electromagnet, damper cylinder filled with MR fluid, accumulator, bearing and seal. The magnetic field generated with the electromagnet changes the characteristics of the MR fluid, which consists of small magnetic particles and fluid base. Consequently, the strength of the electromagnet's input current determines the physical characteristics of MR dampers.

In this study, a series of tests was conducted with random MR damper input currents: under deterministic broadband random excitation, the MR damper was characterized with a constant input current, which randomly varies between tests. Hence,the average (effective) characteristics of the MR damper are determined by the mean of the random input currents, and the uncertainty (variability) of the damper characteristics are controlled by the standard deviation of the input currents.

Identification approach

The restoring force of a nonlinear system can be expressed as

$$r(t) = g(x, \dot{x}, \mathbf{p}) \tag{5.1}$$

where $r(t)$ is the restoring force, $g(\bullet)$ is a nonlinear function, x is the displacement, $\dot{x}$ is the velocity, and **p** is the system parameter vector. The nonlinear restoring force can be modeled as

$$r(t) = \hat{r}(t) + e(t), \qquad \hat{r}(t) = h(x, \dot{x}, \mathbf{q}) \tag{5.2}$$

where $\hat{r}$ is the identified restoring force, $e(t)$ is the modeling error, $h(\bullet)$ is a nonlinear function, and **q** is the postulated model parameter vectors. In parametric modeling approaches, **q** usually is postulated with assumptions of physical characteristics of the system so that the characteristics should be known *a priori*. The physical interpretation, using the parametric approaches, is usually straightforward because the identified **q** is directly related to the assumed system characteristics based on the assumptions concerning the phenomenological model. On the other hand, the non-parametric models do not require the assumption of system characteristics, but their identification processes are model-independent and data-driven. Consequently, the non-parametric models remain valid even if the system is transformed into another type of nonlinearity. An example of the non-parametric approach can be found in the artificial neural networks (ANN) (Masri et al., 1993, 2000, 1999). However, the physical interpretation with the non-parametric approaches is not straightforward because there are no direct relationships between the identified **q** and system characteristics, and as can be seen with ANN, the **q** is not uniquely defined even even with "successful" identification (Masri et al., 2000).

In this case, the Restoring Force Method (RFM) would provide an excellent solution, taking both advantages of the parametric and non-parametric approaches: no *a priori* knowledge of the system is required and physical interpretation of some of the identification results with the identified coefficients (Wolfe et al., 2002; Yun et al., 2007). Therefore, in this study, the RFM was extensively investigated for developing an effective SHM methodology.

Effects of model-order reduction

The significance of the modeling error can be determined by the relationship of the system complexity, $O(\mathbf{p})$ and the model complexity, $O(\mathbf{q})$. If the true system parameters, **p** are uncertain, the relationship between $O(\mathbf{p})$ and $O(\mathbf{q})$ can be defined as

1. $O(\mathbf{p}) > O(\mathbf{q})$: the system complexity is greater than the model complexity (underfitting).
2. $O(\mathbf{p}) = O(\mathbf{q})$: the system complexity is equal to the model complexity (perfect fitting).
3. $O(\mathbf{p}) < O(\mathbf{q})$: the model complexity is greater than the system complexity (overfitting).

Some studies of stochastic non-parametric models of uncertain nonlinear systems were reported by Masri et al. (2006). In practice, the system identification is rarely perfect fitting since the **p** are often unknown. When the system identification is either underfitting or overfitting, the identified **q** is generally biased (Mendel, 1995; Seber and Lee, 2003). Consequently, the damage detection with the identified **q** becomes inaccurate. Hence, in this study, the effects of the model-order reduction on the change detection were investigated with the identified coefficients using the RFM.

Scope

This chapter is organized as follows: the experimental studies using the nonlinear MR damper are discussed in Section 5.2; the non-parametric RFM identification for the MR damper is discussed in Section 5.3; and statistical change detection for the MR damper using pattern-recognition-based classification methods is demonstrated in Section 5.4.

5.2 Experimental Study

5.2.1 Test Apparatus

An MR damper was tested in the Structural Dynamics Laboratory at the University of Southern California.

In order to investigate the effects of system parameter uncertainty, performing a numerous series of tests is necessary. For the successful experimental study, controlling the damper temperature is critical because the internal temperature of the MR damper that is converted from the dissipated energy increases significantly during the series of tests. Consequently, an effective water cooling system was developed to minimize the temperature effects on the damper's physical characteristics (Figure 5.1 (a)). The MR damper was mounted on the actuator, controlling the damper displacement with a PID controller (Figure 5.1 (b)). The MR damper was fully instrumented with various sensors, including an LVDT (displacement), LVT (velocity), accelerometer (acceleration), load cell (force), and temperature (damper surface temperature). In order to conduct a number of tests in this study, a data-acquisition (DAQ) software was also developed. The role of the developed DAQ software was to automate the test procedure by controlling the actuator, controlling the MR damper input current, and measuring the sensor readings. A schematic figure of the architecture of the MR damper test apparatus is illustrated in Figure 5.1 (c).

The MR damper used in this study had very complicated nonlinearities: a hysteretic nonlinearity due to the viscous action of the MR fluid combined with a dead-space nonlinearity due to a mechanical gap in the damper. Figure 5.2 illustrates the time histories of the measured displacement, velocity and force under sinusoidal excitation. For the given displacement that was controlled by the actuator controller, the measured force shows the combination of the dead-space nonlinearity due to a mechanical gap near the damper's neutral position (i.e., $x \approx 0$) and the viscous nonlinearity due to the MR damper characteristics within the remaining displacement range. In Figure 5.1, the mechanical gap can be seen to be approximately 0.9 mm.

5.2.2 Test Protocols

A series of tests was performed with different statistics of the damper input current. A total of eight test sets was conducted, with four different mean values (μ_I) and two different values of standard deviation (σ_I), for the MR damper input current (I): μ_I = 1.0 A, 0.8 A, 0.6 A and 0.4 A, and σ_I = 0.1 A and 0.15 A. Consequently, for each data set, the input current had a Gaussian distribution of $N \sim (\mu_I, \sigma_I)$. Therefore, the effective (nominal) characteristics of the MR damper are determined by means of μ_I, and the uncertainty of the MR damper with

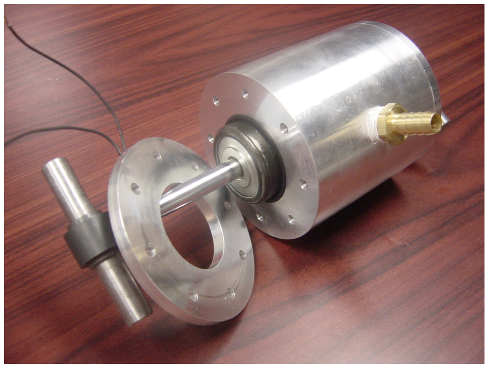

(a) The MR damper mounted
with the water cooler

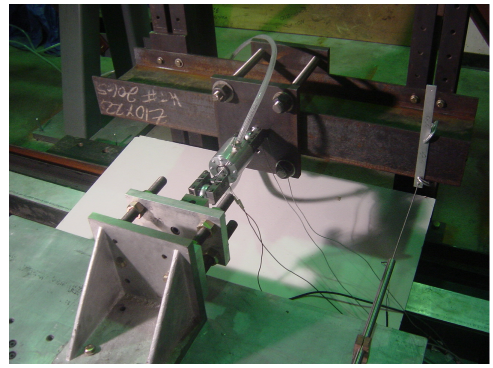

(b) The MR damper installed
on the actuator

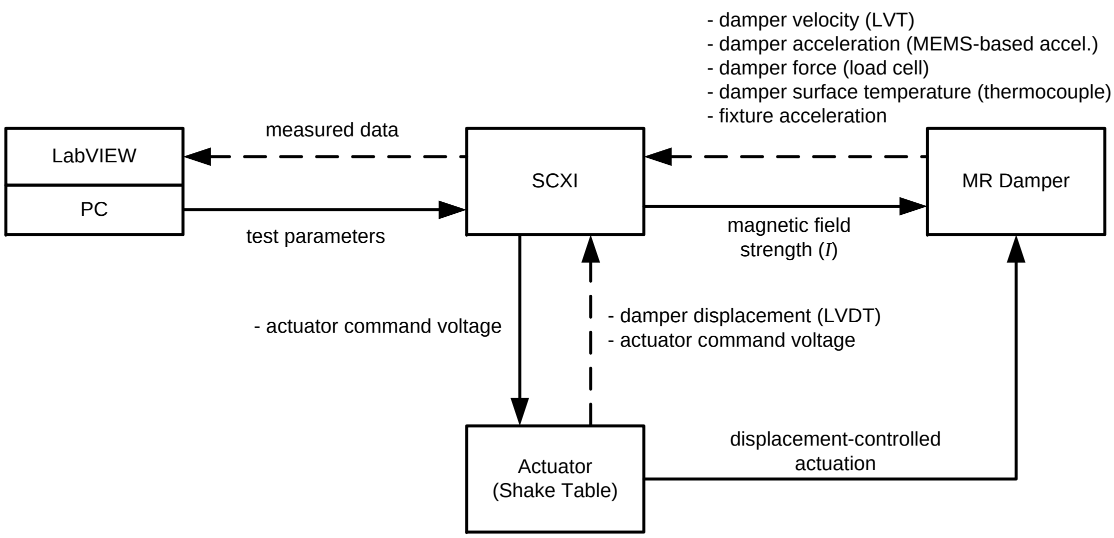

(c) A schematic of the instrumentation system architecture

Figure 5.1: The magneto-rheological (MR) damper test apparatus.

σ_I. For each test set, 500 experiments were conducted. Consequently, a total of 4000 tests was performed in this study. The MR damper was subjected to broadband random excitation with cutoff frequencies of $0.1 \sim 3.0$ Hz. The test protocols using the MR damper are summarized in Table 5.1.

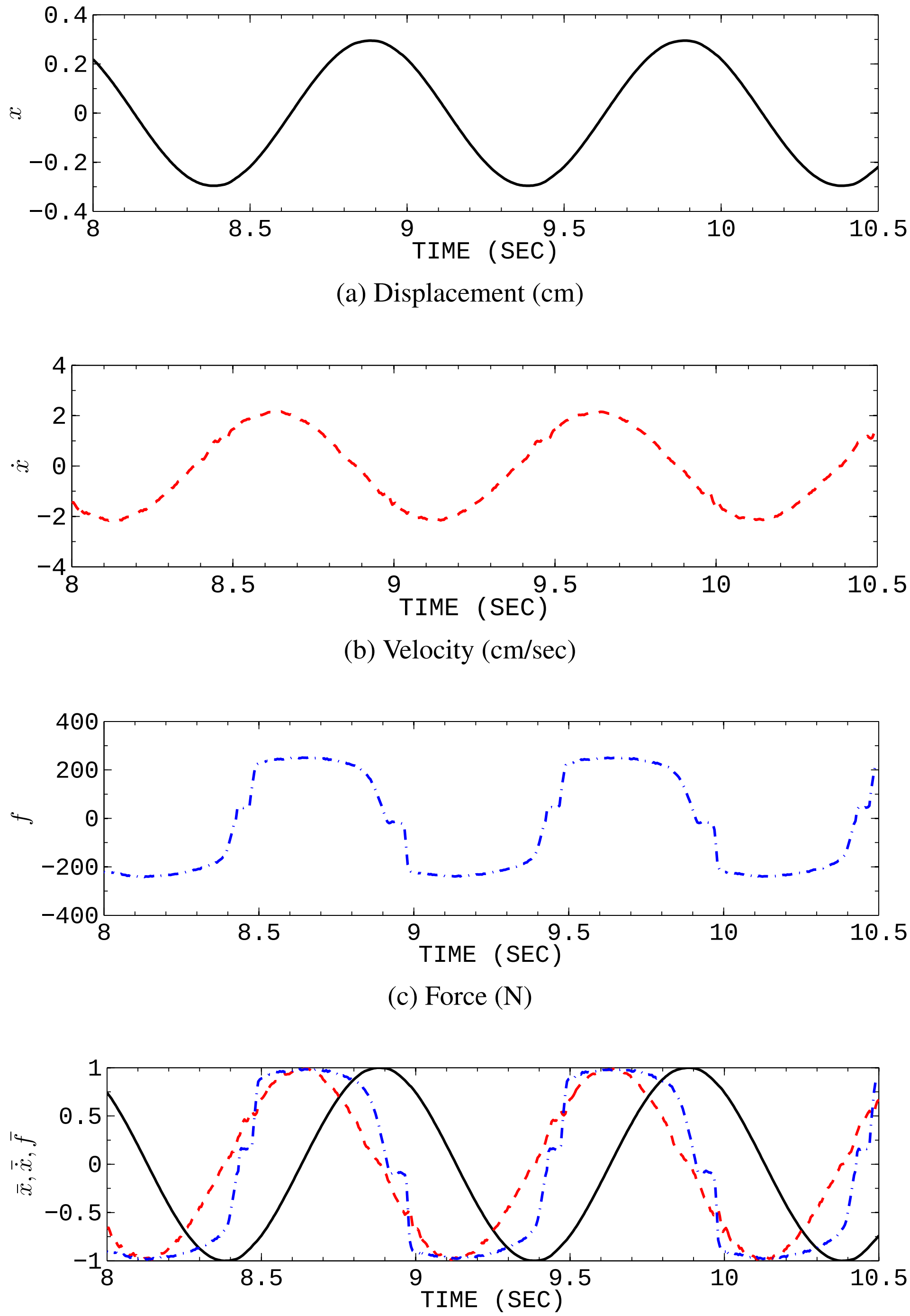

(a) Displacement (cm)

(b) Velocity (cm/sec)

(c) Force (N)

(d) Normalized displacement, velocity and force

Figure 5.2: Time histories of the measured and normalized displacements, velocities and forces of the MR damper subjected to sinusoidal excitation.

Table 5.1: MR damper test protocols.

Test no.	Input current (A) mean	Input current (A) stdv	Input current distribution	Sample size	Excitation
A_1	1.0	0.10			
A_2	1.0	0.15			
B_1	0.8	0.10			Deterministic
B_2	0.8	0.15	Gaussian	500	broadband-random
C_1	0.6	0.10			(0.1 $\sim$ 3.0 Hz)
C_2	0.6	0.15			
D_1	0.4	0.10			
D_2	0.4	0.15			

5.3 Non-Parametric Identification of MR-Damper

5.3.1 Overview of Restoring Force Method

The Restoring Force Method (RFM) is a non-parametric identification technique for nonlinear dynamic systems (Masri and Caughey, 1979; Worden and Tomlinson, 2001). A SDOF nonlinear system can be modeled using a two-dimensional series expansion of the Chebyshev polynomials:

$$r(x, \dot{x}) = \sum_{i=0}^{P} \sum_{j=0}^{Q} \bar{C}_{ij} T_i(\bar{x}) T_j(\bar{\dot{x}}) \tag{5.3}$$

where $r(x, \dot{x})$ is the restoring force of the nonlinear dynamic system, the $\bar{C}_{ij}$ is the normalized Chebyshev coefficient, $T_i(\bullet)$ is the i^{th} order Chebyshev polynomial, P and Q are the highest orders of the Chebyshev polynomial of the normalized displacement ($\bar{x}$) and velocity ($\bar{\dot{x}}$) within the range of [-1,1]. For given measured vectors of x, $\dot{x}$, and r, the $\bar{C}_{ij}$ can be identified as

$$\bar{C}_{ij} = \frac{< r(t), T_i(\bar{x}) T_j(\bar{\dot{x}}) >}{< T_i(\bar{x}) T_j(\bar{\dot{x}}), T_i(\bar{x}) T_j(\bar{\dot{x}}) >} = \frac{\int\int w(\bar{x}) w(\bar{\dot{x}}) r(t) T_i(\bar{x}) T_j(\bar{\dot{x}}) d\bar{x} d\bar{\dot{x}}}{\int\int T_i(\bar{x})^2 T_j(\bar{\dot{x}})^2 d\bar{x} d\bar{\dot{x}}}, \tag{5.4}$$

where $w(\cdot)$ is the weighting function. Once the $\bar{C}_{ij}$ is identified, the normalized and de-normalized power series coefficients ($\bar{a}_{ij}$ and a_{ij}, respectively) can be identified as

$$r(x, \dot{x}) = \sum_{i=0}^{P} \sum_{j=0}^{Q} \bar{C}_{ij} T_i(\bar{x}) T_j(\bar{\dot{x}}) = \sum_{i=0}^{P} \sum_{j=0}^{Q} \bar{a}_{ij} \bar{x}^i \bar{\dot{x}}^j = \sum_{i=0}^{P} \sum_{j=0}^{Q} a_{ij} x^i \dot{x}^j \tag{5.5}$$

using the following relationships (Mason and Handscomb, 2003):

$$T_0(y) = 1, \quad T_1(y) = y, \quad T_2(y) = 2y^2 - 1, \ldots, \quad T_{n+1}(y) = 2yT_n(y) - T_{n-1}(y), \ldots \tag{5.6}$$

5.3.2 Identification Results for the MR Damper

The MR damper was identified using the RFM for the measured data sets in Table 5.1. In order to understand the model-order reduction effects on the identification results, the normalized mean square errors (NMSE) of the RFM identification for different model-orders were measured as

$$\text{NMSE} = \frac{1}{m\sigma_f^2} \sum_{i=1}^{m} (f_i - \hat{f}_i)^2 \tag{5.7}$$

where m is the number of data points, f is the measured force, $\hat{f}$ is the identified force, and σ_f is the standard deviation of the measured force (Worden and Tomlinson, 2001). Figure 5.3 (a) shows the relationship between the series order and the NMSE. The NMSE decreases rapidly from order 1 to 5, and the slope becomes gradually saturated from order 6 to 20. Hence, the MR damper was identified with the model orders of 5 and 20 ($O(5)$ and $O(20)$, respectively) to investigate the effects of the model-order reduction. For $O(5)$ and $O(20)$, a total of 8000 RFM identifications was performed (i.e., 2 model complexities $\times$ 4 input current means $\times$ 2 input current standard deviations $\times$ 500 observations). In the RFM identification, the contribution of each Chebyshev polynomial term can be measured using the following normalized weighting equation:

$$\bar{w}_{ij} = \frac{\bar{C}_{ij}^2}{\sum_{p=0}^{P} \sum_{q=0}^{Q} \bar{C}_{pq}^2} \tag{5.8}$$

The identification results showed that the three most significant terms in the identification were the linear damping ($\bar{C}_{01}$), linear stiffness ($\bar{C}_{10}$), cubic damping ($\bar{C}_{03}$) and cubic stiffness ($\bar{C}_{30}$). The cumulative weight for these terms was greater than 90% for both modeling orders. Table 5.2 summarizes the statistics of $\bar{C}_{01}$, $\bar{C}_{10}$, $\bar{C}_{03}$, the corresponding power series coefficients ($\bar{a}_{01}$, $\bar{a}_{10}$, $\bar{a}_{03}$), and the NMSE of the RFM identification for $O(5)$ and $O(20)$.

5.3.3 Physical Interpretations Without Assuming System Models

Figure 5.3 (b)-(d) show the velocity-force plot of the measured and identified response with $O(5)$ and $O(20)$. Figure 5.3 (c) shows that with the $O(5)$, although the majority of traces of the velocity-force plot can be identified, the details of the traces largely due to the dead-space nonlinearity fail to be identified. Using the basis functions of the Chebyshev polynomials, "smooth" (or continuous) nonlinearities can be identified using a relatively small number of the series expansion terms. However, for discontinuous nonlinearity, such as the dead-space nonlinearity, a relatively large number of the series expansion terms is usually needed of the same basis functions. Figure 5.3 (C) shows that with the higher $O(20)$, the discontinuous nonlinearity are fairly accurately identified.

Table 5.2: Summary of the identification results for the MR damper using the Restoring Force Method.

(a) Normalized Chebyshev Coefficients ($\bar{C}_{ij}$)

Order	Test no.	1st stiffness ($\bar{C}_{10}$) mean	stdv	cv	1st damping ($\bar{C}_{01}$) mean	stdv	cv	3rd stiffness ($\bar{C}_{03}$) mean	stdv	cv
5	A_1	337.88	80.46	0.2381	1038.40	180.30	0.1736	-255.60	49.99	-0.1956
	A_2	330.07	110.38	0.3344	1018.04	257.94	0.2534	-249.14	71.99	-0.2889
	B_1	502.14	60.83	0.1211	1348.91	99.05	0.0734	-324.02	24.96	-0.0770
	B_2	491.39	85.59	0.1742	1328.49	162.36	0.1222	-318.98	41.20	-0.1292
	C_1	573.79	54.61	0.0952	1511.32	67.97	0.0450	-357.11	17.73	-0.0497
	C_2	571.06	67.76	0.1187	1502.65	103.44	0.0688	-354.69	25.79	-0.0707
	D_1	624.05	43.21	0.0692	1618.85	53.48	0.0330	-386.94	17.29	-0.0447
	D_2	619.77	50.65	0.0817	1612.89	75.61	0.0469	-385.18	21.13	-0.0549
20	A_1	360.56	86.72	0.2405	1048.99	183.05	0.1754	-270.00	53.09	-0.1966
	A_2	352.44	117.60	0.3373	1028.54	264.32	0.2570	-263.08	77.02	-0.2928
	B_1	541.28	65.98	0.1219	1364.32	100.87	0.0739	-343.60	26.80	-0.0780
	B_2	529.02	93.41	0.1766	1342.24	166.03	0.0124	-337.73	44.35	-0.0131
	C_1	619.45	59.27	0.0957	1530.89	69.27	0.0452	-380.29	18.98	-0.0499
	C_2	615.86	73.37	0.1191	1522.08	105.47	0.0693	-377.95	27.99	-0.0741
	D_1	668.16	48.02	0.0719	1637.19	54.24	0.0331	-412.16	17.16	-0.0416
	D_2	664.76	56.02	0.0843	1632.14	77.78	0.0477	-410.72	22.80	-0.0555

(b) Normalized Power Series Coefficients ($\bar{a}_{ij}$)

Order	Test no.	1st stiffness ($\bar{a}_{10}$) mean	stdv	cv	1st damping ($\bar{a}_{01}$) mean	stdv	cv	3rd stiffness ($\bar{a}_{03}$) mean	stdv	cv
5	A_1	647.78	170.41	0.2631	2340.12	430.94	0.1842	-3179.03	644.04	-0.2026
	A_2	881.37	229.41	0.3658	2283.33	612.69	0.2683	-3089.39	881.37	-0.2853
	B_1	942.21	137.39	0.1458	3034.01	243.71	0.0803	-4314.57	470.03	-0.1089
	B_2	922.13	172.21	0.1867	2983.92	385.27	0.1291	-4233.05	650.00	-0.1536
	C_1	1076.99	139.31	0.1293	3383.90	193.39	0.0571	-4822.62	472.61	-0.0980
	C_2	1072.01	153.27	0.1430	3363.73	265.94	0.0791	-4792.21	548.46	-0.0114
	D_1	1210.75	115.62	0.0954	3612.91	167.06	0.0462	-5026.61	467.50	-0.0930
	D_2	1189.28	141.32	0.1188	3603.26	201.03	0.0558	-5019.45	480.98	-0.0958
20	A_1	430.95	549.97	1.2762	3205.08	658.45	0.2054	-18432.98	19792.93	-1.0738
	A_2	500.18	526.79	1.0532	3084.24	815.13	0.2643	-16998.43	20179.07	-1.1871
	B_1	777.02	840.00	1.0810	4498.72	929.77	0.2067	-41326.02	33137.60	-0.8019
	B_2	811.18	737.51	0.9092	4369.22	981.22	0.2246	-38265.26	31812.22	-0.8314
	C_1	1036.13	921.20	0.8891	4913.95	1009.55	0.2054	-43620.36	37791.24	-0.8664
	C_2	1054.86	979.76	0.9288	4916.29	1007.44	0.2049	-44503.36	35387.04	-0.7952
	D_1	1163.74	968.06	0.8318	4615.94	1036.27	0.2245	-24603.48	39224.80	-1.5943
	D_2	1167.03	963.62	0.8257	4712.44	1037.13	0.2201	-28390.98	39049.60	-1.3754

(c) Normalized Mean Square Error (NMSE)

Order	Test no.	mean	stdv	cv	Order	Test no.	mean	stdv	cv
5	A_1	0.1532	0.0118	0.0769	20	A_1	0.1173	0.0196	0.1669
	A_2	0.1516	0.0138	0.0908		A_2	0.1150	0.0242	0.2106
	B_1	0.1733	0.0195	0.1128		B_1	0.1419	0.0218	0.1538
	B_2	0.1720	0.0203	0.1179		B_2	0.1406	0.0235	0.1672
	C_1	0.1769	0.0187	0.1056		C_1	0.1484	0.0210	0.1414
	C_2	0.1768	0.0184	0.1039		C_2	0.1494	0.0213	0.1422
	D_1	0.1828	0.0108	0.0593		D_1	0.1579	0.0161	0.1018
	D_2	0.1822	0.0115	0.0629		D_2	0.1579	0.0172	0.1090

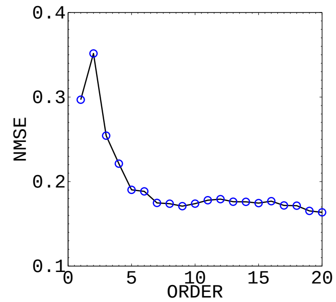

(a) Order vs. NMSE

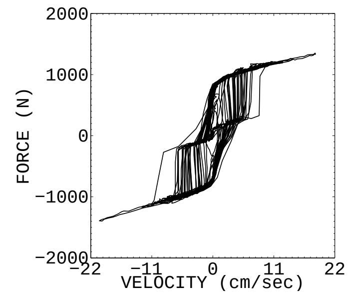

(b) Measured

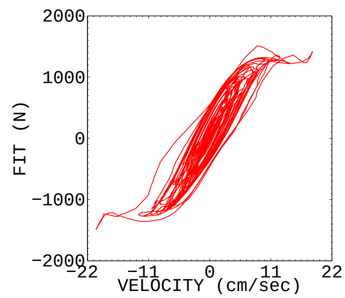

(c) Identified (order 5)

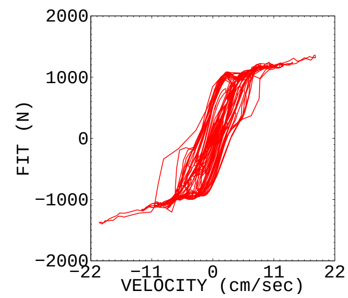

(d) Identified (order 20)

Figure 5.3: A sample identification result for the MR damper using the Restoring Force Method.

Physical interpretations without assuming system models

As discussed earlier, the RFM can be used to identify nonlinear systems without *a priori* knowledge of the systems because the method is model-independent and data-driven, like other non-parametric identification methods. Using the RFM, some physical interpretations are also possible with the identified coefficients. For example, the restoring force of nonlinear systems can be modeled as

$$r(x, \dot{x}) = r_x + r_{\dot{x}} + r_{x,\dot{x}}, \tag{5.9}$$

where r_x is the restoring force component that is dependent on the displacement only, $r_{\dot{x}}$ is the restoring force component dependent on the velocity only, and $r_{x\dot{x}}$ is the restoring force component that depends on both displacement and velocity. In the RFM, the components r_x, $r_{\dot{x}}$, and $r_{x\dot{x}}$ can be expressed, by grouping the terms of the series expansion as

$$r_x = \sum_{i=0}^{P} \bar{C}_{i0} T_i(\bar{x}) = \sum_{i=0}^{P} \bar{a}_{i0} \bar{x}^i \tag{5.10}$$

$$r_{\dot{x}} = \sum_{j=0}^{Q} \bar{C}_{0j} T_j(\bar{\dot{x}}) = \sum_{i=0}^{P} \bar{a}_{0j} \bar{\dot{x}}^j \tag{5.11}$$

$$r_{x\dot{x}} = \sum_{i=1}^{P} \sum_{j=1}^{Q} \bar{C}_{ij} T_i(\bar{x}) T_j(\bar{\dot{x}}) = \sum_{i=1}^{P} \sum_{j=1}^{Q} \bar{a}_{ij} \bar{x}^i \bar{\dot{x}}^j \tag{5.12}$$

First, using the r_x, $r_{\dot{x}}$, and $r_{x\dot{x}}$, some physical interpretations can be made with the identified RFM coefficients without assuming any system models. The effects of different modeling complexities for the same input current were studied. Figure 5.4 shows the phase plots of the r_x and $r_{\dot{x}}$ using the orthogonal Chebyshev and non-orthogonal power series basis functions. In the figure, the identified forces are shown as the solid lines, and the measured forces as the dashed lines. The first row shows the displacement-force plots of r_x for the power series and Chebyshev polynomials with the model complexities of $O(5)$ and $O(20)$, and the second row shows the corresponding velocity-force plots of $r_{\dot{x}}$. For the same model complexity of $O(5)$, the identified r_x and $r_{\dot{x}}$ with the power series and Chebyshev polynomials are different because of employing different basis functions (Figures 5.4 (a) and (b), and Figures 5.4 (d) and (e)). The identified r_x and $r_{\dot{x}}$ for both polynomials trace the slopes of the displacement-force and velocity-force plots, respectively. The identified r_x with the power series polynomials, however, is approximately 50% less than the measured force at the peak displacements of approximately $\pm$1.3 cm, while the identified r_x with the Chebyshev polynomials is almost the same as the measured force at the peak displacements. In the comparison of $O(5)$ and $O(20)$ using the Chebyshev polynomials as

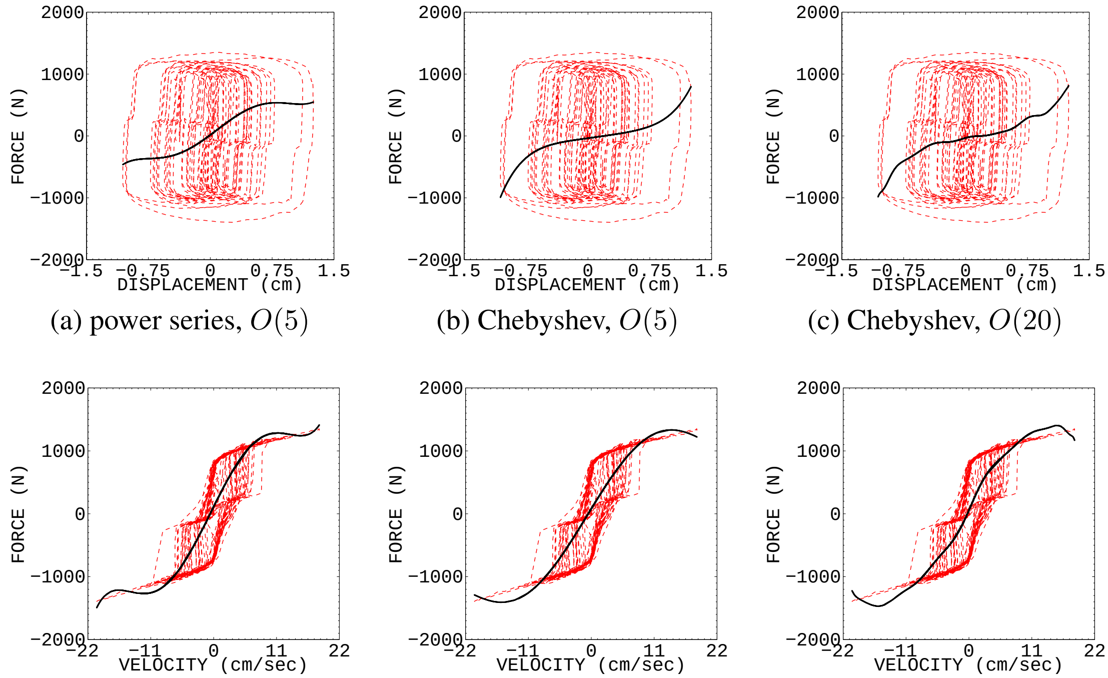

(a) power series, $O(5)$ (b) Chebyshev, $O(5)$ (c) Chebyshev, $O(20)$

(d) power series, $O(5)$ (e) Chebyshev, $O(5)$ (f) Chebyshev, $O(20)$

Figure 5.4: The identified restoring forces that are dependent on the displacement only (r_x) and velocity only ($r_{\dot{x}}$) using the non-orthogonal power series ($\bar{a}_{ij}$) and orthogonal Chebyshev ($\bar{C}_{ij}$) polynomials for different identification model orders ($O(N)$). The solid lines are of the identified force, and the dashed lines are of the measured force. In the top row, (a) the r_x with the power series polynomials for $O(5)$, (b) the r_x with the Chebyshev polynomials for $O(5)$, and (c) the r_x with the Chebyshev polynomials for $O(20)$. In the second row, (d) the $r_{\dot{x}}$ with the power series polynomials for $O(5)$, (e) the $r_{\dot{x}}$ with the Chebyshev polynomials for $O(5)$, and (f) the $r_{\dot{x}}$ with the Chebyshev polynomials for $O(20)$.

shown in Figures 5.4 (b) and (c), and Figures 5.4 (e) and (f), the slopes of the r_x and $r_{\dot{x}}$ become more accurate with the higher $O(20)$, but the improvement is not significant.

Second, the effects of the system changes on the identified coefficients were investigated. In general, the stiffness and damping characteristics of dynamic systems can be determined with the slopes of the phase plots. That is, if the system stiffness is large, the identified $\bar{a}_{i0}$ and $\bar{C}_{i0}$ become large, and *vice versa*. Similarly, if the system damping is large, the $\bar{a}_{0j}$ and $\bar{C}_{0j}$ terms become large, and *vice versa*. Figure 5.5 illustrates the changes of the identified r_x,

$r_{\dot{x}}$, and $r_{x\dot{x}}$ for different MR damper input currents. With the $O(20)$, the first row shows the phase plots of the r_x, $r_{\dot{x}}$, and $r_{x\dot{x}}$ for $I = 1.0$ A (Figures 5.5 (a) to (c), respectively), and the second row shows the phase plots for $I = 0.4$ A (Figures 5.5 (d) to (f), respectively). In the identification, the Chebyshev polynomials were used. The identified r_x, $r_{\dot{x}}$, and $r_{x\dot{x}}$ are shown as solid lines and the measured force as dashed lines in the figure. When the I changes, both the stiffness and damping characteristics of the MR damper change. The exact relationships of the stiffness and damping characteristics on the current I are very complicated nonlinear functions influenced also by the MR fluid properties, electro-magnet design, and damper cylinder and orifice design. Various mechanical models of the MR and controllable dampers can be found in the works by Ehrgott and Masri (1992). Although no damper models are assumed in the RFM identification, the data-driven technique automatically adjusts its coefficients to obtain the best fit for given data sets. Consequently, in the figure, the slopes of r_x and $r_{\dot{x}}$ for the displacement and velocity decrease as the I decreases (Figures 5.5 (a) and (d), and Figures 5.5 (b) and (e)), and the area of $r_{x\dot{x}}$ also decreases as I decreases (Figures 5.5 (c) and (f)). Figure 5.6 also shows the changes of the Chebyshev coefficients for the different input currents. The changes of the MR damper characteristics are reflected in the identified Chebyshev coefficients as shown in the figure.

Hence, the above identification results indicate that the identified RFM coefficients could be used as excellent indicators for change detection of a complicated nonlinear system. Using the information of system characteristics contained in the identified coefficients, some physical interpretation of the detected change would be possible. A question is left: among three kinds of the RFM coefficients, $\bar{C}_{ij}$, $\bar{a}_{ij}$, and a_{ij}, which kind is more useful to detect the changes in the

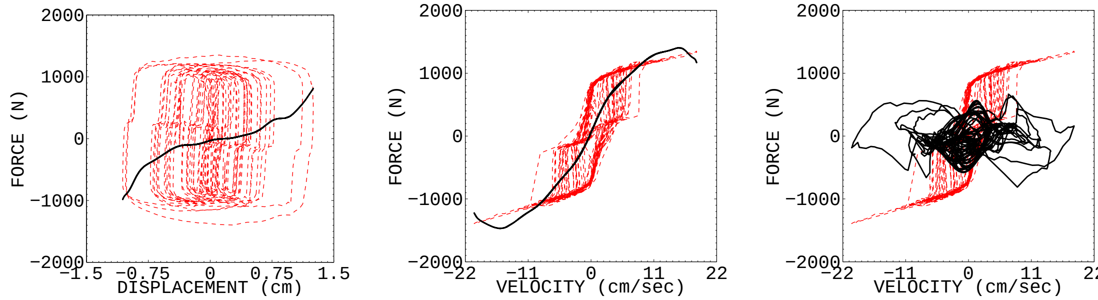

(a) Disp. only ($I = 1.0$ A) (b) Vel. only ($I = 1.0$ A) (c) Coupled ($I = 1.0$ A)

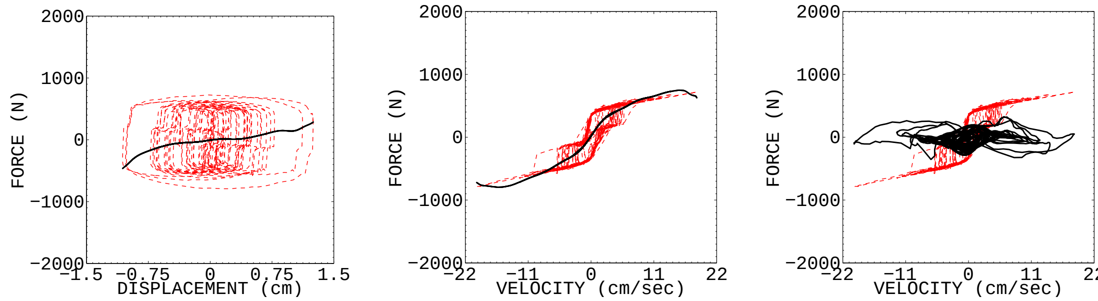

(d) Disp. only ($I = 0.4$ A) (e) Vel. only ($I = 0.4$ A) (f) Coupled ($I = 0.4$ A)

Figure 5.5: Changes of the identified restoring forces that are dependent on the displacement only (r_x), velocity only ($r_{\dot{x}}$), and coupled with both displacement and velocity ($r_{x\dot{x}}$) for different MR damper input current (I) of 1.0 A and 0.4 A. In the identification, the Chebyshev polynomials were used as the basis functions, and the model complexity ($O(N)$) was fixed at 20 for both input current cases. The solid lines are of the identified restoring forces, and the dashed lines are of the measured forces. The top row shows the phase plots of the displacement and force, and the second row shows the phase plots of the velocity and force.

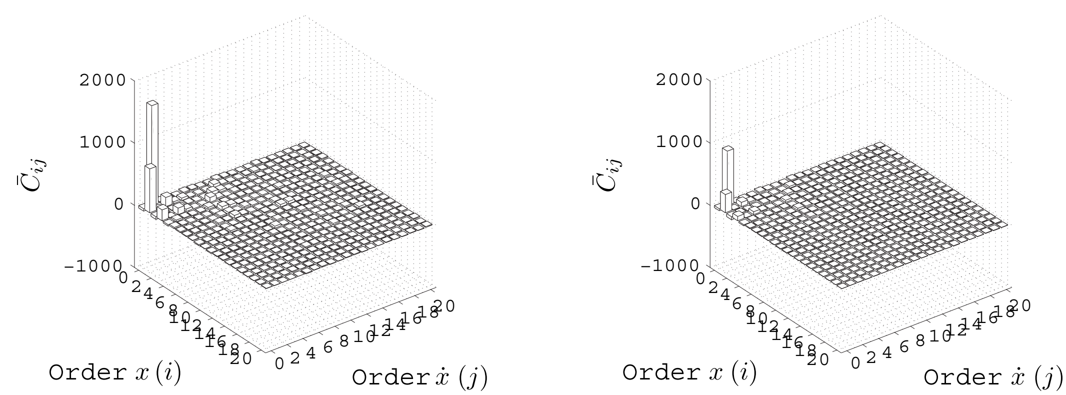

Figure 5.6: Changes of the identified normalized Chebyshev coefficients for different MR damper input currents (I) of 1.0 A and 0.4 A. The identification was performed using the Restoring Force Method with the model complexity of $O(20)$ for both input currents.

uncertain nonlinear system? In the next section, the stochastic properties of the RFM coefficients are discussed.

5.3.4 Stochastic Properties of the Identified RFM Coefficients

As shown in Equations 5.3 and 5.5, three kinds of equivalent coefficients are available using the RFM: the normalized Chebyshev coefficients ($\bar{C}_{ij}$), normalized power series coefficients ($\bar{a}_{ij}$), and de-normalized power series coefficients (a_{ij}). The basis functions for the $\bar{C}_{ij}$ are orthogonal, while the basis functions for the $\bar{a}_{ij}$ and a_{ij} are non-orthogonal. The orthogonality of the basis functions significantly influences the stochastic properties of the identified coefficients, and as well as the performances of the system change detection capability. An analytical description of the stochastic effects of the orthogonality on the identified coefficients is provided below.

Biasness of the identified coefficients

Three kinds of orthogonal basis functions are generally used in system identification: (1) polynomial orthogonal functions, (2) piecewise constant orthogonal functions, and (3) Fourier (sine-cosine) functions. An excellent overview of using orthogonal basis functions for system identification and control application can be found in Datta and Mohan (1995). In system identification, the polynomial orthogonal functions are advantageous to identify continuous nonlinearities, while the piecewise constant orthogonal functions are advantageous for discontinuous nonlinearities by using a smaller number of terms in the identification for each function kind.

In general, the identified restoring forces for the reduced-order and higher-order models can be expressed as

$$\hat{r}_h = \hat{r}_l + \hat{r}_e = \hat{\phi}_l \psi_l + \hat{\phi}_e \psi_e = \hat{\phi}_h \psi_h \tag{5.13}$$

where $\hat{r}_l$ and $\hat{r}_h$ are the restoring force components identified with a reduced-order model and higher-order model, respectively, $\hat{r}_e$ is the residual between $\hat{r}_h$ and $\hat{r}_l$, $\hat{\phi}_h$ and $\hat{\phi}_l$ are the identified model parameters for the higher-order and reduced-order models, respectively, $\hat{\phi}_e$ is the identified model parameters for the residual, ψ_h and ψ_l are the basis functions for the higher and reduced-order models, and ψ_e is the basis function for the restoring force residual. The identified model parameters can be estimated as

$$E[\hat{\phi}_h] = \frac{< \hat{r}_h, \psi_l >}{< \psi_l, \psi_l >} = \frac{< \hat{\phi}_l \psi_l + \hat{\phi}_e \psi_e, \psi_l >}{< \psi_l, \psi_l >} = \hat{\phi}_l \frac{< \psi_l, \psi_l >}{< \psi_l, \psi_l >} + \hat{\phi}_e \frac{< \psi_e, \psi_l >}{< \psi_l, \psi_l >} = \hat{\phi}_l + \hat{\phi}_e \Psi_e \tag{5.14}$$

where $< \bullet >$ is the inner product of two functions. Therefore, the biasness of the reduced-order model parameter ($\hat{\phi}_h$) depends on the significance of the term $\hat{\phi}_e \Psi_e$. For the RFM, the orthogonality of the Chebyshev polynomial basis functions is guaranteed with the normalized displacement ($\bar{x}$) and velocity ($\bar{\dot{x}}$) within the range of [-1, 1]. Consequently, the identified $\bar{C}_{ij}$ become unbiased because ψ_l and ψ_e are orthogonal, and $\hat{\phi}_e \Psi_e = 0$. Consequently,

$$E[\hat{\phi}_h] = \hat{\phi}_l \;\; \text{(unbiased)}, \qquad \text{when } \psi_l \text{ and } \psi_e \text{ are orthogonal.} \tag{5.15}$$

Figure 5.7 shows a comparison of term-wise identification results, with different modeling orders, for the normalized Chebyshev polynomial basis functions. In the figure, the first row shows the term-wise identification results with the $O(5)$ for the linear damping (a), cubic damping (b) and linear stiffness terms (c), and the second row shows the same term-wise identified restoring forces with the $O(20)$ since the term-wise identification results with $O(5)$ and $O(20)$

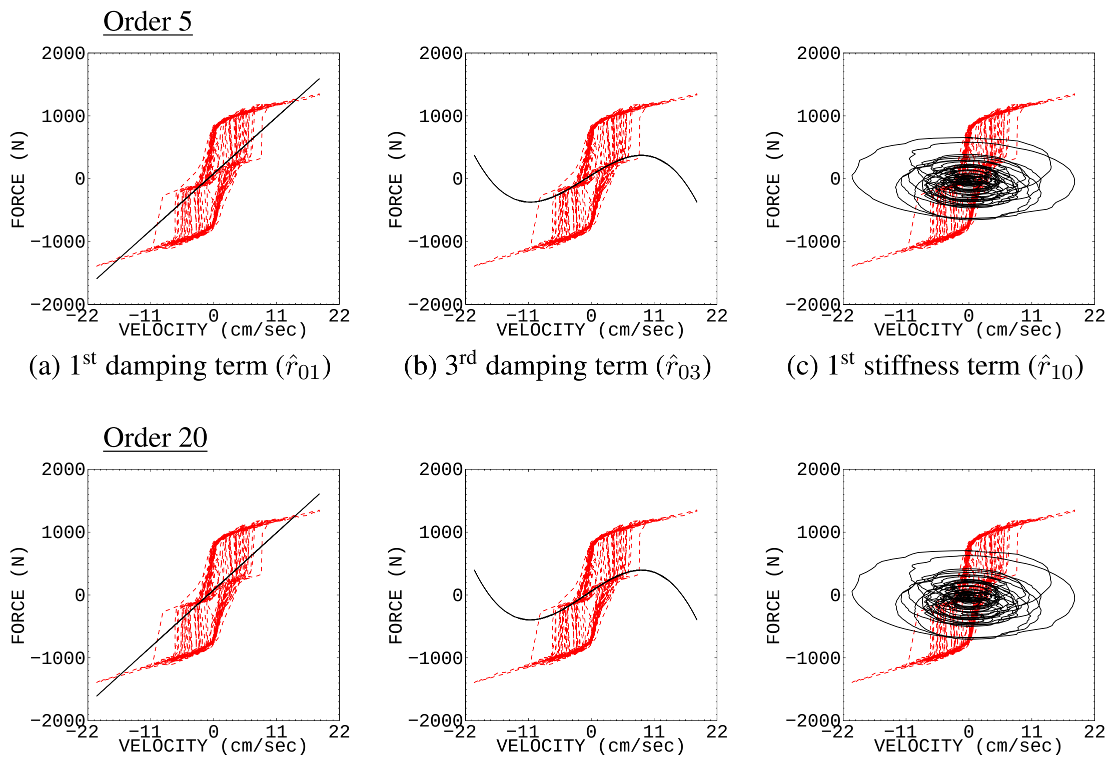

(a) 1st damping term ($\hat{r}_{01}$) (b) 3rd damping term ($\hat{r}_{03}$) (c) 1st stiffness term ($\hat{r}_{10}$)

(d) 1st damping term ($\hat{r}_{01}$) (e) 3rd damping term ($\hat{r}_{03}$) (f) 1st stiffness term ($\hat{r}_{10}$)

Figure 5.7: Term-wise identification results with model orders of 5 and 20 with the normalized Chebyshev polynomial basis functions.

are identical. The comparison shows clearly that the identified Chebyshev coefficients are not biased with respect to the model complexity.

The unbiasness is not generally true for non-orthogonal basis functions. Table 5.3 shows the stochastic effects of the model-order reduction on the identified coefficients with the Chebyshev and power series polynomials. For the Chebyshev polynomials, both the means and standard deviations of the identified coefficients for different model orders are approximately the same, which indicates the statistical unbiasness of the identified coefficients. For the power series polynomials, however, significant biasness is observed with the mean of the identified coefficients: the mean ratio with $O(5)$ and $O(20)$ varies from 20.4% to 104.0%. The standard deviation of the identified coefficients were also significantly varies with different model complexities: the ratio of the $O(5)$ and $O(20)$ varies within the range of 1.19% to 16.1%. The results demonstrate that for different levels of modeling complexity, the identified coefficients with the orthogonal basis functions are statistically unbiased, while the identified coefficients with the non-orthogonal basis functions are significantly statistically biased.

Table 5.3: Stochastic effects of model-order reduction on the coefficient identification with orthogonal and non-orthogonal basis functions. The (%) column shows the percentage fraction of $O(5)/O(20)$.

	Chebyshev polynomials (orthogonal)						Power series polynomials (non-orthogonal)					
term	mean			stdv			mean			stdv		
(i,j)	$O(5)$	$O(20)$	(%)	$O(5)$	$O(20)$	(%)	$O(5)$	$O(20)$	(%)	$O(5)$	$O(20)$	(%)
$(0,1)$	1618.9	1637.2	98.9	53.5	54.2	98.6	3612.9	4615.9	78.3	167.7	1036.3	16.1
$(1,0)$	624.1	668.2	93.4	43.2	48.0	90.0	1210.8	1163.7	104.0	115.6	968.1	11.9
$(0,3)$	14.6	15.6	93.9	17.3	17.2	100.7	-5026.6	-24603.5	20.4	467.5	39224.8	1.19

Distributions of Identified Coefficients

The unbiasness of the identified coefficients using the orthogonal basis functions is critical for implementing the change detection in uncertain nonlinear systems: the the probability of the identified coefficients should be a function of the system uncertainty, not a function of the model complexity. When the unbiasness is guaranteed, the identified coefficients of a reduced-order model can be safely used for change detection. Consequently, change detection could be observed even with a few dominant terms of the identified coefficients. For example, the $O(20)$ model has a total of 441 coefficients. Using the orthogonality property, the testing procedure for change detection could be dramatically simplified by using a smaller number of coefficients. Figure 5.8 shows the bivariate Gaussian probability density functions (pdfs) of the two dominant identified Chebyshev coefficients in the displacement ($\bar{C}_{10}$) and velocity ($\bar{C}_{01}$) for different MR damper input currents. The figure illustrates that, even with two dominant coefficients, the bivariate pdfs can still accurately represent the physical changes in the MR damper.

Figure 5.9 shows the pdfs of the first-order damping coefficient ($\bar{C}_{01}$) for different MR damper input currents. In the figure, the mean of pdfs decreases as the input current decreases. Since the damping force of the MR damper is proportional to the input current (Dyke et al., 1996), it is observed that the mean of $\bar{C}_{01}$ by itself properly represents the actual changes in the damper properties. Figure 5.10 illustrates the current-dependence of the means of the identified Chebyshev coefficients with one standard deviation error bars for different means (μ_I) and standard deviations (σ_I) of input currents. For $\sigma_I = 0.1$ A, as the input current increases, both the first order damping and stiffness coefficients ($\bar{C}_{01}$ and $\bar{C}_{10}$, respectively) increase, while the third order damping coefficient ($\bar{C}_{03}$) decreases (Figure 5.10 (a)). For the same μ_I but different

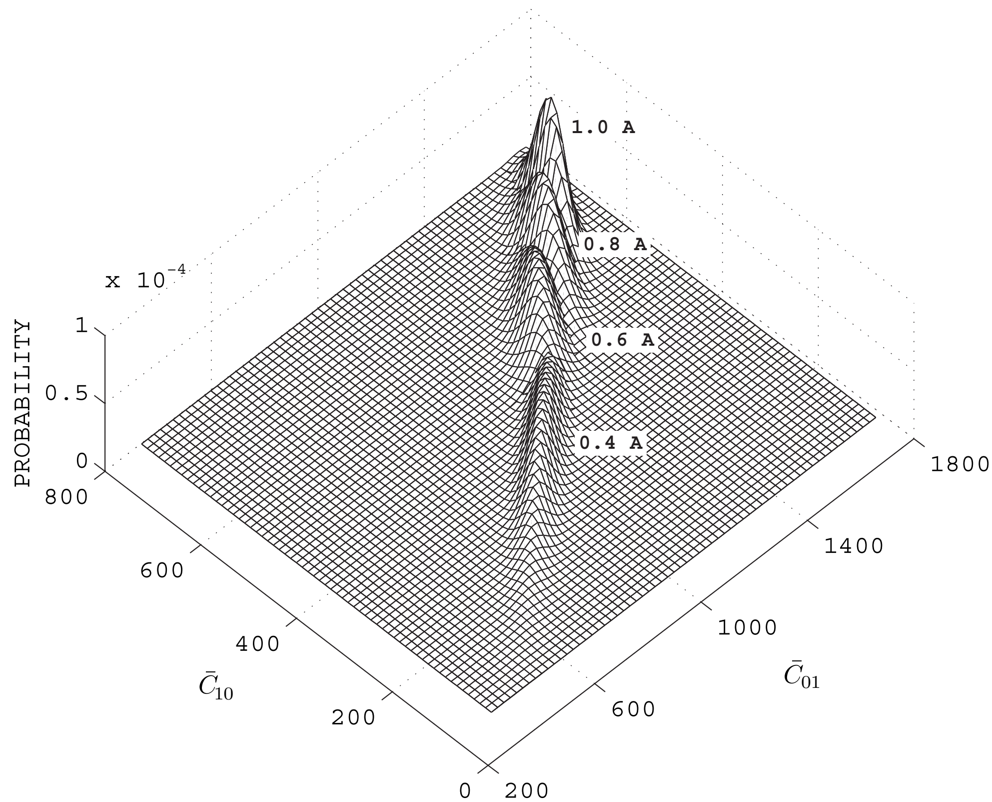

Figure 5.8: Bivariate Gaussian distributions of the identified Chebyshev coefficients of two dominant terms in the velocity ($\bar{C}_{01}$) and displacement ($\bar{C}_{10}$), for different MR damper input currents (Test no. A_1, B_1, C_1, D_1).

σ_I of 0.15 A, the means of the coefficients are almost identical to the means for $\sigma_I = 0.1$ A, but the standard deviation of the identified coefficients increases 42.2% on average (Figure 5.10 (b)). This result indicates that the change of σ_I is also properly reflected in the standard deviation of the identified coefficients.

Based on the above results, the experimental study has demonstrated the following important facts to detect changes in uncertain nonlinear systems:

1. Because the identification procedure of the RFM is data-driven, no *a priori* knowledge of the monitored nonlinear systems is required.

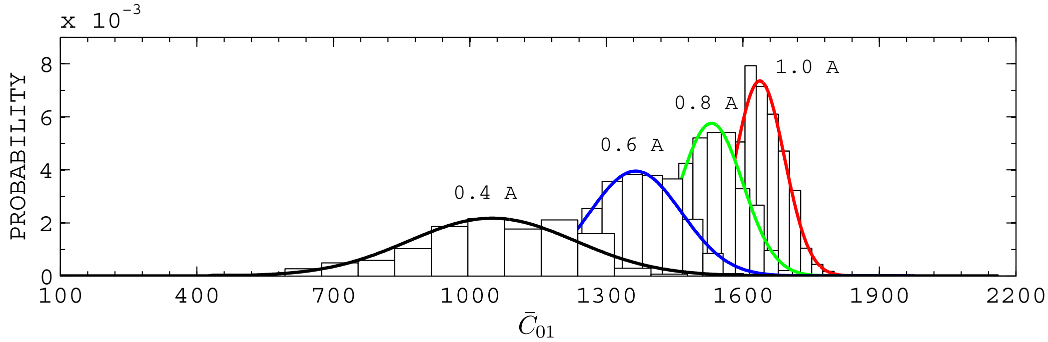

Figure 5.9: The distributions of the identified Chebyshev coefficients for the first order damping ($\bar{C}_{01}$) for different MR damper input currents (Test no. A_1, B_1, C_1 and D_1). In the figure, the smooth factor (bin width) of the histograms were determined with the normal reference rule (or Scott's rule) (Martinez and Martinez, 2002). The pdf's were estimated with the Gaussian distribution assumption.

2. The identified coefficients with the orthogonal basis functions are statistically unbiased with respect to the model complexity.

3. Due to their statistical unbiasness, the identified coefficients (using orthogonal basis functions) with a reduced-order model can be safely used to detect changes in the systems.

4. Using the distributions of the identified coefficients, not only detecting changes in the monitored systems, but also quantifying the detection uncertainty is possible: the mean changes of the distributions measure the genuine system changes, and the standard deviations of the distributions measure the detection uncertainty.

5.4 Stochastic Change Detection of MR Damper

In the previous sections, it was analytically and experimentally demonstrated that the identified coefficients with the orthogonal basis functions are statistically unbiased with respect to the model complexity. In this section, some examples are provided to demonstrate how the unbiased

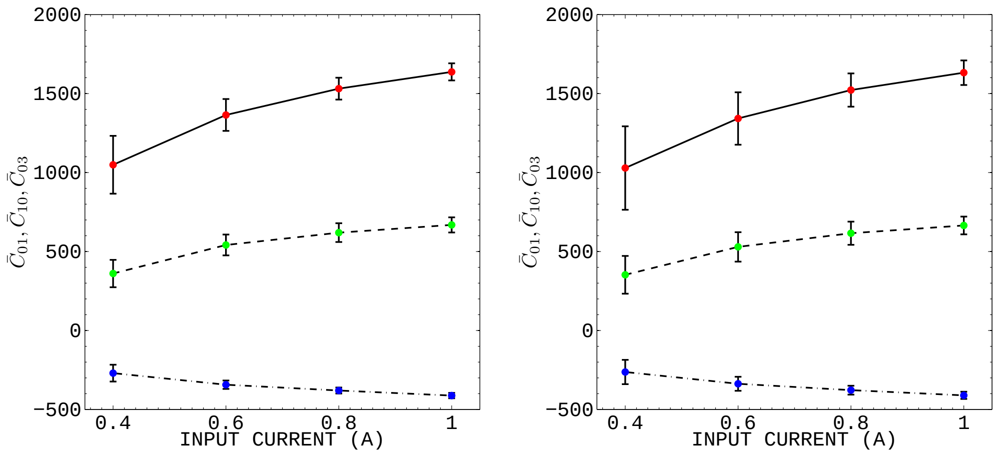

(a) $\sigma_I = 0.1$ A (b) $\sigma_I = 0.15$ A

Figure 5.10: The means of the identified normalized Chebyshev coefficients with 1σ error bars for different MR damper input currents (I). (a) The input current standard deviations of 0.1 A (Test no. A_1, B_1, C_1 and D_1). (b) The input current standard deviations of 0.15 A (Test no. A_2, B_2, C_2 and D_2). In the figures, the solid lines are for $\bar{C}_{01}$, dashed lines for $\bar{C}_{10}$, and dash-dot lines for $\bar{C}_{03}$.

coefficients can be used for the change detection in uncertain nonlinear systems. Two pattern recognition algorithms are used, as supervised and and unsupervised classification methods, in this demonstration. Brief description of both classification approaches will be followed in the next section.

5.4.1 Overview of Statistical Classification with Pattern Recognition Methods

Classification methods

Statistical classification methods are pattern recognition procedures in which the pattern data (or *observations*) are placed into two or more labeled groups (or *classes*) based on one or more characteristics (or *features*). A *classifier* is a nonlinear function mapping an observation in a feature space to a class label. In general, there exist two types of classifiers: supervised classifiers and unsupervised classifiers. The supervised and unsupervised classification are briefly described below. More detailed and formal descriptions of these methods can be found in Duda and Hart (1973).

The *supervised classifiers* require the training pattern data consisting of pairs of feature inputs and desired class labels. Using the training data, the optimal relationships between the feature inputs and class labels can be obtained, minimizing the prediction errors of the desired class labels for the given feature input data. In this study, *Support Vector Machines* are used as an example of supervised classifications for detecting changes in the MR damper. Detailed description of Support Vector Machines will be provided later in Section 5.4.2.

The *unsupervised classifiers* are distinguished from the supervised classifiers by the fact that the unsupervised classifiers do not require the desired class labels. Considering the input features as random variables, this method finds the probabilistic relationships between the input features, commonly employing Bayesian inference to obtain the conditional probabilities of the features. Without this *a priori* information for the classification, the unsupervised classification is often more challenging than the supervised classification. The k-means clustering is one of most widely used unsupervised classification method due to its simple procedure and relatively good classification results (Kanungo et al., 2002). Hence, in this study, the k-means clustering is used as an unsupervised classifier for the change detection in the MR damper. Detailed description of the k-means clustering is provided in Section 5.4.3.

The purpose of the classification demonstration is to illustrate the advantage of using the statistically unbiased coefficients (i.e., $\bar{C}_{ij}$) for the change detection in uncertain nonlinear systems. Consequently, this study focuses on demonstrating the importance of selecting effective features for the system change detection rather than evaluating the performance of different statistical classifiers.

Model selection and error generalization techniques

Accuracy estimation and error generalization are critical steps to select good classifier models and evaluate the performance of the selected models for future data sets (Kohavi, 1995). In both cases, low bias and low variance of the classification results are desirable. If data sets are sufficient, the given data sets are generally partitioned into three groups to perform the following steps: (1) model training, (2) model validation, and (3) model assessment. The *model training* and *model validation* are performed to choose the model with the best performance on new data. For these, the first-group data are used to train different classification models, and the second-group data, which were not used in the model training, are used to select the model with the best performance. Once the best performance model is selected, *model assessment* is performed with the third-group of data sets to estimate the generalization error on future data. However, the given data are often not sufficient to partition into three groups and to perform all the necessary evaluations. In this case, statistical data partitioning and resampling techniques provide effective approaches to maximize the use of a limited amount of data (Efron and Tibshirani, 1993; Martinez and Martinez, 2002).

The *cross-validation method* (CV) is a statistical data-partitioning technique for model selection with an insufficient amount of data. Common types of the CV include: the k-fold cross-validation, and leave-one-out cross-validation. The *k-fold cross-validation* partitions the original data into k subsamples. Of k partitioned subsamples, one subsample is retained for model validation, and the remaining $(k - 1)$ subsamples are used for model training. Then, the same process is repeated with the next subsample to "cross-validate" trained classifier models. Consequently, k accuracy estimates are obtained from the *folds*, and the averaged accuracy is used as the final estimation. The *leave-one-out cross-validation* has similar procedures to the k-fold cross-validation, but this method retains a single observation (or data point) for model validation, and the remaining observations are used for model training. Consequently, if the original data have m observations, the leave-one-out and k-fold cross-validations become identical when $k = m$.

5.4.2 Supervised Change Detection Using Support Vector Classification

Overview of Support Vector Machine classification

The Support Vector (SV) algorithms are statistical learning techniques for various classification and regression problems (Boser et al., 1992; Burges, 1998; Smola and Schölkopf, 1998; Vapnik, 1995, 1998). For the classification problems, the Support Vector Classifiers (SVC) have been successfully used for various system-identification and damage-detection-related applications (Gao et al., 2002; Mita and Hagiwara, 2003; Oh and Beck, 2006; Park et al., 2005; Worden and Lane, 2001; Yun et al., 2006; Zhang et al., 2006). Here, a brief description of the SVC is provided. More complete information on this method can be found in the work by Schölkopf and Smola (2002).

Suppose that m sets are available of training pattern vectors $\mathbf{x}_1, \mathbf{x}_2, \ldots, \mathbf{x}_m$ in a dot product space $\mathcal{H}$ as illustrated in Figure 5.11. If the given training data set is separable, the goal is to find the hyperplane (**H**) with the maximal geometrical margin ρ. The purpose of maximizing ρ is obvious: the classifier becomes robust with the ρ when the training vectors **x** are noisy. If the noise of **x** is bounded in $r > 0$, the separation margin should be $\rho > r$, so that the separating

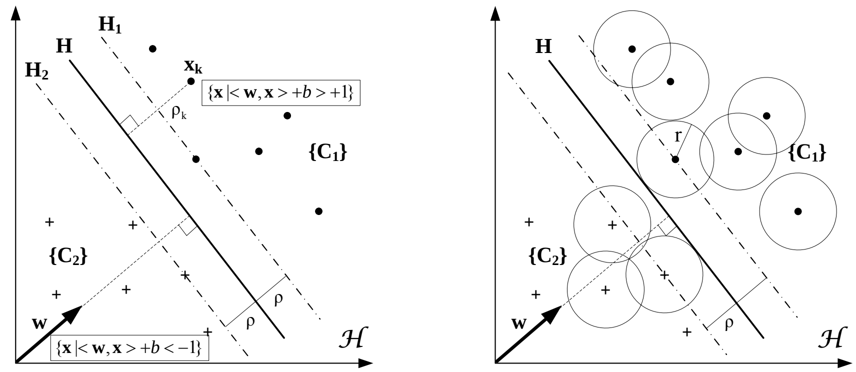

(a) (b)

Figure 5.11: Support Vector Classification.

hyperplane (**H**) correctly classifies the noisy data (Figure 5.11 (b)). Therefore, for a given r of the training pattern vectors, ρ is optimized with the maximal value ρ^* (Schölkopf and Smola, 2002). Any hyperplane **H** in $\mathcal{H}$ can be expressed as

$$\{\mathbf{x} \in \mathcal{H} | < \mathbf{w}, \mathbf{x} > +b = 0\}, \tag{5.16}$$

where **w** is a vector orthogonal to the hyperplane ($\mathbf{w} \in \mathcal{H}$), b is a threshold (and $b \in \Re$), and $< \bullet >$ is a dot product. Because **w** and b are arbitrary, we can imagine two linear hyperplanes as

$$\mathbf{H}_1 := \{x | < \mathbf{w}, \mathbf{x} > +b = +1\}, \quad \mathbf{H}_2 := \{x | < \mathbf{w}, \mathbf{x} > +b = -1\}. \tag{5.17}$$

Then the separation conditions for an arbitrary vector $\mathbf{x}_k$ into two classes become

$$< \mathbf{w}, \mathbf{x} > +b > +1 \quad \text{for } \mathbf{x}_k \in \{\mathbf{C}_1\}, \quad < \mathbf{w}, \mathbf{x} > +b < -1 \quad \text{for } \mathbf{x}_k \in \{\mathbf{C}_2\}. \tag{5.18}$$

Or more concisely,

$$y_k < \mathbf{w}, \mathbf{x} > +b > +1, \qquad \text{where } y_k = \text{sgn}(< \mathbf{w}, \mathbf{x} > +b >). \tag{5.19}$$

Since the distance between $\mathbf{x}_k$ and $\mathbf{H}$ (ρ_k) is given by

$$y_k \frac{(< \mathbf{w}, \mathbf{x} > +b)}{||\mathbf{w}||} \geq \rho, \tag{5.20}$$

the separating hyperplane $\mathbf{H}$ can be obtained by solving the following constrained quadratic optimization problem with $||\mathbf{w}||\rho = 1$:

$$\text{minimize} \quad Q(\mathbf{w}, b) = \frac{1}{2}||\mathbf{w}||^2, \tag{5.21}$$

$$\text{subject to} \quad y_k(< \mathbf{w}, \mathbf{x}_k > +b) \geq 1. \tag{5.22}$$

This is called the *primal* optimization problem. Introducing the Lagrangian, the optimization becomes

$$\text{minimize} \;\; L(\mathbf{w}, b, \lambda) = \frac{1}{2}||\mathbf{w}||^2 - \sum_{i=1}^{m} \lambda_i (y_i(< \mathbf{x}_i, \mathbf{w} > +b) - 1) \tag{5.23}$$

where λ_i are Lagrange multipliers. Since the quadratic equation is convex, this leads to

$$\frac{\partial}{\partial b} L(\mathbf{w}, b, \lambda) = 0 \quad \Rightarrow \quad \sum_{i=1}^{m} \lambda_i y_i = 0, \tag{5.24}$$

$$\frac{\partial}{\partial \mathbf{w}} L(\mathbf{w}, b, \lambda) = 0 \quad \Rightarrow \quad \mathbf{w} = \sum_{i=1}^{m} \lambda_i y_i \mathbf{x}_i.$$

at the optimum. The Karush-Kuhn-Tucker (KKT) theorem that asserts the existence of non-zero Lagrange multipliers (i.e., $\lambda_i > 0$) at the optimum (Bertsekas, 1999) leads to

$$\lambda_i(y_i(<\mathbf{x}_i, \mathbf{w}> +b) - 1) = 0 \tag{5.25}$$

The training vectors $\mathbf{x}_i$ with $\lambda_i > 0$ are called *Support Vectors* (SVs) located on the geometrical margins (i.e., $\mathbf{H}_1$ and $\mathbf{H}_2$), and the rest of the training vectors $\mathbf{x}_j$ are irrelevant to the optimization procedures because $\lambda_j = 0$. Substituting Equations 5.24 and 5.25 into Equation 5.23, the *dual* formation of the primal optimization problem can be obtained as

$$\begin{aligned}
\text{maximize} \quad & P(\lambda) = \sum_{i=1}^{m} \lambda_i - \frac{1}{2}\sum_{i,j=1}^{m} \lambda_i \lambda_j y_i y_j < \mathbf{x}_i, \mathbf{x}_j >, && (5.26)\\
\text{subject to} \quad & \lambda_i \geq 0 \ \ \forall\, i = 1, 2, \ldots, m, \quad \text{and} && (5.27)\\
& \sum_{i=1}^{m} \lambda_i y_i = 0.
\end{aligned}$$

Once the optimal λ_i's are found, the classification function can be solved as

$$f(\mathbf{x}) = \operatorname{sgn}\left(\sum_{i=1}^{m} \lambda_i y_i < \mathbf{x}, \mathbf{x}_i > +b\right) \tag{5.28}$$

When the training pattern vectors are not linearly separable, one can make H_1 and H_2 soft margin hyperplanes with so-called slack variables (ξ_i):

$$y_i(< x_i, w > +b) \geq 1 - \xi_i, \quad \text{where} \ \ \xi_i \geq 0 \ (i = 1, 2, \ldots, m). \tag{5.29}$$

Two approaches are commonly used for soft margin hyperplanes: the C-Support Vector Classification, and ν-Support Vector Classification. Cortes and Vapnik (1995) proposed a SV classifier by introducing slack variables and a penalty parameter C to the primal optimization function in Equation 5.22 as:

$$\begin{aligned} &\text{maximize} \quad Q(\mathbf{w}, \xi) = \frac{1}{2}||w||^2 + \frac{C}{m}\sum_{i=1}^{m}\xi_i, &(5.30)\\ &\text{subject to} \quad \xi_i \geq 0, \quad \text{and} &(5.31)\\ &\qquad\qquad y_i(< x_i, w > +b) \geq 1 - \xi_i, \quad \forall\, i = 1, 2, \ldots, m. \end{aligned}$$

This modified primal problem is called the C-Support Vector Classification (C-SVC). The dual form of the C-SVC is

$$\begin{aligned} &\text{maximize} \quad P(\lambda) = \sum_{i=1}^{m}\lambda_i - \frac{1}{2}\sum_{i,j=1}^{m}\lambda_i\lambda_j y_i y_j < \mathbf{x}_i, \mathbf{x}_j >, &(5.32)\\ &\text{subject to} \quad 0 \leq \lambda_i \leq \frac{C}{m} \quad \forall\;\, i = 1, 2, \ldots, m, \quad \text{and} &(5.33)\\ &\qquad\qquad \sum_{i=1}^{m}\lambda_i y_i = 0. \end{aligned}$$

The penalty parameter C determines the trade-off between maximizing the geometrical margin and minimizing the training error. One practical drawback of the C-SVC is that there is no guidelines to choose a reasonable value of C, because C is rather unintuitive. In order to address this problem, Schölkopf et al. (2000) proposed the ν-Support Vector Classification (ν-SVC) replacing C with another parameter ν as:

$$\text{maximize} \quad Q(\mathbf{w}, \xi) = \frac{1}{2}||w||^2 - \nu\rho + \frac{1}{m}\sum_{i=1}^{m}\xi_i, \tag{5.34}$$

$$\text{subjected to} \quad \xi_i \geq 0, \quad \rho \geq 0, \quad \text{and} \tag{5.35}$$

$$y_i(< x_i, w > +b) \geq \rho - \xi_i, \quad \forall\, i = 1, 2, \ldots, m.$$

The dual form of the ν-SVC is

$$\text{maximize} \quad P(\lambda) = -\frac{1}{2}\sum_{i,j=1}^{m}\lambda_i\lambda_j y_i y_j < \mathbf{x}_i, \mathbf{x}_j >, \tag{5.36}$$

$$\text{subject to} \quad 0 \leq \lambda_i \leq \frac{1}{m} \quad \forall\; i = 1, 2, \ldots, m, \tag{5.37}$$

$$\sum_{i=1}^{m}\lambda_i y_i = 0, \quad \text{and}$$

$$\sum_{i=1}^{m}\lambda_i \geq \nu.$$

So far, the training pattern vectors have been assumed to be linearly separable, and the SVC algorithm can be extended to the nonlinear classification using so-called *kernel-trick* technique. Using a kernel function Φ, the training vectors $\mathbf{x}_1, \mathbf{x}_2, \ldots, \mathbf{x}_m \in \mathcal{H}$ are nonlinearly transformed into a higher feature space, and the linear SVC is performed in the higher order space. Cover (1965) found the relationship between the number of possible linear separations and m numbers of training vectors in general position in an N-dimensional space. The number of possible linear separation is

$$2^m \qquad \text{when} \;\; m \leq (N+1) \tag{5.38}$$

and

$$2\sum_{i=0}^{N}\begin{pmatrix} m-1 \\ i \end{pmatrix} \qquad \text{when } \; m > (N+1) \tag{5.39}$$

Consequently, since $m > N+1$ in this study, the more N increases, the larger the number of possible linear separation that exists. However, in Cover's theory, the training vectors are required to be in a general position. Schölkopf and Smola (2002) pointed out that the Cover's theory "*does not strictly make a statement about the separability of a given data set in a given feature space. E.g., the feature map might be such that all points lie on a rather restrictive lower-dimensional manifold, which could prevent us from finding points in general position.*" This issue becomes very important in the classification of the reduced-order model, and more detailed discussion will be provided later in this section with actual experimental results from the MR damper. Solving the dual form of the optimization using the kernel-trick approach, the classification decision function in Equation 5.28 can be converted to

$$f(\mathbf{x}) = \text{sgn}\left(\sum_{i=1}^{m} y_i\lambda_i < \Phi(\mathbf{x}), \Phi(\mathbf{x}_i) >\right), \tag{5.40}$$

and then solving the dual form of the quadratic optimization function with kernel for separable training vector (refer Equation 5.28) as

$$\text{maximize} \quad P(\lambda) = \sum_{i=1}^{m}\lambda_i - \frac{1}{2}\sum_{i,j=1}^{m}\lambda_i\lambda_j y_i y_j < \Phi(\mathbf{x}_i), \Phi(\mathbf{x}_j) >, \tag{5.41}$$

$$\text{subject to} \quad \lambda_i \geq 0 \;\; \forall\, i = 1, 2, \ldots, m, \quad \text{and} \tag{5.42}$$

$$\sum_{i=1}^{m}\lambda_i y_i = 0.$$

Four kernel functions are commonly used in the SVC:

$$\text{Linear classifiers} \quad : \quad <\mathbf{x}, \mathbf{x}_i> \tag{5.43}$$

$$\text{Polynomial classifiers of order } d \quad : \quad <\mathbf{x}, \mathbf{x}_i>^d \tag{5.44}$$

$$\text{Radial basis function classifiers} \quad : \quad \exp(-||\mathbf{x} - \mathbf{x}_i||^2/\gamma) \tag{5.45}$$

$$\text{Sigmoid neural networks classifiers} \quad : \quad \tanh(\alpha <\mathbf{x}, \mathbf{x}_i> +\beta) \tag{5.46}$$

Classifier model selection for the MR damper change detection

A supervised change detection was performed using the C-SV radial basis function classifier (Equations 5.32, 5.33 and 5.45) to monitor the changes of the MR damper using the orthogonal Chebyshev coefficients ($\bar{C}_{ij}$) and non-orthogonal power series coefficients ($\bar{a}_{ij}$). In order to find the optimal parameters C and γ, a grid search method (Fan et al., 2005; Hsu et al., 2007) was used within the ranges of $2^{-9} \leq C \leq 2^{15}$ and $2^{-15} \leq \gamma \leq 2^5$. The SV classifier was trained using the data sets of $\bar{C}_{ij}$ and $\bar{a}_{ij}$. The cross-validation of 5-folds was used for the model selection of the SV classifier with the training data sets consisting of (441 features) $\times$ (2000 observations).

The classifier model selection was performed using the 3-fold cross validation of the training data sets for different C and γ. Figure 5.12 (a) shows the classification precisions for the $\bar{C}_{ij}$, and Figure 5.12 (b) for the $\bar{a}_{ij}$. From the grid search with 3-fold cross validation, the optimal values of the C and γ were found: $C_{\text{opt}} = 8192$ and $\gamma_{\text{opt}} = 3.91 \times 10^{-3}$ for the orthogonal Chebyshev coefficients, and $C_{\text{opt}} = 2.0$ and $\gamma_{\text{opt}} = 1.95 \times 10^{-3}$ for the non-orthogonal power-series coefficients.

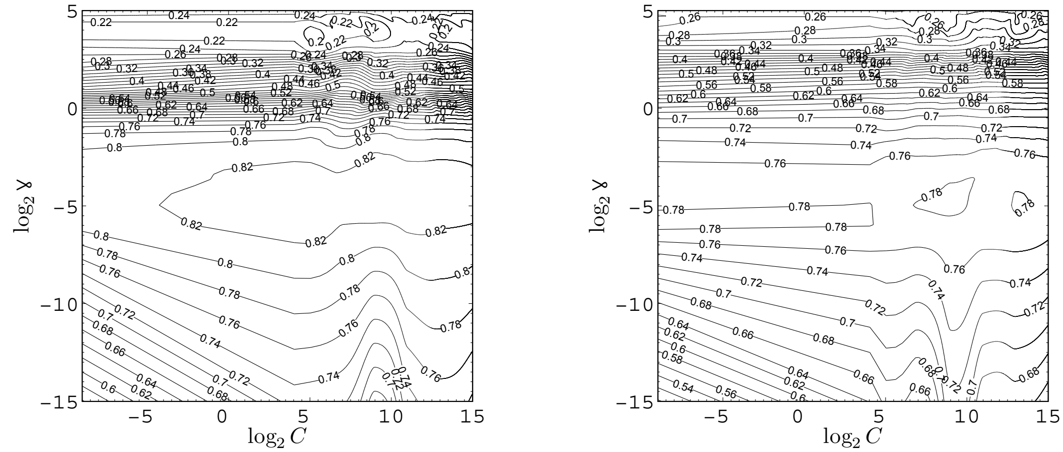

(a) Chebyshev coefficients

(b) Power series coefficients

Figure 5.12: The classification precision of C-Support Vector Classification for different C and γ values. The contours show the classification precision for different parameter values of C and γ.

Classifier precision assessments for the MR damper change detection

Once the SV classifier model was selected with the optimal C and γ for the $\bar{C}_{ij}$ and $\bar{a}_{ij}$, the classification precision was assessed using 50% of the data for training and 50% of the data for the precision assessment. In order to understand the model-order reduction effects, the number of features (m) in the classifications increased from one to 441 for the $O(20)$ models, and the corresponding classification precisions were measured. For $1 \leq m \leq 5$, the five most significant terms were determined using Equation 5.8, and the coefficients were used in the classification cumulatively in the order of the $\bar{C}_{01}$, $\bar{C}_{01}$, $\bar{C}_{10}$, $\bar{C}_{03}$, $\bar{C}_{30}$ and $\bar{C}_{34}$, and the same terms and order of the $\bar{a}_{ij}$.

Effects of model order reduction on the classification results

Figure 5.13 shows the classification precisions with the unbiased $\bar{C}_{ij}$ and the biased $\bar{a}_{ij}$ for different number of features. In the figure, the classification precisions for the data sets of $\sigma_I = 0.1$ A ($\bigcirc$) and $\sigma_I = 0.15$ A ($\triangle$) are also compared. Figures 5.13 (a) and (b) illustrate that

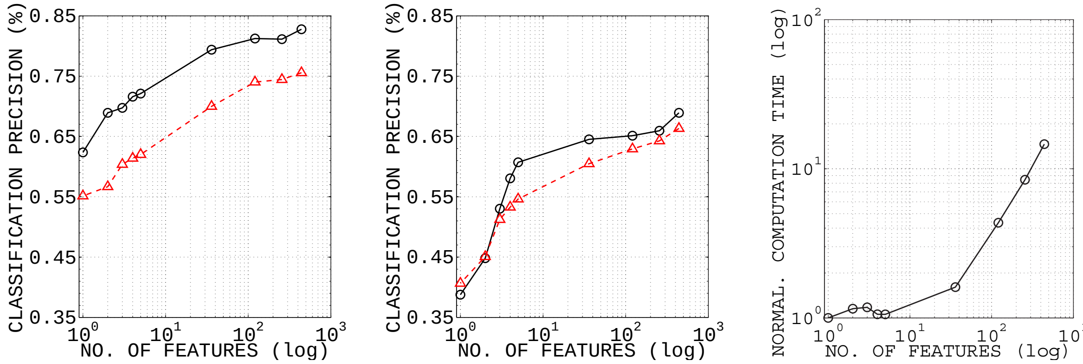

(a) Orthogonal ($\bar{C}_{ij}$) (b) Non-orthogonal ($\bar{a}_{ij}$) (c) Normalized comput. time

Figure 5.13: The precisions of the Support Vector Classification (SVC) for the statistically independent Chebyshev coefficients ($\bar{C}_{ij}$) and statistically correlated power-series coefficients ($\bar{a}_{ij}$). The SVC was performed for different number of features (i.e., identified coefficients) to study the effects of model-order reduction. Two different standard deviations of the MR damper input current (σ_I) of 0.1 A (◯) and 0.15 A (△) are compared for each type of coefficients. The computation times, normalized with respect to the smallest time, are also shown in the figure.

the classification precision increases as m increases for both $\bar{C}_{ij}$ and $\bar{a}_{ij}$. The semi-log plots also show that the precision improvement becomes saturated for a large m. In the figures, the precisions with the $\bar{C}_{ij}$ are larger than those with the $\bar{a}_{ij}$. For different system uncertainty levels, the precisions with $\sigma_I = 0.1$ A are greater than those with $\sigma_I = 0.15$ A. Figure 5.13 (c) shows the computation times, normalized with respect to the smallest time, for different m. The computation time with 441 features is about 15 times larger than with one feature. The classification results in Figure 5.13 is also summarized in Table 5.4.

The above results indicate that the classification with the unbiased $\bar{C}_{ij}$ is more efficient than with the statistically biased $\bar{a}_{ij}$ due to many advantageous properties of the orthogonal basis functions discussed in Sections 5.3.3 and 5.3.4. For the change detection in the MR damper, with the unbiased $\bar{C}_{ij}$, using reduced-order models would be more efficient, especially when a short computation time is a critical concern. For example, in order to improve the classification

Table 5.4: The precision of the Support Vector Classification (SVC) procedure for the statistically independent Chebyshev coefficients ($\bar{C}_{ij}$) and the statistically correlated power series coefficients ($\bar{a}_{ij}$). The SVC was performed for different number of features (i.e., identified coefficients) to study the effects of model-order reduction. Two different standard deviations of the MR damper input current (σ_I) of 0.1 A (◯) and 0.15 A (△) are compared for each type of coefficients. The computation times, normalized with respect to the smallest time, are also summarized in the table.

Number of classes	Number of features	0.1 A (%)		0.15 A (%)		Normalized computation time
		$\bar{C}_{ij}$	$\bar{a}_{ij}$	$\bar{C}_{ij}$	$\bar{a}_{ij}$	
4	1	62.4	38.8	55.1	40.7	1.0
	2	68.9	44.8	56.7	45.1	1.2
	3	69.7	53.0	60.4	51.2	1.2
	4	71.6	58.1	61.4	53.3	1.1
	5	72.1	60.7	62.0	54.6	1.1
	36	79.4	64.5	70.0	60.5	1.6
	121	81.2	65.1	74.0	62.9	4.3
	256	81.1	65.9	74.4	64.3	8.4
	441	82.8	68.9	75.6	66.3	14.6

precision from 80% to 85% for $\sigma_I = 0.1$ A, the m should be increased from 36 to 441 (Figure 5.13 (a)). However, the corresponding computation time increases approximately nine times (Figure 5.13 (c)). In the comparison of data sets with $\sigma_I = 0.1$ A and $\sigma_I = 0.15$ A, because the classification precision is inversely proportional to the system uncertainty, the classification with higher system uncertainty should involve more features in order to have the same precision as with a smaller system uncertainty.

Error analysis of the SV classication

In general, there exist two sources of classification error: Type I and Type II errors (Hogg and Tanis, 1997; Mendenhall and Sincich, 1995). For a given null hypothesis ($\mathbf{H}_0$), *Type I error* is defined as $\mathbf{H}_0$ is rejected when $\mathbf{H}_0$ is true. For the same $\mathbf{H}_0$, *Type II error* is defined as $\mathbf{H}_0$ is

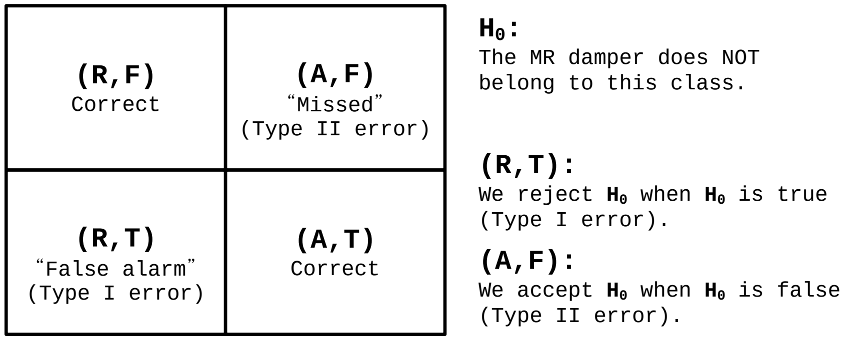

Figure 5.14: Detection rules with two sources of errors (Type I and Type II errors).

accepted when $\mathbf{H}_0$ is false. In this study, the $\mathbf{H}_0$ and its alternative hypothesis ($\mathbf{H}_a$) for each class are defined as (Figure 5.14)

$$\mathbf{H}_0 \;:\; \text{The MR damper does NOT belong to this class.} \tag{5.47}$$

$$\mathbf{H}_\mathrm{a} \;:\; \text{The MR damper belongs to this class.} \tag{5.48}$$

Consequently, in this study, Type I error is of a “false-alarmed” error, while Type II error is of a “missed-classification” error. The power of a test (or probability of detection) is defined as the probability of rejecting $\mathbf{H}_0$ when $\mathbf{H}_\mathrm{a}$ is true. The power of test can be expressed as

$$\text{Power of test} = 1 - p(\text{Type II error}), \tag{5.49}$$

where $p(\text{Type II error})$ is the probability of Type II error. Therefore, the power of test is the probability that the test will declare $\mathbf{H}_\mathrm{a}$ true when in fact $\mathbf{H}_\mathrm{a}$ is true.

Using those definitions, the Type I and Type II errors of the SVC for the $\bar{C}_{ij}$ were assessed. The probabilities of the apparent successful classification (correct), Type I error (false-alarm), Type II error (missed) and the power of test for each class are shown in Figure 5.15. The probabilities were measured for different m, so that the effects of model-order reduction on the classification precisions and errors can be understood.

In Figure 5.15 (a), the probabilities of the apparent successful classification were measured with the number of observations that belong to `(R,F)` and `(A,T)` in Figure 5.14 divided by total number of observations for different m. The highest probability of apparent successful classification is observed with Class D_1 ($\times$), and the lowest with Class B_1 ($\triangle$) (refer Table 5.1 for the class labels).

The probabilities of the Type I and Type II errors were measured with the number of observations that belong to `(R,T)` and `(A,F)`, respectively, divided by the total number of observations (Figures 5.15 (b) and (c)). For both Type I and Type II errors, the highest error probabilities are observed with Class B_1 ($\triangle$), and the lowest error probabilities with Class D_1 ($\times$). This result indicates that the classifier performance varies with different types of classes. The probabilities of both Type I and Type II errors decrease as m increases. In Figures 5.15 (b) and (c), it is also observed that there exist trade-offs between Type I and Type II errors for all classes. That is, if the Type I error decreases, the Type II error increases, and *vice versa*. Between these trade-offs, minimizing the Type II error would be more appropriate for the purpose of the SHM. For example, let us assume that there occurs significant damage in a monitored system. In the damage detection of the system, the chances of "false alarms" of the change detection increase with a larger Type I error. In this case, although the performance of the classifier becomes worse, having "false alarms" is more conservative to prevent the failure of the system. On the other hand, the chances of "missed" damage detection increases with a larger Type II error. In this case,

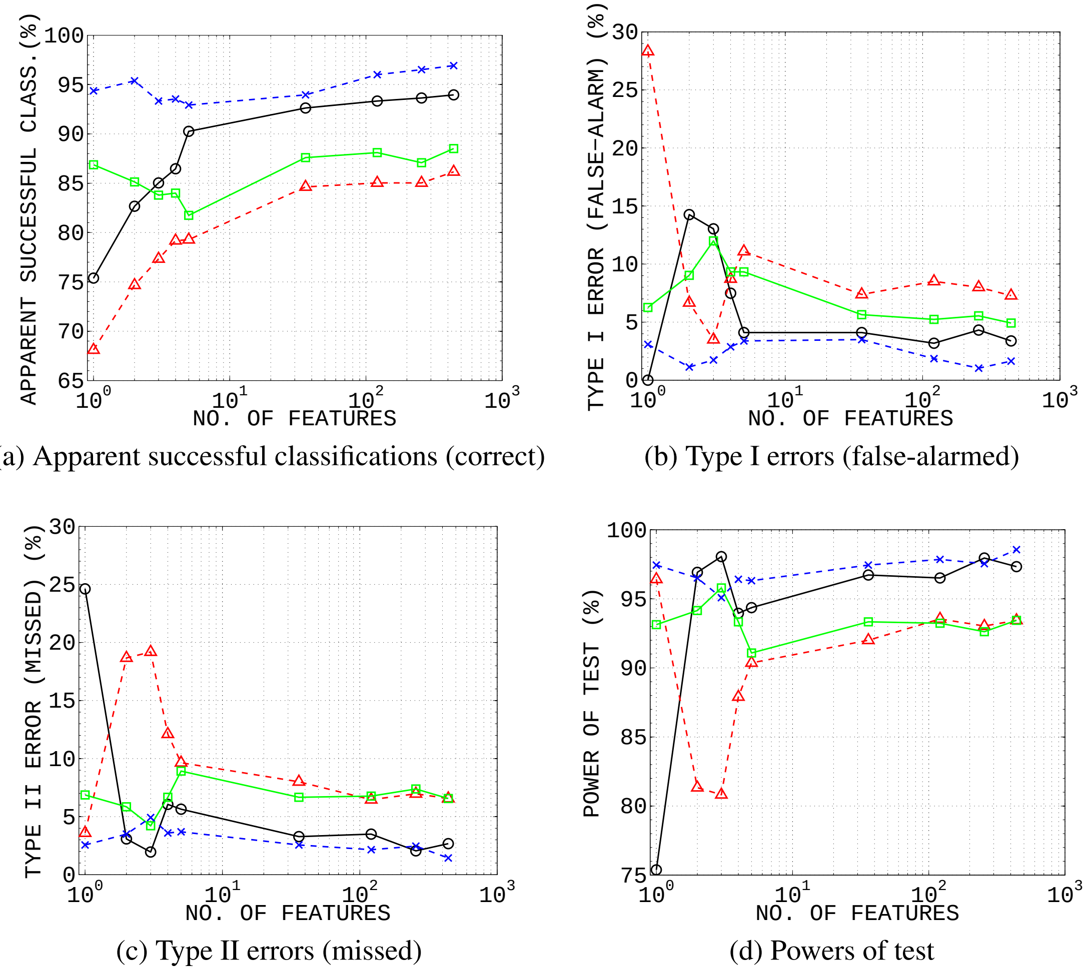

(a) Apparent successful classifications (correct)

(b) Type I errors (false-alarmed)

(c) Type II errors (missed)

(d) Powers of test

Figure 5.15: The probabilities of apparent successful classification, Type I error, Type II error and the power of test of the Support Vector Classification (SVC) for different numbers of the normalized Chebyshev coefficients (features) in the classification. In the SVC, four classes of data are classified: Test no. A_1 ($\bigcirc$), B_1 ($\triangle$), C_1 ($\Box$) and D_1 ($\times$).

the monitored system could be in a dangerous condition as results of failing to detect serious structural damage. Figure 5.15 (d) shows the powers of test for different m. The powers of tests increase as m increases, especially when $m > 10$. Similar to the probabilities of the apparent successful classification, the largest power of test is observed with Class D_1 ($\times$), and the lowest with Class B_1 ($\triangle$).

Classifier design for the optimal number of features

Based on the above results, an optimal classifier design strategy can be proposed by minimizing the number of features in the identification subjected to chosen thresholds of the "false alarm" (or Type I error), "missed" (or Type II error) and computation time. Two simple design examples are shown below:

(i) Design specifications 1

- Powers of test $\leq 90\%$ (or Type II errors $\leq 10\%$),
- Type I errors $\leq 10\%$, and
- The normalized computation time ≤ 2.0

(ii) Design specifications 2

- Powers of test $\leq 90\%$ (or Type II errors $\leq 10\%$),
- Type I error $\leq 15\%$, and
- The normalized computation time ≤ 2.0

The figures necessary for these design examples can be found in Figure 5.15 (d) for the powers of test, in Figure 5.15 (c) for the Type I error, and Figure 5.13 (c) for the normalized computation time. The optimal number of features for the design examples is *36* for the specifications 1, and *5* for the specifications 2 (without the interpolations between different m).

5.4.3 Unsupervised Change Detection Using k-Means Clustering

Overview of the k-means clustering

The k-means clustering is an unsupervised algorithm to cluster the pattern vectors in a feature space into k partitions. With *a priori* information about the number of clusters (not desired class labels), the algorithm defines k centroids, and one for each cluster. For the given pattern vectors $\mathbf{x}_1, \mathbf{x}_2, \ldots, \mathbf{x}_m$ ($m \geq k$), let $\mathbf{c}_i$ be the geometrical centroid of the i^{th} cluster. Then, the k-means classifier can be expressed as the following optimization function:

$$\text{minimize} \quad J(\mathbf{c}_1, \mathbf{c}_2, \ldots, \mathbf{c}_k) = \sum_{i=1}^{k} \sum_{\mathbf{x}_j \in S_i} |\mathbf{x}_j - \mathbf{c}_i|^2 \tag{5.50}$$

where $S_i = \{\mathbf{x}|\ \mathbf{x}$ assigned in the i^{th} cluster$\}$. Simple procedures of the k-means clustering were proposed by MacQueen (1967):

1. Randomly generate k points as the initial centroids $\mathbf{c}_i$, where $i = 1, 2, \ldots, k$.
2. Assign $\mathbf{x}_j$ to the nearest cluster centroid, where $j = 1, 2, \ldots, m$.
3. Once all $\mathbf{x}$ are assigned to the centroids, recalculate the position of the centroids.
4. Repeat above two steps until the locations of the centroids are converged.

In general, however, the solution of Equation 5.50 is not necessarily lead to a global minimum (Bottou and Bengio, 1995; Mangasarian, 1997; Pollard, 1982; Selim and Ismail, 1984).

Classification results for the MR damper

A unsupervised change detection was performed using the k-mean clustering algorithm with the identified RFM coefficients. The distances between the centroid clusters are measured with the squared Euclidean distance. The maximum iteration of each clustering was set to be 5000. In order to avoid the local minimum problem discussed earlier, and the procedures were statistically averaged over 100 sets. The parameters of the k-mean clustering used are summarized in Table 5.5.

Table 5.5: Parameters for k-means clustering for the MR damper change detection.

Parameters	Values
Distance measurement	Squared Euclidean distance
Maximum iteration	5000
Number of statistical averagings	600

Table 5.6 summarizes the results of unsupervised k-mean clustering for the MR damper change detection. The table shows the powers of test (Equation 5.49) for different numbers of features (m) and classes (M). The power of test is also referred to as the probability of detection that declares that the MR damper belongs to a class ($\mathbf{H}_0$) when $\mathbf{H}_0$ is actually true. The results show that, unlike the SVC, there is no noticeable improvement of the powers of test with the k-means clustering by adding more features in the classification for both $\bar{C}_{ij}$ and $\bar{a}_{ij}$. However, the power of test is slightly larger with the $\bar{C}_{ij}$ than with the $\bar{a}_{ij}$ for approximately 9% on average.

Table 5.6: The results of k-means clustering for the MR damper change detection with different numbers of features and classes. The table shows powers of test (Equation 5.49) for each case.

Classes	No. of observations	Orthogonal ($\bar{C}_{ij}$) (%)			Non-orthogonal coefficients ($\bar{a}_{ij}$) (%)		
		2 features	5 features	441 features	2 features	5 features	441 features
A_1	1000	56.56	94.34	95.94	81.54	81.22	82.87
B_1		66.28	86.98	51.44	78.34	73.11	83.24
A_1	1500	96.95	97.09	70.34	81.15	80.11	86.56
B_1		88.50	88.43	90.85	79.90	73.39	88.50
C_1		85.72	85.03	94.46	82.74	71.31	66.87
A_1	2000	99.18	75.89	75.89	84.04	86.61	82.25
B_1		76.04	88.25	76.04	78.96	79.53	77.83
C_1		90.30	74.45	92.05	83.58	86.04	74.55
D_1		86.15	86.20	74.04	74.19	75.68	77.12
	Averages	82.85	86.30	80.12	80.49	78.56	79.98

5.5 Summary and Conclusion

An effective and reliable structural health monitoring methodology is proposed for change detection in uncertain nonlinear dynamic systems. An experimental study was performed using an MR damper to evaluate the range of validity of the proposed methodology. The experimental results demonstrated that the proposed methodology can successfully assess the conditions of uncertain nonlinear systems by: (1) detecting (small) genuine system changes, (2) interpreting physical meaning of the detected changes without *a priori* knowledge of system characteristics, and (3) quantifying the uncertainty bounds of the detected changes.

In the proposed methodology, the Restoring Force Method was used as a non-parametric system identification approach. It was demonstrated that the Restoring Force Method is more useful than other modeling approaches in structural health monitoring applications, taking advantage of features from both the parametric and non-parametric modeling approaches: the identification procedure is data-driven and some physical interpretation is possible, using the identified coefficients.

Supervised and unsupervised statistical classification methods were applied to detect genuine system changes with different levels of system uncertainty. The classification results demonstrated that the identified coefficients using the Restoring Force Method can be used as excellent features to detect system changes in uncertain nonlinear systems. With statistical unbiasness of the identified coefficients, it was shown that the change detection procedure can be dramatically simplified using reduced-order models.

Chapter 6

Monitoring the Collision of a Cargo Ship with the Vincent Thomas Bridge

6.1 Introduction

6.1.1 Motivation

The demand on advanced transportation infrastructure increases in every region of the world. In the United States and across the world, more highways and bridges are being built than in the past. With new construction technologies and materials to link lands and islands, bridges have become longer and more reliable. As more bridges have been constructed, however, the chances of collisions with ships have also increased. In fact, ship-bridge collisions (with potentially serious consequences) happen relatively frequently. Some examples of these, with fatalities, in different countries are shown in Table 6.1. In the United States, many significant ship-bridge collisions have occurred, and many of them involved human fatalities. Some major ship-bridge collision incidents in the United States, reported by National Transportation Safety Board (NTSB), are summarized in Table 6.2.

When a ship-bridge collision occurs, accurate and rapid condition assessment of the bridge is critical. Such an assessment should include the estimation of potential damage, as well as that of direct damage in order to prevent secondary disasters that could be induced by the collision.

Table 6.1: Examples of ship-bridge collisions with fatalities in different countries, listed in chronological order (Mastaglio, 1997; Proske and Curback, 2003).

Bridge name	Year	Fatalities
Severn River Railway Bridge, UK	1960	5
Lake Ponchartain, USA	1964	6
Sidney Lanier Bridge, USA	1972	10
Lake Ponchartain Bridge, USA	1974	3
Tasman Bridge, Australia	1975	15
Pass Manchac Bridge, USA	1976	1
Tjorn Bridge, Sweden	1980	8
Sunshine Skyway Bridge, USA	1980	35
Lorraine Pipeline Bridge, France	1982	7
Sentosa Aerial Tramway, China	1983	7
Volga River Railroad Bridge, Russia	1983	176
Claiborn Avenue Bridge, USA	1993	1
CSX/Amtrak Railroad Bridge, USA	2001	47
Port Isabel, USA	2001	8
Webber-Falls, USA	2002	12

Since current practices of damage estimation mainly rely on human visual inspections, accurate and reliable condition assessment of a target bridge is often infeasible, as damage may not be visible. In such a case, vibration-based structural health monitoring approaches can augment traditional damage inspection methods. Thanks to the multi-disciplinary advanced technologies of sensor networks, data acquisition, communication, computation powers and system identification techniques, this approach has the potential to provide a useful and reliable damage quantification, which might be difficult with traditional visual inspection approaches.

6.1.2 Objectives

This chapter presents a forensic study of the first-ever collision of a cargo ship with the Vincent Thomas Bridge (VTB), a critical 1850-m suspension bridge located in the larger metropolitan Los Angeles, California region.

Table 6.2: Examples of major ship-bridge collision incidents in the U.S.A. during the past 30 years reported by National Transportation Safety Board.

Date	Location	Accident description
1977-02-24	Hopewell, Virginia	U.S. Tankship SS Marine Floridan Collision with the Benjamin Harrison Memorial Bridge.
1978-04-01	Berwick Bay, Louisiana	Collision of M/V stud with the Southern Pacific Railroad Bridge over the Atchafalaya River.
1980-05-09	Tampa Bay, Florida	Ramming of the Sunshine Skyway Bridge by the Liberian bulk carrier Summit Venture.
1983-04-02	St. Louis, Missouri	Ramming of the Popular Street Bridge by the tow boat M/V City of Greenville and its four-barge tow.
1983-11-23	New Orleans, Louisiana	Collision of the Panamainia cement carrier M/V Amparo Paola with the Danziger Bridge Inner Harbor Nav. Canal.
1984-04-26	St. Louis, Missouri	Ramming of the Poplar Street Bridge by the towboat M/V Erin Marie and its twelve-barge tow.
1987-05-03	Brunswick, Georgia	Ramming of the Sidney Lanier Bridge by the Polish bulk carrier Ziemia Bialostocka.
1988-05-06	Chicago, Illinois	Ramming of the CSXT Railroad Bridge by the Cyprian Bulk carrier M/V Pontokratis Calumet River.
1993-05-28	New Orleans, Louisiana	U.S. Towboat Chris collision with the Judge William Seeber Bridge.
1998-04-04	St. Louis Harbor, Missouri	Ramming of the Eads Bridge by barges in tow of the Merchant/Motor Vessel (M/V) Anne Holly with subsequent ramming and near breakaway of the President Casino on the Admiral.
2002-05-26	Oklahoma	U.S. towboat Robert Y. Love allision with Interstate 40 Highway Bridge near Webbers Falls.

Using advanced structural health monitoring technologies, the main objective of this study was to demonstrate various analysis and interpretation capabilities of the bridge's global condition after the collision. The dynamic response of the VTB was successfully measured (with a real-time monitoring system installed on the bridge) before and after the incident, as well as during the impact process. Using these valuable data, various system identification approaches, including global (multi-sensor) and local (single-sensor) identification methods, were performed independently to detect the potential occurrence of significant changes in the bridge's vibration signature.

6.1.3 Scope

The contents of this chapter are organized as follows. The description of the VTB and its real-time monitoring system are presented in Section 6.2. The procedure for the preliminary data processing and its results are discussed in Section 6.3. In Section 6.4, detailed information and sensor measurements of the ship-bridge collision incident are presented. Various global and local identification approaches used in this study are explained, and their identification results are shown in Section 6.5. The summary and conclusions of the chapter are provided in Section 6.6.

6.2 Real-Time Monitoring of the Bridge

6.2.1 Bridge Description

The VTB is located in the metropolitan Los Angeles region. This bridge was one of toll bridges before 2000, and it is still considered as a major bridge in California. It connects two main harbors in this region, the Port of Los Angeles and the Port of Long Beach (See Figure 6.1). These two ports are among the busiest ports in the U.S. The bridge handles approximately 39000 cars and trucks daily. The VTB is a cable-suspension bridge, approximately 1850-m long, consisting of a main span of 457 m, two suspended side spans of 154 m each, and two ten-span cast-in-place concrete approaches of 545-m length on both ends. The roadway is 16-m wide and accommodates four lanes of traffic. The bridge was completed in 1964 with 92000 tons of Portland cement, 13000 tons of light weight concrete, 14100 tons of steel and 1270 tons of suspension cables. The bridge was designed to withstand winds of up to 145 kilometer per hour. A major seismic retrofit was performed during the period 1996-2000, including a variety of strengthening measures, and the incorporation of about 48 large-scale nonlinear passive viscous dampers.

(a) A photo of the Vincent Thomas Bridge (Courtesy of Port of Los Angeles). In the photo, the left is the East tower toward Terminal Island, and the right is the West tower toward San Pedro.

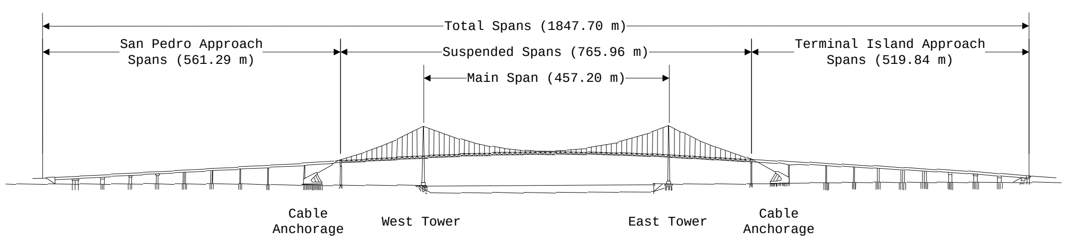

(b) A schematic view of the Vincent Thomas Bridge with span dimensions.

Figure 6.1: The Vincent Thomas Bridge.

6.2.2 VTB Instrumentation

The VTB has been instrumented by the California Strong Motion Instrumentation Program (CSMIP) of the California Geology Services (CGS), formerly known as the Division of Mines and Geology (CDMG), for more than twenty years. The strong-motion recording system consists of twenty-six accelerometers mounted on the bridge and an original analog recording system (later converted to a digital recording system) located in the east anchor block. Figure 6.2 shows the sensor locations for this system.

Significant motions have been recorded for the 1987 Whittier, 1994 Northridge, and several other earthquakes. Analysis of these recordings has provided much information about the dynamic response of large suspension bridges. The previous analog film recording system, (used until the mid 1990s) has proven to be very reliable, but the recorded data were limited in dynamic range and difficult to convert to digital format appropriate for computer analysis.

Modern digital recording technology certainly can provide superior data quality and ease of analysis. To demonstrate this, a temporary digital monitoring system with remote communications capability was installed in parallel with the existing analog recording system for the Vincent Thomas Bridge strong motion instrumentation between November 3 and December 5, 1995. During this short time period, a large amount of ambient vibration data was recorded. The capability of remote real-time data monitoring was also demonstrated.

Abdel-Ghaffar et al. (1995) includes examples of preliminary analysis in the appendices, showing these measurements and the large amount of high-quality digital data obtained during the monitoring period. Examples of preliminary analyses are included in the appendices. In

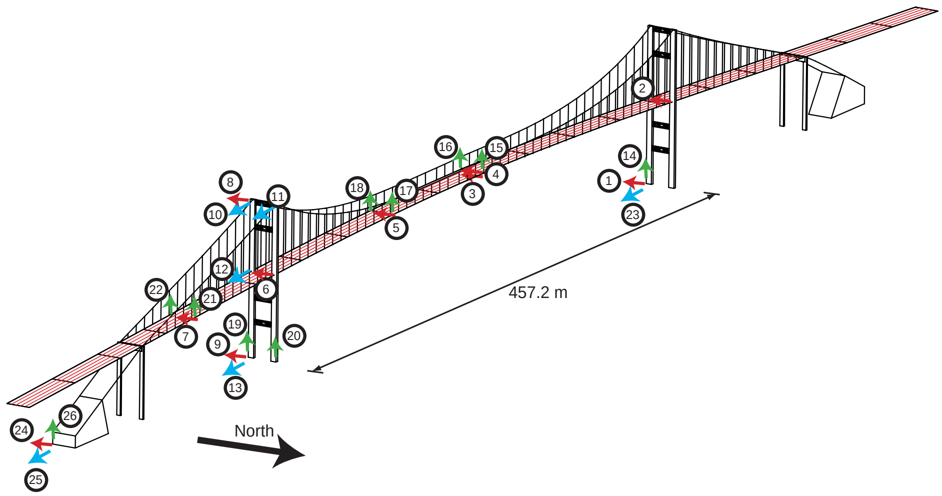

Figure 6.2: Sensor locations and directions on the Vincent Thomas Bridge, San Pedro, CA.

addition to successfully demonstrating this application of modern structural monitoring instrumentation, the recorded ambient vibration data provided a baseline for evaluating the effects of the seismic retrofit on the bridge's dynamic behavior, occurring from 1999 to 2000.

More information concerning instrumentation and analysis of the VTB can be found in Abdel-Ghaffar and Housner (1978); Abdel-Ghaffar et al. (1992); He et al. (2004); Ingham et al. (1997); Masri et al. (2004); Smyth et al. (2003); Wahbeh et al. (2003).

6.2.3 Real-time Bridge Monitoring System

The VTB has been monitored with a web-based real-time bridge monitoring system developed by the authors since 2005 (Wahbeh et al., 2005). The monitoring system consists of four subsystems, including: (1) sensor networks; (2) publisher; (3) server; and (4) clients (see Figure 6.3).

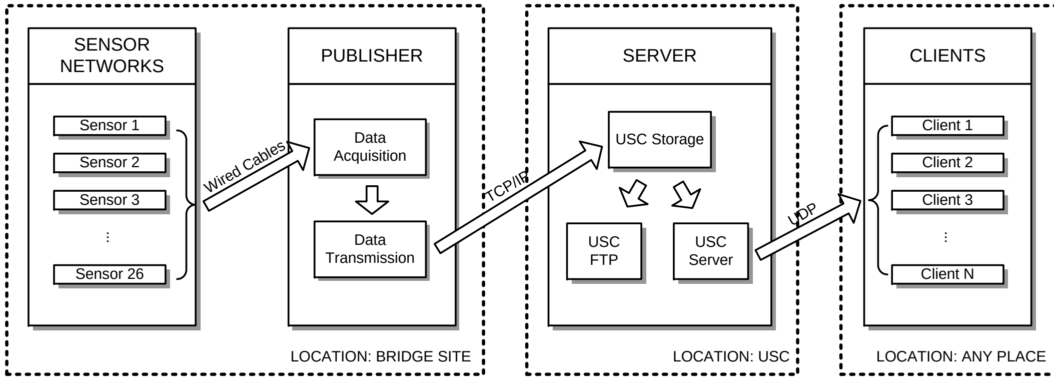

Figure 6.3: A schematic of the VTB real-time monitoring system architecture.

1. For the sensor network subsystem, twenty-six strong-motion accelerometers are used to measure the bridge's ambient and earthquake vibrations. The sensor locations and measurement directions are illustrated in Figure 6.2. Notice that the eastern half of the bridge is more densely instrumented than the western half, because the data acquisition system is housed in the eastern cable anchorage.

2. Bridge motion is sensed by the accelerometers, then the sensor signals are conveyed to the publisher subsystem, which consists of the data acquisition module and data transmission module. The accelerometers are physically connected to the data acquisition module with wire cables, and the sensor signals are sampled at 100 Hz.

3. Using the data transmission module, the digitized signals are transmitted to the server subsystem accessed via the Internet. The TCP/IP protocol is used for reliable data communication between the publisher and server subsystems (Stevens, 1998; Stevens et al., 2002).

4. The acquired data can be downloaded using the FTP server located in the University of Southern California (USC), the USC FTP module, for further analysis. The data are also

sent to the USC server module to distribute the data simultaneously to multiple authorized clients, such as CDMG and Caltrans.

5. In the server-to-multiclient communication, the data transmition rate often becomes a "bottle-neck" for successful data communication. Therefore, a faster and less reliable communication protocol , UDP, is used (Stevens, 1998; Stevens et al., 2002).

6.3 Preliminary Data Processing

Once the bridge accelerations were measured, the raw data were processed to obtain the corresponding velocities and displacements using the following procedure:

1. The DC and linear trend were subtracted from the raw accelerations, and a cosine-tapered window was applied to the acceleration time histories to prevent frequency leakage.

2. A bandpass filter was designed with the cutoff frequencies of 0.1 to 30 Hz and applied to the acceleration time histories.

3. Standard numerical integration procedures were subsequently used to obtain the corresponding velocity and displacement time histories.

A sample processed acceleration and displacement time history record at the moment of the cargo-ship collision is shown in Figure 6.4.

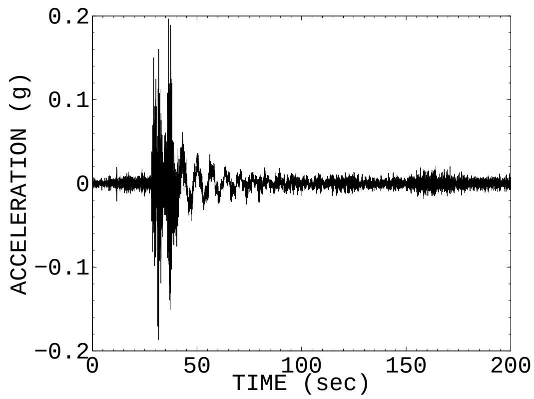

(a) Processed acceleration

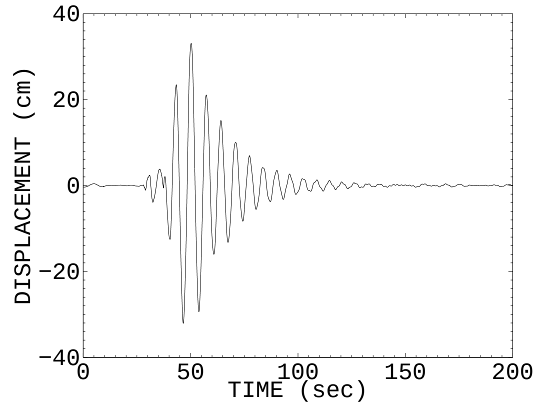

(b) Processed displacement

Figure 6.4: Preprocessed acceleration and displacement of Channel 4 (lateral direction at the mid-span of the bridge deck). The acceleration was numerically double-integrated to obtain the displacement with the cutoff frequencies of 0.1 to 30 Hz.

6.4 Description of the Ship Collision Incident

6.4.1 Factual Information of the Incident

The *Beautiful Queen* is a 189-m (620-ft) 32000-ton cargo ship, owned by Pasha Hawaii Transportation Line. The cargo ship is a bulk carrier, not a container ship, commonly hauling rolled steel, coal or grain. The ship is equipped with onboard cranes for freight loading.

On Sunday, 27 August 2006, the ship departed from the Los Angeles harbor via one of the channels in the harbor district. At 16:40 (Pacific Daylight Time), the ship was passing under the Vincent Thomas Bridge, linking San Pedro and Terminal Island as shown in Figure 6.5. When the ship was passing under the bridge, the ship operators miscalculated the tide, and one of the onboard cranes scraped a guide rail of a maintenance scaffold secured at the bridge center span, which was about 56 m (185 ft) above water. No injuries were reported during the incident. A schematic view of the ship-bridge collision is illustrated in Figure 6.6, and the damaged guide rail of the maintenance scaffold is shown in Figure 6.7.

Figure 6.5: Schematic view of the incident area (courtesy of Google Inc.)

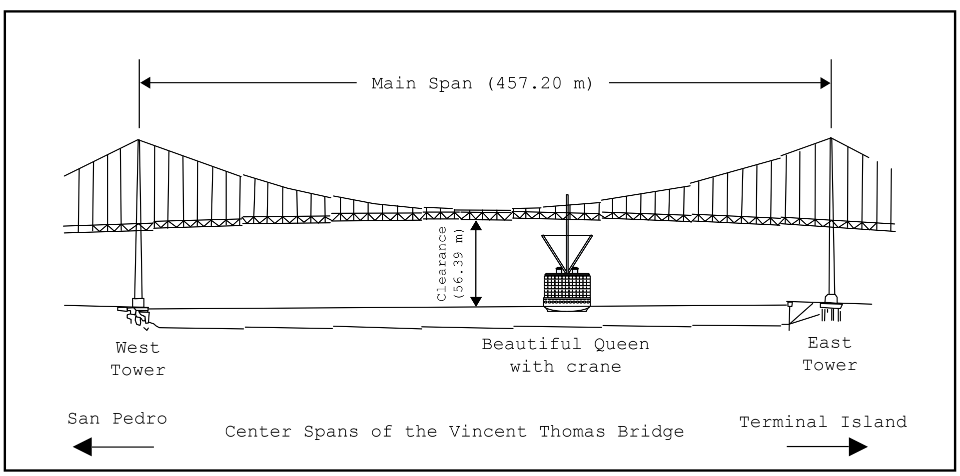

Figure 6.6: Schematic view of *the Beautiful Queen*, a cargo ship, under the Vincent Thomas Bridge. The figure is presented for illustration purpose, and does not show the actual path taken by the ship during the collision.

About thirty minutes after the collision, the vehicular traffic across the bridge was stopped by Caltrans to investigate potential damage. Vessel traffic was also stopped under the bridge by the Los Angeles Port Police and Coast Guard. Two incoming cargo ships were delayed due to the vessel traffic shut-down. After investigating the incident for a period of about two hours, Caltrans engineers declared that the bridge was sound and that the damage was limited to the maintenance scaffolding. Both vehicle and vessel traffic were re-opened at 18:55 the same day. An independent investigation was also conducted by the Coast Guard on the colliding cargo ship.

6.4.2 Vibration Monitoring of the Incident

The VTB vibration during the cargo-ship incident, and two-hour traffic shut-down afterward, were successfully captured by the real-time monitoring system. Sample acceleration time history data are illustrated in Figure 6.8. The figure shows a time-window of 24-hours (from midnight to midnight) corresponding to the displacement measurements at the mid-span of the bridge deck (Figure 6.8 (a)) and at the east column (Figure 6.8 (b)) in the lateral and vertical directions. According to the measurements, the incident occurred at 16:41 and resulted in approximately two minutes of superstructure vibration. At 17:12, thirty-one minutes after the incident, the displacement RMS reduced dramatically for a 1:45 hour duration, corresponding to the post-incident traffic shut-down by Caltrans. The impact by the cargo-ship was more noticeable in the lateral displacements than in the vertical displacements, for both the bridge deck and columns, since the bridge was rammed by the ship in the lateral direction.

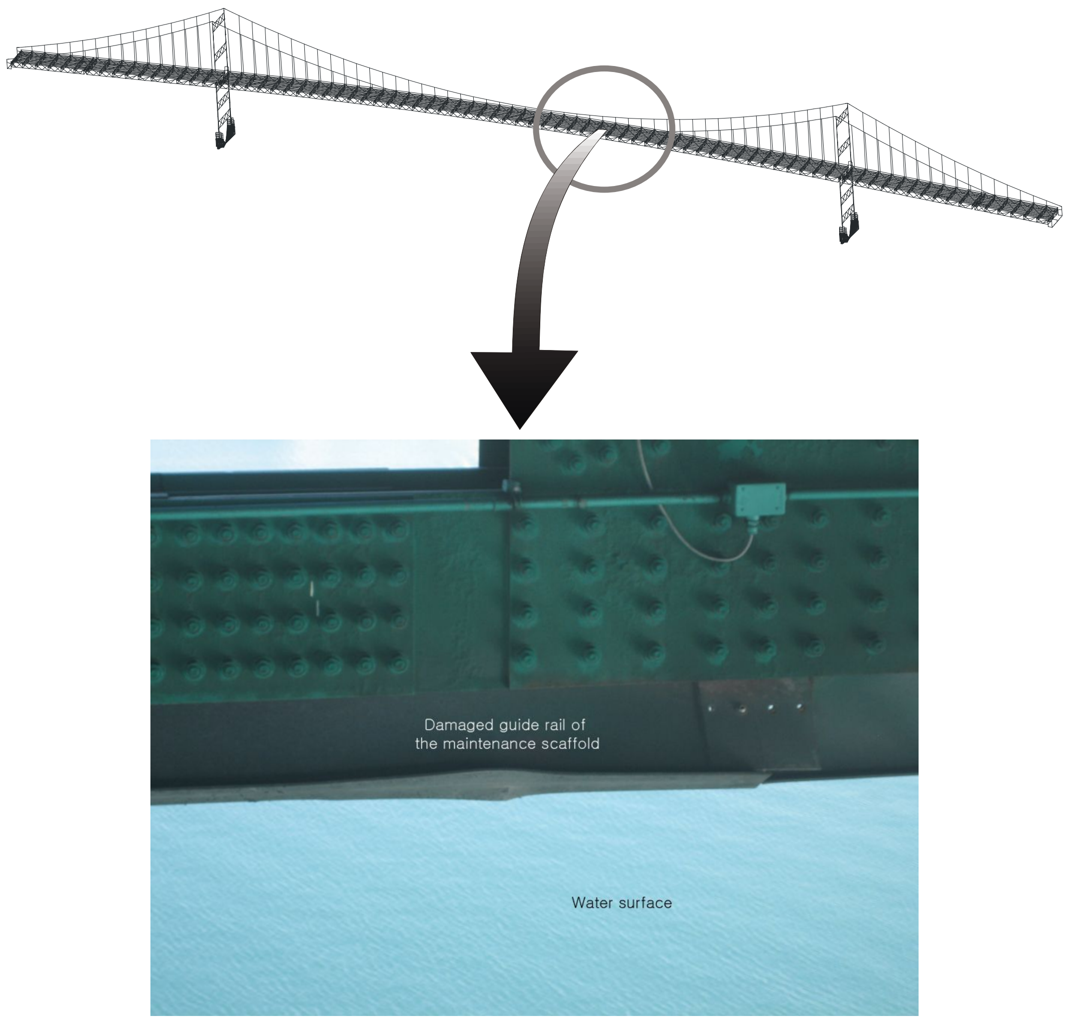

Figure 6.7: A damaged maintenance scaffolding member from the ship-bridge collision (Courtesy of Caltrans). This figure is presented for illustration purpose. The location of the damaged member in the bridge could differ from the exact location.

6.4.3 Bridge Response Before and After the Incident

The bridge response is largely influenced by various environmental conditions, such as traffic intensity and temperature, and the bridge characteristics determined with identification methods could be also affected by these conditions. Therefore, it is worthy to investigate the trends of the bridge response over certain periods.

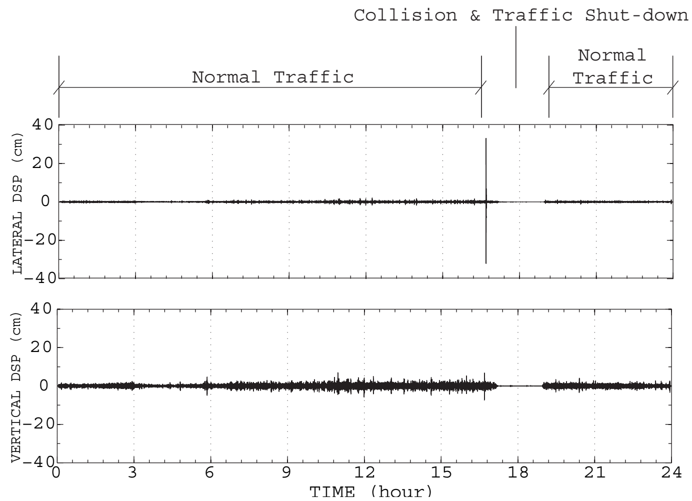

(a) Displacements at the mid-span of the bridge deck — Channel 3 (top) and Channel 16 (bottom).

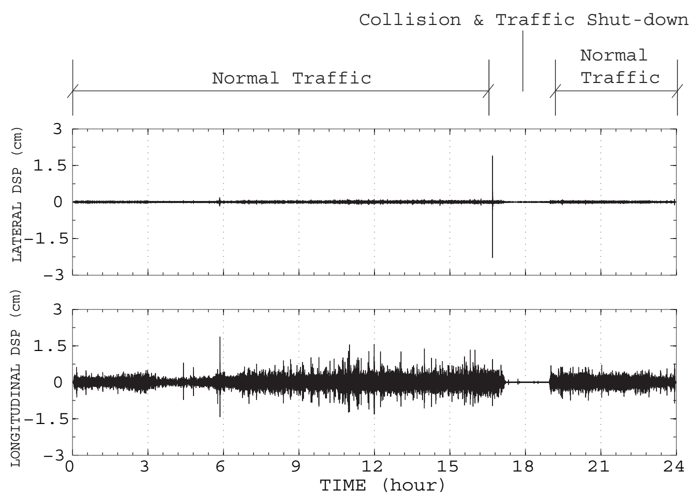

(b) Displacements at the top of the bridge column — Channel 8 (top) and Channel 10 (bottom).

Figure 6.8: Displacements of the bridge deck and column on 27 August 2006 when the cargo-ship incident occurred. The top figure shows the lateral displacement, and the bottom figure shows the vertical direction.

Typical weekly RMS displacements of the main span of the bridge deck before and after the incident are shown in Figure 6.9. In the figure, $\circ$ indicates an hourly RMS displacement, and $\triangle$ indicates a daily average of the hourly RMS displacements. One standard deviation (σ) of the hourly RMS displacements for one day is shown as the gray region in the figure. The RMS levels of the displacement during the incident impact and traffic shut-down after the incident were also determined and shown as a dash line and dash-dot line, respectively. The figure shows that no significant difference was observed in the bridge response before and after the incident. For the vertical displacement, the hourly RMS displacement is less than 2.5 cm during the particular weeks before and after the incident (Figures 6.9 (a) and (c)). A daily cycle was observed for a week starting on Monday and ending Sunday – smaller displacements were noted at night and larger displacements during the day due to traffic. It is also shown that the daily average of the hourly RMS displacement is relatively high during weekdays, while much lower during weekends. Similar trends were found in the lateral displacements (Figures 6.9 (b) and (d)), while its amplitude is about one third of the vertical displacements before and after the incident.

6.5 System Identification of the Bridge

6.5.1 Global System Identification Approaches

This section deals with the basic formulation of the Natural Excitation Technique (NExT) in conjunction with the Eigensystem Realization Algorithm (ERA), which was used to extract the modal parameter information of the VTB. For more detailed formulation and discussion, the reader is referred to other papers by the authors (Nayeri et al., 2007, 2006).

Formulation of the time-domain modal parameter identification techniques

Providing known input excitations for large civil structures is very difficult, costly, and in many cases infeasible. On the other hand, ambient excitation (from wind, traffic, ground motion, etc.) is always available. However, ambient vibrations are output-only, as the inputs cannot be measured or quantified with any certainty. These facts show the importance of output-only modal

BEFORE ACCIDENT

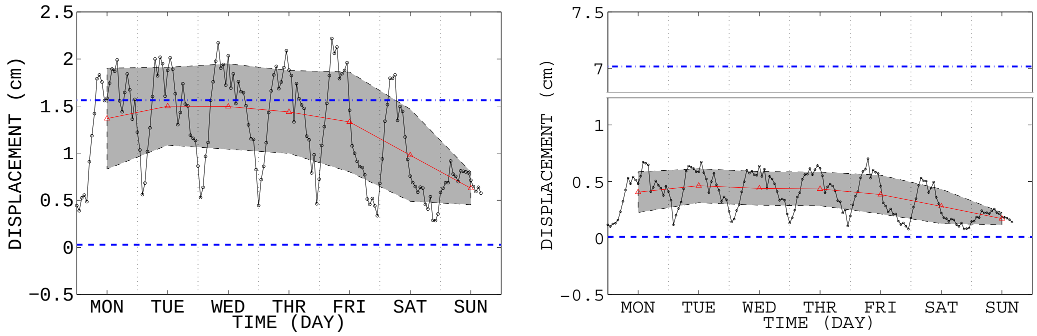

(a) Vertical displacement (sensor 15) (b) Lateral displacement (sensor 3)

AFTER ACCIDENT

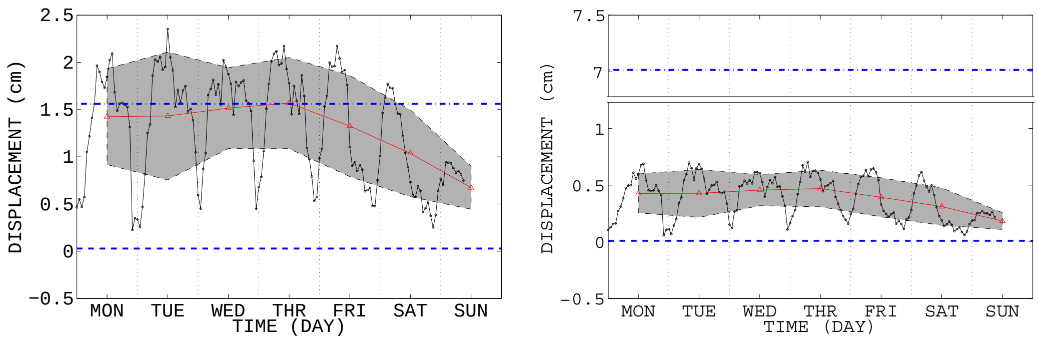

(c) Vertical displacement (sensor 15) (d) Lateral displacement (sensor 3)

Figure 6.9: Typical weekly root-mean-square (RMS) displacements of the main span of the bridge deck in vertical and lateral directions before and after the ship-bridge collision. In the figure, ○ indicates an hourly RMS displacement, and △ indicates a daily average of the hourly RMS displacements. One standard deviation (1σ) of the hourly RMS displacements for one day is shown as the gray region in the figure. The RMS levels of the displacement during the incident impact and traffic shut-down after the incident were also determined and shown as a dash line and dash-dot line, respectively.

parameter identification methods. The NExT approach, introduced by James et al. (1993, 1996), has been successfully used for the identification of structures based on output-only information (Caicedo et al., 2004). The basic idea behind the NExT method is that the cross-correlation function between the response vector and the response of a selected reference DOF satisfies the homogeneous equation of motion, provided the excitation and responses are weakly stationary random processes. Weak stationarity can usually be assumed for ambient vibrations over typical analysis time durations of minutes to tens of minutes.

Using NExT, it can be also shown that the cross correlation function between the acceleration process vector and the acceleration of a reference DOF satisfies the homogeneous (or free vibration) equation of motion per the equation:

$$\mathcal{M}\ddot{\mathbf{R}}_{\ddot{X}_{ref}\ddot{X}}(\tau) + \mathcal{D}\dot{\mathbf{R}}_{\ddot{X}_{ref}\ddot{X}}(\tau) + \mathcal{K}\mathbf{R}_{\ddot{X}_{ref}\ddot{X}}(\tau) = \mathbf{0} \tag{6.1}$$

where $\ddot{X}$ and $\ddot{X}_{ref}$ are the $n \times 1$ acceleration vector, and the reference DOF acceleration, respectively, $\mathcal{M}$, $\mathcal{D}$, and $\mathcal{K}$ are the $n \times n$ mass, damping, and stiffness matrices respectively, and $\mathbf{R}(.)$ denotes the correlation function.

Previous experience (Nayeri et al., 2006) has shown that one cannot rely one a single reference DOF for identification of all modes. Optimum accuracy for different modes typically occurs at different choices of the reference DOFs. The importance of Equation (6.1) is that: (a) the stationary random excitation (ambient noise) is eliminated from the equation of motion, and (b) only the acceleration records are needed to implement the technique.

Once the homogeneous equation of motion is formed using the NExT, the ERA (Juang and Pappa, 1985, 1986) can be used to extract the modal parameters of the homogeneous model.

Here, we briefly present the fundamental principles of ERA. The first fundamental step is to form the $n(r+1) \times m(p+1)$ Hankel block data matrix as follows:

$$\mathbf{H}(k-1) = \begin{bmatrix} \mathbf{Y}(k) & \mathbf{Y}(k+1) & \dots & \mathbf{Y}(k+p) \\ \mathbf{Y}(k+1) & \mathbf{Y}(k+2) & \dots & \mathbf{Y}(k+p+1) \\ \vdots & \vdots & \ddots & \vdots \\ \mathbf{Y}(k+r) & \mathbf{Y}(k+r+1) & \dots & \mathbf{Y}(k+p+r) \end{bmatrix} \tag{6.2}$$

where n and m are the number of measurement stations, and the reference DOFs, respectively; r and p are integers corresponding to the number of block rows and columns, respectively. $\mathbf{Y}(k)$ is the $n \times m$ matrix of the cross-correlation functions which satisfies the homogeneous equation of motion (Equation 6.1). The ERA process starts with factorization of the Hankel block data matrix, for $k = 1$, using the singular value decomposition procedure:

$$\mathbf{H}(0) = \mathbf{P}\mathbf{D}\mathbf{Q}^T = \begin{bmatrix} \mathbf{P}_1 & \mathbf{P}_2 \end{bmatrix} \begin{bmatrix} \mathbf{D}_1 & \mathbf{0} \\ \mathbf{0} & \mathbf{0} \end{bmatrix} \begin{bmatrix} \mathbf{Q}_1^T \\ \mathbf{Q}_2^T \end{bmatrix} = \mathbf{P}_1\mathbf{D}_1\mathbf{Q}_1^T \tag{6.3}$$

where $\mathbf{D}$ is the diagonal matrix of monotonically non-increasing singular values. $\mathbf{D}_1$ is an $N \times N$ ($N \leq p$) diagonal matrix formed by truncating the relatively small singular values. N is the final system order. It is worth noting that the selection of the final model order it not a trivial task (Nayeri et al., 2006). The discrete-time state-space realization matrices for the structural model can be estimated as (Juang and Pappa, 1985)

$$\hat{\mathbf{A}} = \mathbf{D}_1^{-1/2}\mathbf{P}_1^T\mathbf{H}(1)\mathbf{Q}_1\mathbf{D}_1^{-1/2} \tag{6.4}$$

$$\hat{\mathbf{C}} = \mathbf{E}_m^T \mathbf{P}_1 \mathbf{D}_1^{1/2} \tag{6.5}$$

where $\mathbf{E}_m^T = \begin{bmatrix} \mathbf{I} & \mathbf{0} \end{bmatrix}$, and its size is determined accordingly. The control influence matrix can not be estimated using the output-only information. The estimated discrete-time realization needs to be transformed to the continuous-time domain version, and the modal parameters can then be extracted from the identified continuous-time system (Nayeri et al., 2007).

There are lots of issues with the implementation of these techniques, including: selection of user-selectable parameters such as the size of the SVD matrix, the reference DOF (or DOFs), window size, final model order, and more important, recognizing and eliminating spurious modes which will appear due to noise and model overspecification. Nayeri et al. (2006) addressed these problems in detail.

Implementation and results

This section reports the results of the application of the proposed algorithms to the VTB recorded data. As was mentioned earlier, for implementing the NExT/ERA algorithm, only output acceleration records are needed. In this study, three distinct time windows of data were considered. The first window captures data during the accident (impact type excitation), which lasted about twenty minutes, the second one corresponds to the traffic shut-down period which lasted about two hours, and the third window corresponds to regular traffic conditions for eight hours. Relatively long time-history records were used to enhance the stationarity of the analysis data.

As shown in Figure 6.2, the VTB was instrumented with twenty-six accelerometers, however, only the acceleration measurements on the main deck, and towers (six vertical, six lateral, and three longitudinal directions) were used in this study. Sensors at the base of the VTB recorded negligible levels of response. Data were recorded at a sampling rate of 100 Hz. Since the frequency range of interest is less than 5 Hz, the data (after pre-processing) were down-sampled to 50 Hz.

After pre-processing (filtering, detrending, etc.), the next step was to compute the Cross-Correlation Functions (CCF) between the response of the preselected reference DOF (or, for more reliability, multiple DOFs) and the response of all available DOFs. As mentioned earlier, one cannot rely on just one single reference DOF for all modes. One single reference that is a proper selection for some modes, might not be proper for other modes. Consequently, it is recommended to use *multiple* reference DOFs, as opposed to a *single* reference DOF (Nayeri et al., 2006). In this study, in order to improve the identification results, all available DOFs were included (in sequential order) as the reference ones. The CCF can be estimated by the inverse Fourier transform of the Cross-Power-Spectral Density (CPSD), where the CPSD is computed directly from the data. Random errors associated with the CPSD can be minimized by windowing and averaging (Bendat and Piersol, 2000).

Three different time windows were considered in this study: (1) during accident (impact type excitation), (2) traffic shut down, and (3) regular traffic. Table 6.3 summarizes the modal parameter identification results for the three above mentioned time windows. A total of five dominant modes were identified: the first lateral bending (Mode A), first vertical bending (Mode B), first torsion (Mode C), second vertical bending (Mode D), and second torsion (Mode E). One interesting observation from this table is that the first lateral mode only appeared during the accident. This makes sense, since the traffic can barely excite that pure lateral mode. Mode

Table 6.3: Comparison of the VTB modal parameter identification results using NExT/ERA for three different cases: (1) during accident (impact type excitation), (2) traffic shut down, and (3) regular traffic. For all cases: window size and overlap=327.68 sec and 75%, respectively, and all available DOFs are used as the reference. For ERA: $r = 30$, and $p = 2/3$ of the correlation data points.

Mode No.	Mode shape	Natural frequency (Hz) and damping ratio (%)			Mode shape ratio w/ MAC (%) and frequency difference (%)		
		impact (1)	w/o traffic (2)	w/ traffic (3)	(1) & (2)	(1) & (3)	(2) & (3)
A	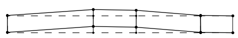 (top view)	0.1496	–	–	–	–	–
		4.0%	–	–	–	–	–
B	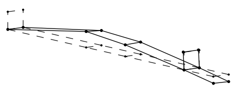	0.2327	0.2441	0.2353	99.7%	99.9%	99.8%
		2.7%	2.5%	1.9%	4.87%	1.11%	3.61%
C	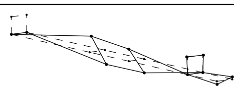	0.5357	0.5430	0.5339	99.8%	99.7%	99.4%
		0.8%	0.6%	0.6%	1.36%	0.67%	0.68%
D	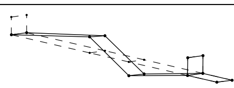	1.3938	1.3920	1.4004	99.2%	99.7%	98.9%
		1.5%	1.3%	1.7%	0.13%	0.47%	0.60%
E	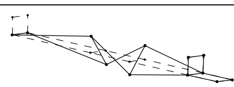	1.8685	1.8930	1.8668	98.9%	98.7%	99.3%
		1.3%	1.2%	1.9%	1.31%	0.09%	1.38%

shape and frequency comparisons between the results of these three time windows indicate that the mode shapes are virtually identical; however, there is up to a 5% change in frequency. That is not a surprise in view of the uncertainty issues related to environmental conditions.

Comparison with previous identification studies for different earthquakes

The identification results in this study are compared with previous identification works by Luş et al. (1999) and Smyth et al. (2003). In their identification work, Luş et al. (1999) employed the ERA method with the Observer/Kalman filter Identification (OKID) approach to extract the modal parameters of the Vincent Thomas Bridge, based on the data obtained during the 1987 Whittier and 1994 Northridge earthquakes. Using the same earthquake data sets, Smyth et al. (2003) applied a linear least-squares method to identify the bridge. The three identification results are summarized in Table 6.4. Obviously, the number of identified modes in this study is smaller than those in the previous studies. As mentioned earlier, we used an autonomous algorithm to eliminate the spurious modes and include only genuine modes of the bridge. This autonomous algorithm works based on some accuracy indicators, which are used to perform a validation test (Nayeri et al., 2006). Thus, the modes not satisfying the test criteria are regarded as non-genuine modes and automatically eliminated from the process. The mode shapes in Table 6.3 clearly indicate that non-genuine modes were successfully rejected. Moreover, the genuine modes identified in this study repeatedly appeared in different identification time-windows under both the impact and ambient vibration conditions. The repeatability of the identified modes in various excitation conditions is critical for reliable structural health monitoring applications.

Uncertainty study of the bridge identification

A statistical study was performed to estimate the identification uncertainty. Because the structural conditions of the bridge characterized with the identification methods used in this study could vary significantly with different excitation and environmental conditions (e.g. traffic intensity and temperature), it is important to estimate the bounds of uncertainty in the identification results. For three-month duration (July, 2007 $\sim$ September, 2007), the statistics of the identified natural frequencies and damping ratios were obtained. The statistics were obtained separately for weekdays and weekends because a significant difference of the bridge response was observed between weekdays and weekends, as shown in Figure 6.9. Sample distributions of the identified

Table 6.4: Comparison of the bridge identification results with previous studies for different earthquakes. The previous studies in the comparison include Smyth et al. (2003) and Luş et al. (1999) for the 1987 Whittier and 1994 Northridge earthquakes. In the table, f is the natural frequency (Hz), and ζ is the damping ratio (%).

Smyth et al. (2003)				Luş et al. (1999)				Yun et al.					
Vertical direction				All directions				All directions					
Whittier		Northridge		Whittier		Northridge		Impact		w/o traffic		w/ traffic	
f	ζ	f	ζ	f	ζ	f	ζ	f	ζ	f	ζ	f	ζ
0.212	1.2	0.225	0.1	0.234	1.5	0.225	1.7	0.150	4.0	–	–	–	–
0.242	1.7	0.240	8.2	0.388	38.2	0.304	28.6	0.233	2.7	0.244	2.5	0.235	1.9
0.317	-4.3	0.358	-4.7	0.464	9.7	0.459	1.8	0.536	0.8	0.543	0.6	0.534	0.6
0.531	10.2	0.390	4.2	0.576	9.9	0.533	4.0	1.394	1.5	1.392	1.3	1.400	1.7
0.570	0.6	0.448	-0.7	0.617	14.5	0.600	26.2	1.869	1.3	1.893	1.2	1.867	1.9
0.636	4.2	0.478	1.3	0.617	76.8	0.632	13.7						
0.672	0.1	0.522	1.4	0.769	29.7	0.791	15.6						
0.734	2.4	0.587	-0.1	0.804	1.4	0.811	1.0						
0.818	1.9	0.625	7.4	0.857	11.6	0.974	2.7						
0.958	2.9	0.733	1.2	0.947	4.3	1.110	0.6						
1.027	-1.9	0.837	5.0										
1.111	1.3	0.935	-1.8										
1.159	1.7	1.036	1.6										
1.391	2.3	1.110	1.7										
1.554	-1.3	1.136	1.4										

natural frequencies and damping ratios for Mode B (the first vertical bending) are illustrated in Figure 6.10.

The average of natural frequencies and damping ratios for four different identified modes (Modes B $\sim$ E) were determined with the averaged sample sizes of 288 for weekdays and 123 for weekends. The sample size of each mode varied because not all modes were identifiable with ambient vibration in the NExT-ERA identification. The mean of the averaged natural frequency for weekdays and weekend differed from 0.39% to 1.47%. The coefficient of variance of the averaged natural frequency was determined between 0.35% and 1.98% for weekdays, and between 0.41% and 1.85% for weekend. Thus, no significant difference for weekdays and weekend was observed in the averaged natural frequencies. For the averaged damping ratio, the difference of its mean ranged from 7.13% to 19.64%, and the coefficient of variance ranged from 0.98% to 45.64%. Therefore, the discrepancy between the averaged damping ratio for weekdays

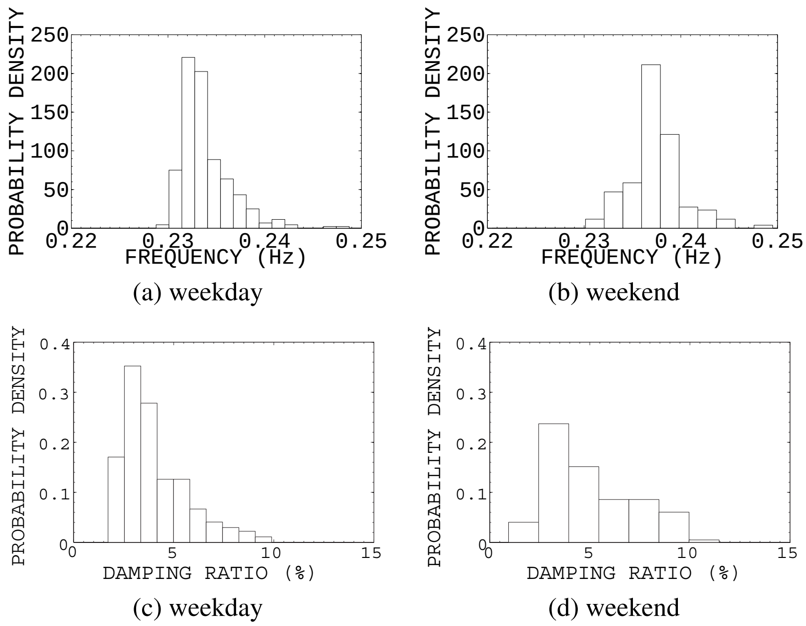

Figure 6.10: Histograms of the natural frequencies and damping ratios of the first vertical bending mode (Mode B) identified using the ERA method.

and weekend is greater than that of the averaged natural frequency. Therefore, it was observed that the uncertainty of identifying the damping ratio was greater than that of identifying the natural frequency.

Effects of temperature variation

It is well known that the effects of temperature variations are very significant to the dynamic response of bridges, and in many cases, the genuine changes of bridge modal properties could be overwhelmed by the temperature-induced changes. Unfortunately, because no temperature measurements were conducted in this study due to the limitation of the current monitoring system configuration, more rigorous studies of this important temperature effects could not be performed. However, this chapter is designed to demonstrate the practical applications of the

SHM approaches for forensic investigations, and advanced issues of the bridge identification are beyond the scope of this study.

6.5.2 Local System Identification Approaches

Identification of natural frequency and damping ratio

Once the global (multiple-sensor) system identification was performed, local (single-sensor) identification approaches were also applied independently for comparison purposes. Modal frequencies and damping ratios of the lateral displacement modes of the bridge deck were estimated. The logarithmic decrement (δ) method was used to estimate modal damping ratio as (Meirovitch, 1986):

$$\delta_j = \frac{1}{j} \ln \frac{x_1}{x_{j+1}}, \qquad \bar{\delta} = \frac{1}{n} \sum_{j=1}^{n} \delta_j \tag{6.6}$$

$$\bar{\zeta} = \frac{\bar{\delta}}{\sqrt{(2\pi)^2 + \bar{\delta}^2}} \cong \frac{\bar{\delta}}{2\pi} \tag{6.7}$$

where x_j is the j^{th} peak displacement, δ_j is the logarithmic decrement between x_1 and x_{j+1}, $\bar{\delta}$ is the averaged logarithmic decrement, and $\bar{\zeta}$ is the averaged damping ratio. The averaged damping ratios of sensors 3 and 5 were calculated with the peaks and valleys of the oscillation as shown in Figure 6.11 (a). A slight discrepancy of $\bar{\zeta}$ between the peaks and valleys was observed. The $\bar{\zeta}$ of peaks and valleys were measured at 6.40 and 4.78 for sensor 3, and 6.40 and 4.60 for sensor 5, respectively. Notice that the averaged values of $\bar{\zeta}$ of peaks and valleys for sensors 3 and 5 were 5.59 and 5.50. Second, the natural frequencies of the bridge deck at sensors 3 and 5 were also estimated from its power spectral density plot as shown in Figure 6.11 (b). The estimated lateral natural frequencies (ω_n) of the bridge were 0.138 Hz for sensor 3, and 0.142 Hz for sensor 5. The identification results of the lateral damping ratios and natural frequencies of the bridge deck are summarized in Table 6.5.

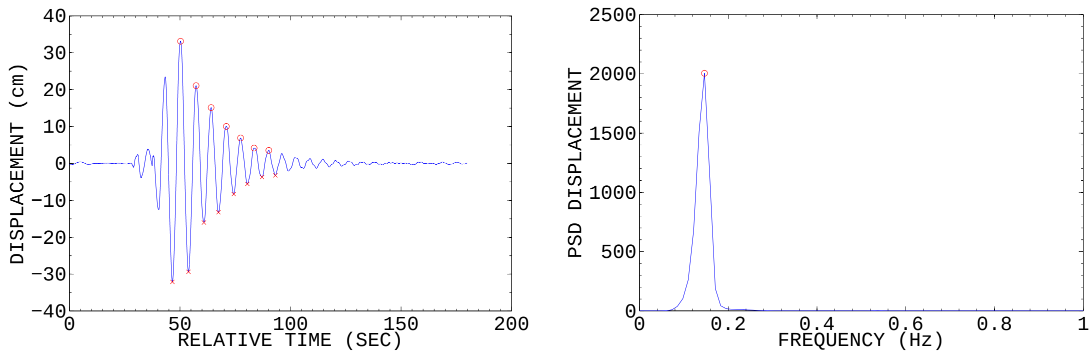

(a) Time history

(b) Power spectral density

Figure 6.11: Local identification of the damping ratio and natural frequency of the bridge deck in lateral direction (sensor 3) during the incident impact.

The natural frequencies and damping ratios of the vertical and torsional bridge response were also estimated. First, the vertical displacements at the center of the main span (sensors 15 and 16) and their frequency spectra are shown in Figures 6.12 (a)-(d). From the frequency spectra, two identical natural frequencies were identified at 0.232 Hz and 0.537 Hz for both sensors 15 and 16. The torsional displacement was obtained from the subtraction between the time histories of sensors 15 and 16 as shown in Figure 6.12 (e). The natural frequencies of the torsional displacement were identified at 0.147 Hz and 0.537 Hz for sensors 15 and 16, and at 0.147 Hz, 0.537 Hz, and 0.717 Hz for sensors 17 and 18. The slight variations in the single-sensor frequency estimates are primarily attributable to mode-order-reduction effects.

In order to estimate the damping ratios for the identified natural frequencies, a bandpass filter was applied to the torsional displacement, and Equations 6.6 and 6.7 were used for the

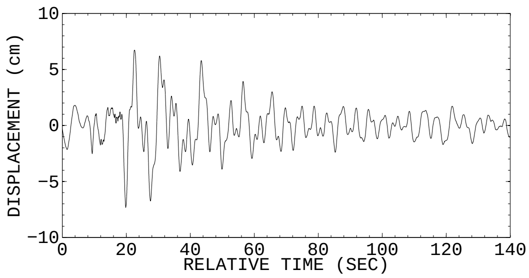

(a) Time history of sensor 15

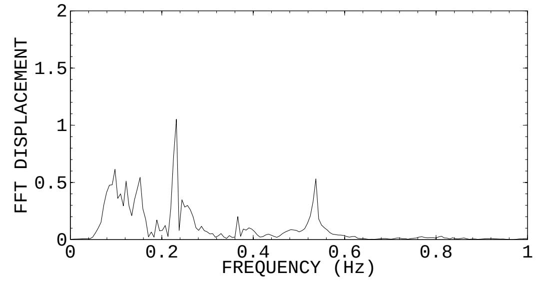

(b) Frequency spectrum of sensor 15

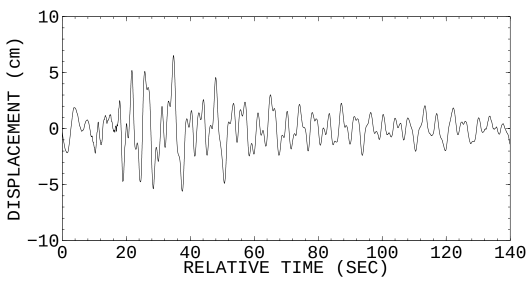

(c) Time history of sensor 16

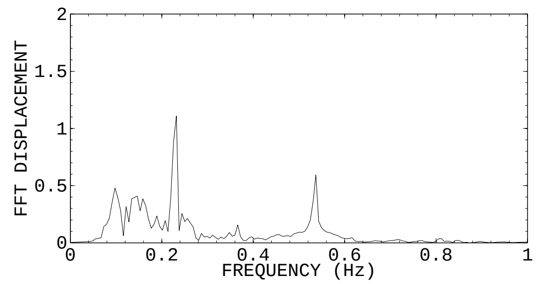

(d) Frequency spectrum of sensor 16

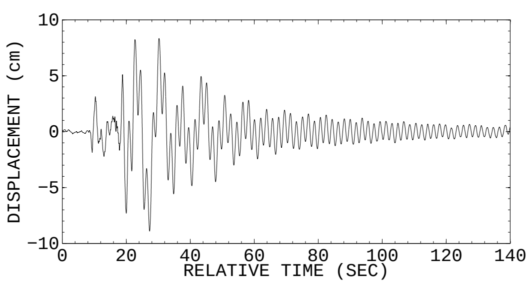

(e) Time history of the difference of sensors 15 and 16

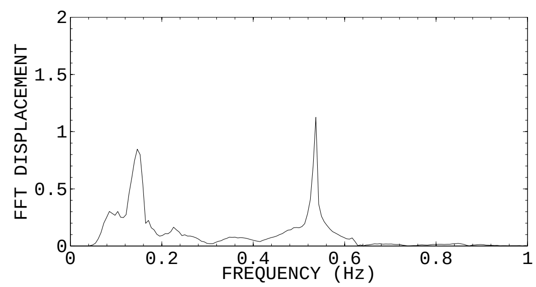

(f) Frequency spectrum of the difference of sensors 15 and 16

Figure 6.12: The vertical and torsional displacements at the center of the bridge deck (sensors 15 and 16). The torsional displacement was obtained with the subtraction between the time histories of sensors 15 and 16.

filtered signal. An example of the damping ratio estimation for the torsional displacement is shown in Figure 6.13. The damping ratios based on sensors 15 and 16 for peaks and valleys were identified at 4.8% (peak) and 6.9% (valley) for the natural frequency of 0.147 Hz, and 0.5% (peak) and 0.6% (valley) for the natural frequency of 0.537 Hz. The damping ratios for sensors 17 and 18 were identified at 5.0% (peak) and 7.3% (valley) for the natural frequency of

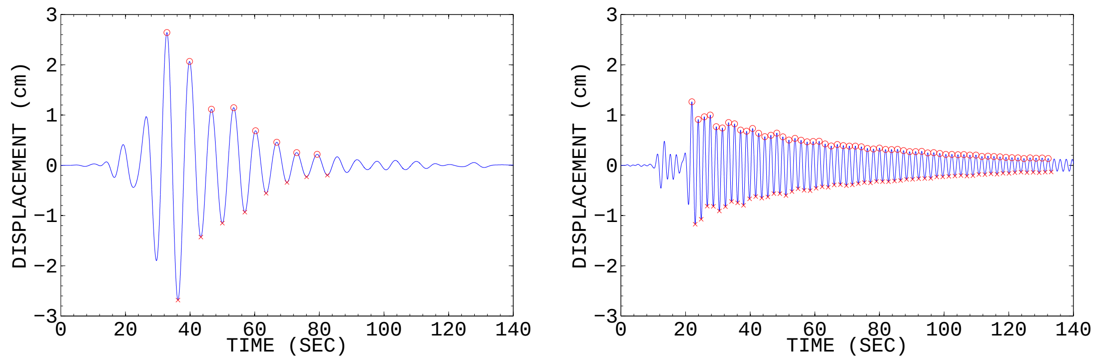

(a) Cutoff frequencies: 0.13 $\sim$ 0.2 Hz (b) Cutoff frequencies: 0.5 $\sim$ 0.6 Hz

Figure 6.13: The estimation of damping ratios for torsional displacement. The damping ratios were estimated with the bandpass-filtered signal of the torsional displacement illustrated in Figure 6.12 (e).

Table 6.5: Summary of estimated local damping ratios of the bridge deck.

Direction	Sensor No.	Locations	Averaged damping ratio (%) peaks	valleys	average	Frequency (Hz)
Lateral	3	center	6.4	4.8	5.6	0.138
	5	east quarter	6.4	4.6	5.5	0.142
Vertical	15	center	–	–	–	0.232
			–	–	–	0.537
	16	east quarter	–	–	–	0.232
			–	–	–	0.537
			–	–	–	0.720
Torsional	$\triangle(15-16)$	center	4.8	6.9	5.8	0.147
			0.5	0.6	0.6	0.537
	$\triangle(17-18)$	east quarter	5.0	7.3	6.1	0.147
			0.5	0.7	0.6	0.537
			1.0	1.0	1.0	0.717

0.147 Hz, 0.5% (peak) and 0.7% (valley) for the natural frequency of 0.537 Hz, and 1.0% (peak) and 1.0% (valley) for the natural frequency of 0.717 Hz. The identified damping ratios of the bridge deck are summarized in Table 6.5.

Phase of two different sensor readings

The cross-correlation of bridge displacements was measured to determine the phase lag of two

Table 6.6: Time lags and dominant frequencies of cross-correlation for different sensor readings.

Direction	Sensor no.	Time lag (sec)	Dominant frequency (Hz)
Lateral	3 and 4	0	0.147
Vertical	15 and 16	approx. 8	0.232 and 0.537

different sensor readings. Figure 6.14 (a) illustrates the cross-correlation of the lateral displacements at the main span of the bridge deck (sensors 3 and 5). The cross-correlation shows that the time lag between sensors 15 and 16 is zero, which implies the oscillation phases of the sensors are identical. The frequency spectrum of the cross-correlation shows that the dominant frequency is placed at 0.147 Hz, which is almost identical to the identified natural frequencies of the lateral displacements, 0.138 Hz for sensor 3 and 0.142 Hz for sensor 5 shown in Table 6.5 (Figure 6.14 (b)). The cross-correlation of the vertical displacements, sensors 15 and 16, was also determined, and its time lag was measured at approximately 8 seconds; that is, the period of relative vertical displacement between sensors 15 and 16. The dominant frequencies of the cross-correlation spectrum were observed at 0.232 Hz and 0.537 Hz. The time lags and dominant frequencies of the cross-correlation are summarized in Table 6.6.

6.5.3 Comparison of Global and Local Identification Results

Once the local identification was performed, the results of the local identification were compared with those of the global identification for validation purpose. A comparison of the global and local identification results is shown in Table 6.7. As depicted in the table, only minor discrepancies were observed between the global and local identification results for Modes A through C. Notice that the same natural frequency and damping ratio of Mode A, a strong lateral motion, were observed from the torsional displacements of sensors 15 and 16, and sensors 17 and 18,

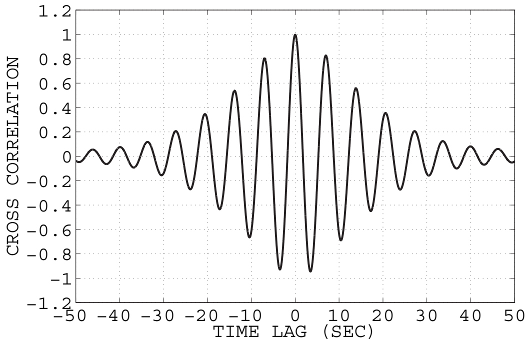

(a) Cross-correlation of lateral displacement

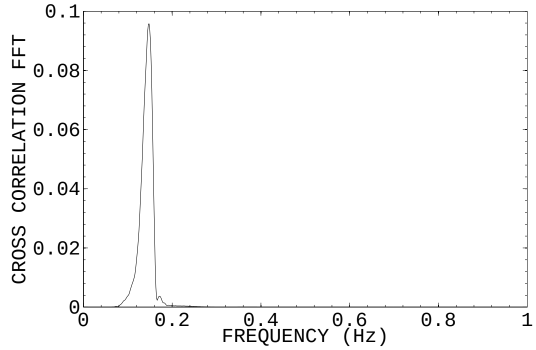

(b) FFT of cross-correlation of lateral displacement

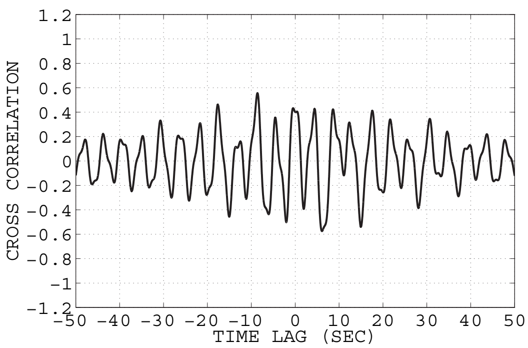

(c) Cross-correlation of vertical displacement

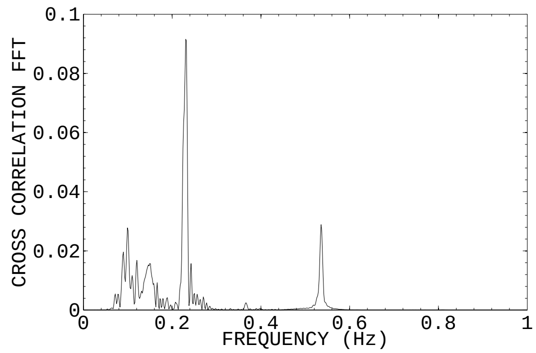

(d) FFT of cross-correlation of vertical displacement

Figure 6.14: Cross-correlation and its frequency spectrum for the lateral displacements (sensors 3 and 5) and vertical displacements (sensors 15 and 16) of the bridge deck.

which are the differences of those two-vertical displacements. Figure 6.15 shows a top view and lateral view of Mode A identified with the global identification method. Although a lateral motion is dominant in this mode (Figure 6.15 (a)), there also exists a minor torsional motion (Figure 6.15 (b)). Thus, the natural frequency and damping ratio of Mode A were also observed in the torsional displacement calculated from sensors 15 and 16, and from sensors 17 and 18.

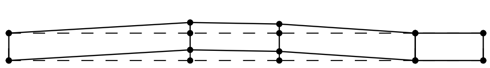

(a) Top view

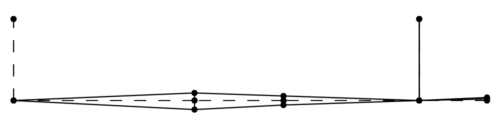

(b) Lateral view

Figure 6.15: Top and lateral views of Mode A identified with the global identification methods.

Modes D and E, which are relatively higher modes identified with the global identification method, were not successfully observed with the local identification. It should be noticed that using the global identification method, these higher modes were accurately determined with the ambient excitation as well as the impact excitation during the incident.

Using the local identification method, the natural frequency of 0.717 Hz and its corresponding damping ratio of 1.0% were identified with the torsional displacement calculated from sensors 17 and 18. This is approximately the quarter-point of the bridge main span. The same natural frequency and damping ratio were not observed with the torsional displacement calculated from sensors 15 and 16, located at the center of the main span. This is a symmetric torsional mode, and so the center of the main span is an antinode for the mode shape. Using the global identification method, this mode was detectable. However, the corresponding mode shape could not be determined due to a low sensor density.

6.6 Summary and Conclusions

This chapter reports on a study of the analysis of multi-channel time-history acceleration records captured by the digital instrumentation network installed on the Vincent Thomas Bridge, near the Port of Los Angeles, California, and caused by an accident that occurred on 27 August 2006 between a large cargo ship and the bridge.

Relatively long time history records of the bridge oscillations before, during, and after the accident, were used to analyze its nearly stationary response by applying multi-sensor system identification approaches, utilizing the Natural Excitation Technique with the Eigensystem Realization Algorithm. Modal parameter estimates for the bridge based on analysis of single-sensor

Table 6.7: A comparison of natural frequencies and damping ratios identified with global and local identification methods.

Global (Multi-Sensor) Identification				Local (Single-Sensor) Identification			Comparison	
Mode no.	Mode shape	f_G (Hz)	ζ_G (%)	sensor no.	f_L (Hz)	ζ_L (%)	$\frac{f_L}{f_G}$	$\frac{\zeta_L}{\zeta_G}$
A	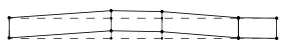	0.150	4.0	3	0.138	5.6	0.92	1.40
				5	0.142	5.5	0.95	1.38
				$\Delta(15-16)$	0.147	5.8	0.98	1.45
				$\Delta(17-18)$	0.147	6.1	0.98	1.53
				xcorr(3, 4)	0.147	–	0.98	–
B	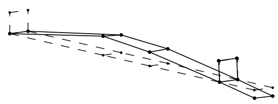	0.233	4.0	15	0.232	–	1.00	–
				16	0.232	–	1.00	–
				xcorr(15, 16)	0.232	–	1.00	–
C	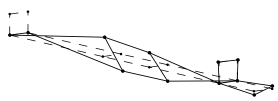	0.536	0.8	16	0.537	–		–
				$\Delta(15-16)$	0.537	0.6		–
				$\Delta(17-18)$	0.537	0.6		–
				xcorr(15, 16)	0.537	–		–
D	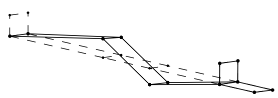	1.394	1.5	–	–	–	–	–
E	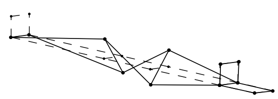	1.869	1.3	–	–	–	–	–
–	–	–	–	$\Delta(17-18)$	0.712	1.0	–	–
				16	0.720	–	–	–

measurements at selected locations were also used to demonstrate the range of validity of crude estimates of selected modal parameters when drastic reduction in the identified model-order is used.

By utilizing a web-enabled structural health monitoring system that is installed on the bridge, it is shown that analysis of the acquired sensor measurements, using various levels of sophistication in the digital signal processing of the captured data, can provide the owners of critical infrastructure systems with forensic tools that enable reliable and rapid assessment to analyze the circumstances and consequences of extreme events to which the target system is subjected.

The power of the results reported in this chapter is that it provides maintenance engineers with the ability to quickly determine the need for, or order of, visual inspection required after an event, such as an earthquake. Thus, assuming a number of large structures are appropriately instrumented, maintenance inspection engineers are able to review the damage potential at each location and schedule visual inspections, or investigations utilizing more sophisticated means, accordingly.

Chapter 7

Summary and Conclusion

The objective of this study was to develop effective modeling and monitoring methodologies for assessing the "health" of uncertain, nonlinear, dynamic systems. The SHM methodology proposed in this study is more advantageous than existing methodologies with the following three aspects: (1) its feasibility to detect (small) changes in complex nonlinear systems, (2) the possibility to make physical interpretation of detected changes, and (3) the possibility to quantify the uncertainty of change detection, which is usually influenced by various uncertainty sources. A series of investigations was performed by gradually introducing the complexities of various problems in modeling and monitoring uncertain nonlinear systems in a logical fashion. From the investigations reported in this thesis, the following important facts can be concluded:

Comparison of modeling approaches for full-scale nonlinear viscous damper

One parametric (simplified design model) and two non-parametric (Restoring Force Method and artificial neural networks) identification methods were compared using a full-scale nonlinear viscous damper of the type that is frequently employed to mitigate seismic and wind-induced vibration in civil structures. A series of experimental studies was conducted on the viscous damper. The viscous damper was successfully identified with the parametric as well as non-parametric identification methods. Among the modeling approaches investigated in this study, the Restoring Force Method was more advantageous than other methods for monitoring purposes due to the following aspects: (1) no *a priori* knowledge of the system being monitored is required; (2) the same model can be used when the system evolves into different types of nonlinearity; (3) the method is applicable to a wide range of nonlinearities; (4) both Chebyshev and power series coefficients can be identified; and (5) physical interpretation of some of the identification results is possible with identified coefficients.

Data-driven methodologies for change detection in large-scale nonlinear dampers with noisy measurements

There are two types of uncertainties affecting modeling and monitoring results of uncertain nonlinear systems: (1) measurement uncertainty (or measurement noise), and (2) system characteristic uncertainty (or variation of system parameters). Among them, the effects of the measurement uncertainty on the change detection performance were firstly investigated.

An experimental study was conducted using three different types of large-scale nonlinear viscous dampers, and multiple sets of tested dampers' response polluted with random noise were produced to investigate the stochastic effects of the measurement noise on the change detection performance. Using the Restoring Force Method, the viscous dampers were identified with the noisy measurements, and the corresponding coefficients were obtained.

It was found that the coefficients identified using the Restoring Force Method can be used as excellent features for (1) detecting the changes of nonlinear systems, (2) interpreting the physical meaning of the detected changes, and (3) quantifying the uncertainty of the detected system changes.

The Bootstrap method was also studied to estimate the uncertainty bounds on the coefficient identification, when the measurement data are insufficient for reliable statistical inference. Using the Bootstrap method, the uncertainty in the identification was estimated reasonably accurately even with a single data set when the displacement and force were measured, rather than when the acceleration and force were measured with random noise.

Model-order reduction effects on change detection in uncertain nonlinear magneto-rheological dampers

Once the effects of measurement uncertainty were understood, the effects of system characteristic uncertainty were investigated. In order to study the system characteristic uncertainty, a semi-active magneto-rheological (MR) damper was employed. Multiple sets of the damper's response were obtained for Gaussian distributions of MR damper input currents with different means and standard deviations. Here, the mean of the distribution determines the effective system characteristics and the standard deviation of distribution determines the uncertainty of the system characteristics.

A series of experimental studies was performed with the MR damper, and the MR damper was identified using the Restoring Force Method. Using the distributions of the corresponding identified coefficients, it was demonstrated that the developed change detection methodology can successfully assess the conditions of uncertain nonlinear systems by (1) detecting the effective (nominal) system changes with the mean changes of the coefficient distributions, (2) quantifying the uncertainty bounds of the detected changes with the standard deviation of the coefficient distributions, and (3) interpreting the physical meaning of the detected changes without a priori knowledge of the system characteristics.

Supervised and unsupervised statistical classification methods were applied to detect effective system changes with different levels of system uncertainty. Among the three coefficients available in the Restoring Force Method (the normalized Chebyshev coefficients, normalized power series coefficients, and de-normalized power series coefficients) the normalized Chebyshev coefficients with orthogonal basis functions demonstrated many advantageous aspects for change detection purposes, due to the statistical unbiasness of the identified coefficients, which was not observed with non-orthogonal power series coefficients identified with non-orthogonal basis functions. In addition, the change detection with statistically unbiased coefficients showed higher accuracy and less computation time with reduced-order models.

Monitoring the collision of a cargo ship with the Vincent Thomas Bridge

Once various important effects of uncertain nonlinear systems for the development of the component-level structural health monitoring were investigated, the scope of this study was expanded to the full-system-level structural health monitoring.

On 27 August 2006, the Vincent Thomas Bridge, an important suspension bridge in southern California, had a collision with a cargo ship. An investigation was performed on the multi-channel time-history acceleration records captured by the web-based digital instrumentation network installed on the bridge.

Relatively long time history records of the bridge oscillation before, during and after the accident, were used to analyze its nearly stationary response by applying multi-sensor system identification approaches, utilizing the Natural Excitation Technique with the Eigensystem Realization Algorithm. Modal parameter estimates for the bridge based on analysis of single-sensor measurements at selected locations were also used to demonstrate the range of validity of crude estimates of selected modal parameters, when drastic reduction in the identified model-order is used.

By utilizing a web-enabled structural health monitoring system that is installed on the bridge, it is shown that analysis of the acquired sensor measurements, using various levels of sophistication in the digital signal processing of the captured data, can provide the owners of critical infrastructure systems with forensic tools that enable reliable and rapid assessment to analyze the circumstances and consequences of extreme events to which the target system was subjected.

The power of this study is that it allows maintenance engineers the ability to quickly determine the need for, or order of, visual inspection required after an event, such as an earthquake. Thus, assuming a number of large structures are appropriately instrumented, maintenance inspection engineers are able to review the damage potential at each location and schedule visual inspections, or investigations utilizing more sophisticated means, accordingly.

References

Aaseng, G. B. (2001). "Blueprint for an integrated vehicle health management system." *The 20th Conference of the Digital Avionics Systems*, Vol. 1, Dayton, FL.

Abdel-Ghaffar, A., Masri, S. F., and Nigbor, R. N. (1995). "Preliminary report on the Vincent Thomas Bridge monitoring test." *Report No. Report No. M9510*, University of Southern California, Los Angeles, California.

Abdel-Ghaffar, A. M. and Housner, G. W. (1978). "Ambient vibration tests of suspension bridge." *Journal of the Engineering Mechanics Division, ASCE*, 104(EM5), 983–999.

Abdel-Ghaffar, A. M., Masri, S. F., and Niazy, A. S. M. (1992). "Seismic performance evaluation of suspension bridges." *Proceedings of the Tenth World Conference: Volume 1*. 4845–4850.

Aiken, I. (1996). "Passive energy dissipation - hardware and applications." *Los Angeles County and SEAOSC Symposium on Passive Energy Dissipation Systems for New and Existing Buildings*, Los Angeles.

Aiken, I. D. (1998). "Testing of seismic isolators and dampers - considerations and limitations." *Proceedings, Structural Engineering World Congress*, San Francisco, California.

Aiken, I. D. and Kelly, J. M. (1996). "Cyclic dynamic testing of fluid viscous dampers." *Proceedings, Caltrans' Fourth Seismic research Workshop*, Sacramento, California.

Aiken, I. D., Nims, D. K., Whittaker, A. S., and Kelly, J. M. (1993). "Testing of passive energy dissipation systems." *Earthquake Spectra*, 9(3).

Andronikou, A. M., Bekey, G. A., and Masri, S. F. (1982). "Identification of nonlinear hysteretic system using random search." *Proceedings of 6th IFAC Symposium on Identification and System Parameter Estimation*, Washington, D. C. 10721073.

ATC/MCEER (2003). *MCEER/ATC-49 Recommended LRFD Guidelines forthe Seismic Design of Highway Bridges - Part1: Specifications*, Vol. 1.

Baker, G. (1998). "Seismic retrofit of the vincent thomas suspension bridge, los angeles, california." *1998 Catalog of TRB Annual Meeting Practical Papers - VIII Bridge Design and Performance*, TRB, Design and Construction Group, Technical Activities Division.

Beck, J. L., Iwan, W. D., and Chen, J.-C. (1994). "International full-scale test facility for structural control." *Americal Control Conference, 1994*, INSPEC Accession No. 4880808.

Bendat, J. S. and Piersol, A. G. (2000). *Random Data - Analysis and Measurement Procedures*. A Wiley-Interscience Publication.

Bertsekas, D. P. (1999). *Nonlinear Programming*. Athena Scientific, 2 edition.

Boser, B. E., Guyon, I., and Vapnik, V. (1992). "A training algorithm for optimal margin classfiers." *Proceedings of the Fifth Annual Workshop on Computational Learning Theory*. ACM Press, 144–152.

Bottou, L. and Bengio, Y. (1995). "Convergence properties of the k-means algorithms." *Advances in Neural Information Processing Systems 7*, G. Tesauro and D. Touretzky, eds., MIT Press, 585–592.

BSSC (2004). *NEHRP Recommended Provisions for Seismic Regulations for New buildingsand Other Structures (FEMA 450) - Part1: Provisions*, Vol. 1. Building Seismic Safety Council, 2003 edition.

Burges, C. J. C. (1998). "A tutorial on Support Vector Machines for pattern recognition." *Data Mining and Knowledge Discovery*, 2(2), 121–167.

Caicedo, J. M., Dyke, S. J., and Johnson, E. A. (2004). "Natural excitation technique and eigensystem realization algorithm for phase I of the IASC-ASCE benchmark problem: simulated data." *ASCE Journal of Engineering Mechanics*, 130(1), 49–60.

Caltrans (2003). "The race to seismic safety - protecting california's transportation system." *Report no.*, Caltrans Seismic Advisory Board.

Carlstein, E. (1986). "The use of subseires values for estimating the variance of general statistic from a stationary sequence." *Ann. Statist.*, 14, 1171–1194.

Chen, W.-F. and Duan, L. (2000). *Bridge Engineering Handbook*. CRC Press LLC.

Constantinou, M. C. and Symans, M. D. (1993). "Experimental study of seismic response of buildings with supplemental fluid dampers." *Structural Design of Tall Buildings*, 2(93-132).

Constantinou, M. C., Symans, M. D., Tsopelas, P., and Taylor, D. P. (1993). "Fluid viscous dampers in applications of seismic energy dissipation and seismic isolation." Vol. 2.

Cortes, C. and Vapnik, V. (1995). "Support vector networks." *Machine Learning*, 20, 273–297.

Cover, T. M. (1965). "Geometrical and statistical properties of systems of linear inequalities with applications in pattern recognition." *IEEE Transactions on Electronic Computers*, 14, 326–334.

Datta, K. B. and Mohan, B. M. (1995). *Orthogonal Functions in Systems and Control*. World Scientific Publishing Co.

Davison, A. C. and Hinkley, D. V. (1997). *Bootstrap Methods and Their Application*. Cambridge University Press.

Den Hartog, J. P. (1956). *Mechanical Vibrations, Third Edition*. McGraw-Hill, 4 edition.

Duda, R. O. and Hart, P. E. (1973). *Pattern Classification and Scene Analysis*. John Wiley & Sons, Inc.

Dyke, S. J., Spencer Jr., B. F., Sain, M. K., and Carlson, J. D. (1996). "Modeling and control of magnetorheological dampers for seismic response reduction." *Smart Materials and Structures*, 5, 565–575.

Efron, B. (1979). "Bootstrap methods: anaother look at the jackknife." *Annals of Statistics*, 7, 1–26.

Efron, B. and Tibshirani, R. J. (1986). "Bootstrap methods for standard errors, confidence intervals, and other measures ofstatistical accuracy." *Statist. Science*, 1, 54–77.

Efron, B. and Tibshirani, R. J. (1993). *An Introduction to the Bootstrap*. CRC Press LLC.

Ehrgott, R. C. and Masri, S. F. (1992). "Modelling of oscillatory dynamic behavior of electrorheological materials in shear." *Journal of Smart materials and structures*, 4(275-285).

Ehrgott, R. C. and Masri, S. F. (1994). "Structural control applications of an electrorheological device." *Proceedings of the International Workshop on Structural Control*, Los Angeles, California. USC Publication, 115–129.

Fan, R.-E., Chen, P.-H., and Lin, C.-J. (2005). "Working set selection using the second order information for training SVM." *Journal of Machine Learning Research*, 6, 1889–1918.

FHWA (1972). *National Bridge Inspection Program (NBIP)*. Federal Highway Administration (FHWA) Technical Advisory T5140.21 (1988).

FHWA (2006). *Long-Term Bridge Performance Program (LTBP) - House Report 109-203 - Safe, Accountable, Flexible, Efficient Transportation Equity Act: A Legacy for Users*. Federal Highway Administration.

Fujino, Y., Nishitani, A., and Iemura, H. (2004). "Recent developmentsin structural control research, developments and practice in Japan." *The 4th International Workshop on Structural Control*, A. Smyth and R. Betti, eds., Columbia University, New York.

Gao, J., Shi, W., Tan, J., and Zhong, F. (2002). "Support Vector Machines based approach for fault diagnosis of valves in reciprocating pumps." *Proceedings of the 2002 IEEE Canadian Conference on Electrical and Computer Engineering*.

Hall, P. (1985). "Resampling a coverage pattern." *Stoch. Proc. Appl.*, 20, 231–246.

Härdle, W., Horowitz, J., and Kreiss, J.-P. (2003). "Bootstrap mehods for time series." *Internaltional Statistical Review*, 71(2), 435–459.

He, X., Moaveni, J. P., and Elgamal, A. (2004). "System identification of Vincent Thomas Bridge using simulated wind response data." *Proceedings of the Second International Conference on Bridge Maintenance, Safety and Management*.

HITEC (1996). *Guidelines for the Testing of Seismic Isolation and Energy Dissipating Devices*. CERF Report: HITEC 96-02. Highway Innovative Technology Evaluation Center.

HITEC (1998a). *Evaluation Findings for Enidine, Inc. Viscous Damper*. Highway Innovative Technology Evaluation Center.

HITEC (1998b). *Evaluation Findings for Taylor Devices Fluid Viscous Damper*. Highway Innovative Technology Evaluation Center.

HITEC (1999). *Summary of Evaluation Findings for the Testing of Seismic Isolation and Energy Dissipationg Devices*. CERF Report No. 40404. Higway Innovative Technology Evaluation Center.

Hogg, R. V. and Tanis, E. A. (1997). *Probability and Statistical Inference, 5th Edition*. Prentice Hall.

Housner, G. W., Bergman, L. A., Caughey, T. K., Chassiakos, A. G., Claus, R. O., Masri, S. F., Skelton, R. E., Soong, T. T., Spencer, B. F., and Yao, J. T. P. (1997). "Special issue: Structural control: Past,present and future." *ASCE, Journal of Engineering Mechanics*, 123(9), 897–971.

Hsu, C.-W., Chang, C.-C., and Lin, C.-J. (2007). "A practical guide to support vector classification." *Report no.*, National Taiwan University, http://www.csie.ntu.edu.tw/ cjlin/papers/guide/guide.pdf.

Infanti, S., Papanikolas, P., and Theodossopoulos, G. (2003). "Rion-antirion bridge: Full-scale testing of seismic devices." *Proceedings of Fib Symposium 2003 - Concrete structures in seismic resions*.

Ingham, T. J., Rodriguez, S., and Nadar, M. (1997). "Nonlinear analysis of the Vincent Thomas Bridge for seismic retrofit." *Computer and Structures*, 64(5), 1221–1238.

James, G. H., Carne, T. G., and Lauffer, J. P. (1993). "The natural excitation technique for modal parameter extraction from operating wind turbines." *Report No. SAND92-1666, UC-261*, Sandia National Laboratories.

James, G. H., Carne, T. G., and Mayes, R. L. (1996). "Modal parameter extraction from large operating structures using ambient excitation." *Proc. 14th Int. Modal Analysis Conf.*, Dearborn, Michigan, USA.

Juang, J. N. and Pappa, R. S. (1985). "An eigensystem realization algorithm for modal parameter identification and model reduction." *AIAA Journal of Guidance, Control, and Dynamics*, 8(5), 620–627.

Juang, J. N. and Pappa, R. S. (1986). "Effect of noise on modal parameters identified by the eigensystem realization algorithm." *AIAA Journal of Guidance, Control, and Dynamics*, 9(3), 294–303.

Kanungo, T., Mount, D. M., Netanyahu, N. S., Piatko, C. D., Silverman, r., and Wu, A. Y. (2002). "An efficient *k*-means clustering algorithm: Analysis and implementation." *IEEE Transactions on Pattern Analysis and Machine Intelligence*, 24(7), 881–892.

Kareem, A., Kijewski, T., and Tamura, Y. (1999)." *Wind and Structure, An International Journal*, 2(3).

Kitagawa, Y. and Midorikawa, M. (1998). "Seismic isolation and passive response-control buildings in japan." *Smart Materials and Structures*, 7, 581–587.

Kohavi, R. (1995). "A study of cross-validation and bootstrap for accuracy estimation and model selection." *International Joint Conference on Artificial Intelligence (IJCAI)*.

Kreiss, J. P. and Franke, J. (1992). "Boostrapping stationary autoregressive moving average models." *J. Time Ser. Anal.*, 13, 297–317.

Luş, H., Betti, R., and Longman, R. W. (1999). "Identification of linear structural systems using earthquake-induced vibration data." *Earthquake Engineering and Structural Dynamics*, 28, 1449–1467.

MacQueen, J. B. (1967). "Some methods for classification and analysis of mulivariate observations." *Proceedings of* $5^{textrmth}$ *Berkeley Symposium on Mathematical Statistics and Probability*. University of California Press, 281–297.

Makris, N. and Constantinou, M. C. (1991). "Fractional derivative model for viscous dampers." *Journal of Structural Engineering, ASCE*, 117, 2708–2724.

Makris, N., Constantinou, M. C., and Dargush, G. F. (1993). "Analytical model of viscoelastic fluid dampers." *Journal of Structural Engineering, ASCE*, 119(11), 3310–3325.

Mancini, S., Tumino, G., and Gaudenzi, P. (2006). "Structural health monitoring for future space vehicles." *Journal of Intelligent Material Systems and Structures*, 17, 577–585.

Mangasarian, O. L. (1997). "Mathematical programming in data mining." *Data Mining and Knowledge Discovery*, 1, 183–201.

Martinez, W. L. and Martinez, A. R. (2002). *Computational Statistics Handbook with MATLAB*. CRC Press LLC.

Mason, J. C. and Handscomb, D. C. (2003). *Chebyshev Polynomials*. CRC Press.

Masri, S. F., Bekey, G. A., and Safford, F. B. (1980). "A global optimization algorithm using adaptive random search." *Applied Mathematics and Computation*, 7, 353–375.

Masri, S. F. and Caughey, T. K. (1979). "A nonparametric identification technique for nonlinear dynamic problems." *Journal of Applied Mechanics, Trans. ASME.*, 46(2), 433–447.

Masri, S. F., Chassiakos, A. G., and Caughey, T. K. (1993). "Identification of nonlinear dynamic systems using neural networks." *ASME, Journal of Applied Mechanics*, 60, 123–133.

Masri, S. F., Ghanem, R., Arrate, F., and Caffrey, J. P. (2006). "Stochastic nonparametric models of uncertain hysteretic oscilliators." *American Institute of Aeronautics and Astronautics Journal (AIAA)*, 44(10), 2319–2330.

Masri, S. F., Sheng, L.-H., Caffrey, J. P., Nigbor, R. L., Wahbeh, M., and Abdel-Ghaffar, A. M. (2004). "Application of a web-enabled real-time structural health monitoring system for civil infrastructure systems." *Smart Materials and Structures*, 13, 1269–1283.

Masri, S. F., Smyth, A. W., Chassiakos, A. G., Caughey, T. K., and Hunter, N. F. (2000). "Application of neural networks for detection of changes in nonlinear systems." *ASCE, Journal of Engineering Mechanics*, 126(7), 666–676.

Masri, S. F., Smyth, A. W., Chassiakos, A. G., Nakamura, M., and Caughey, T. K. (1999). "Training neural networks by adaptive random search techniques." *ASCE, Journal of Engineering Mechanics*, 125(2), 123–132.

Mastaglio, L. (1997). "Bridge bashing." *Civil Engineering*, 38–40.

Meirovitch, L. (1986). *Elements of Vibration Analysis*. McGraw-Hill Inc.

Mendel, J. M. (1995). *Lessons in Estimation Theory for Signal Processing, Communications, and Control*. Prentice Hall, Inc.

Mendenhall, W. and Sincich, T. (1995). *Statistics for Engineering and the Sciences, 4th Edition*. Prentice Hall.

Mita, A. and Hagiwara, H. (2003). "Damage diagnosis of a building structure using support vector machine and modal frequency patterns." *Smart Systems and Nondestructive Evaluation for Civil Infrastructures*, S.-C. Liu, ed., Vol. Volume 5057. 118–125.

National Aeronautics and Space Administration (2007). *NASA - Integrated Vehicle Health Management (IVHM)*. http://www.nasa.gov/centers/ames/research/humaninspace/humansinspace-ivhm.html.

Nayeri, R. D., Masri, S. F., and Chassiakos, A. G. (2007). "Use of eigensystem realization algorithm to track structural changes in a retrofitted building based on ambient vibration." *ASCE Journal of Engineering Mechanics*. submitted.

Nayeri, R. D., Tasbihgoo, F., Masri, S. F., Caffrey, J. P., Conte, J. P., He, X., Moaveni, B., Wahbeh, M., Whang, D. H., and Elgamal, A. (2006). "Comparative study of time-domain techniques for modal parameter identification of the New Carquinez Bridge." *ASCE Journal of Engineering Mechanics*. submitted.

Oh, C. K. and Beck, J. L. (2006). "Sparse Baysian learning for structural health monitoring." *4th World Conference on Structural Control and Monitoring*, San Diego.

Ou, J. (2004). "Recent advances on structural control in mainland china." *The 4th International Workshop on Structural Control*, A. Smyth and R. Betti, eds., Columbia University, New York.

Ou, J. and Li, H. (2004). "Recent advances of structural vibration control in mainland of china." *2004 ANCER Annual Meeting - Earthquake Disaster Prevention and Mitigation Research Center*.

Paik, I.-Y., Koh, H.-M., Yun, C.-B., and Choo, J.-F. (2004). "Progress of structural control and monitoring technologies in Korea and Korea panel's activities." *The 4th International Workshop on Structural Control*, A. Smyth and R. Betti, eds., Columbia University, New York.

Park, S.-H., Yun, C.-B., and Roh, Y. (2005). "PZT-induced Lamb waves and pattern recognitions for on-line health monitoring of jointed steel plates." *Proceedings of SPIE International Symposium on Smart Structures and Materials*. 364–375.

Park, W. and Koh, H.-M. (2001). "Application and r&d of active, semi-active and hybrid vibration control techniques for civil structures in korea." *7th International Seminar on Seismic Iso;ation, Passive Energy Dissipation and Active Control of Vibrations of Structures*, Assisi, Italy.

Peeters, B., Maeck, J., and Roeck, G. D. (2001). "Vibration-based damage detection in civil engineering: excitation sources and temperature effects." *Journal of Smart Materials and Structures*, 10, 518–527.

Pollard, D. (1982). "A central limit theorem for k-means clustering." *Annals of Probability*, 10, 919–926.

Proske, D. and Curback, M. (2003). "Risk to old bridges due to ship impact on German inland waterways." *Swets Zeitlinger, Lisse, ISBN 90 5809 551 7*, 1263–1270.

Prosser, W. H., Woodard, S. E., Wincheski, R. A., Cooper, E. G. Price, D. C., Hedley, M., Prokopenko, M., Scott, D. A., Tessler, A., and Spangler, J. L. (2004). "Structural health management for future aerospace vehicles." *In Proceedings of the 2nd Australasian Workshop on Structural Health Monitoring (2AWSHM)*, Melbourne, Australia.

Rodellar, J. (2004). "A technical overview of European research in structural control and health monitoring." *The 4th International Workshop on Structural Control*, A. Smyth and R. Betti, eds., Columbia University, New York. 18–28.

Schölkopf, B. and Smola, A. J. (2002). *Learning with Kernels*. The MIT Press.

Schölkopf, B., Smola, A. J., Willianson, R. C., and Bartlett, P. L. (2000). "New support vector algorithms." *Neural Computation*, 12, 1207–1245.

Schwabacher, M., Samuels, J., and Brownston, L. (2002). "The NASA Integrated Vehicle Health Management technology experiment for X-37." *Proceedings of the SPIE AeroSense 2002 Symposium*, Orlando, FL.

Scott, D. W. (1979). "On optimal and data-based histograms." *Biometrika*, 66(3), 605–610.

Scott, D. W. (1992). *Multivariate Density Estimation: Theory, Practice and Visualization*. Wiley, New York.

Seber, G. A. F. and Lee, A. J. (2003). *Linear Regression Analysis*. John Wiley & Sons, Inc., Canada, 2 edition.

Selim, S. Z. and Ismail, M. A. (1984). "k-means-type algorithms: a generalized convergence theorem and characterization of local optimality." *IEEE Trans. Pattern Analysis and Machine Intelligence*, 6, 81–87.

Sheng, L.-H. and Lee, D. (2003). "Performance of viscous damper and its acceptance criteria." *Earthquake Engineering 2003 - Advancing Mitigation Technologies and Disaster Response for Lifeline Systems*, J. E. Beavers, ed., Vol. TCLEE Monograph No. 25, 6th U.S. Conference and Workshop on Lifeline Earthquake Engineering.

Shenton, H. W. (1994). "Standard test procedures for seismic isolation systems." *Proceedings, U.S./Japan Natural resources Development Program (UJNR). Wind and Seismic Effects. joint meeting of the U.S./Japan Cooperative Program in Natural Resources Panel on Wind and Seismic Effects, 26th*, J. Raufaste, N. J., ed. 97–107.

Shi, S. G. (1991). "Local Bootstrap." *Ann. Inst. Statist.*, 43, 667–676.

Smola, A. J. and Schölkopf, B. (1998). *A tutorial on Support Vector Regression*. ESPRIT Working Group in Neural and Computational Learing II, http://www/neurocolt.com.

Smyth, A. W., Pei, J.-S., and Masri, S. F. (2003). "System identification of the Vincent Thomas Suspension Bridge using earthquake records." *Earthquake Engineering and Structural Dynamics*, 32, 339–367.

Soong, T. T. (1998). "Experimental simulation of degrading structures through active control." *Earthquake Engineering and Structural Dynamics*, 27, 143–154.

Soong, T. T. and Constantinou, M. C. (1994). *Passive and Active Structural Vibration Control in Civil Engineering (CISM International Centre for Mechanical Sciences)*. Springer, 1 edition.

Soong, T. T. and Dargush, G. F. (1997). *Passive Energy Dissipation Systems in Structural Engineering*. John Wiley & Sons Ltd.

Spencer, Jr., B. F., Carlson, J. D., Sain, M. K., and Yang, G. (1997). "On the current status of magnetorheological dampers: seismic protection of full-scale structures." *Proceedings of the American Control Conference (AACC)*, Albuquerque, New Mexico.

Spencer, Jr., B. F. and Yang, G. (2004). "Recent developments in structural control research in the U.S.." *The 4th International Workshop on Structural Control*, A. Smyth and R. Betti, eds., Columbia University, New York. 3–12.

Spencer, Jr., B. F., Yang, G., Carlson, J. D., and Sain, M. K. (1998). "Smart dampers for seismicprotection of structures: A full-scale study." *Proceedings of the 2nd World Conference on Structural Control*, Kyoto, Japan. 417–426.

Spencer Jr., B. F. and Nagarajaiah, S. (2003). "State of the art of structural control." *Journal of Structural Engineering*, 845–856.

Stevens, W. R. (1998). *UNIX Network Programming, Volume 2: Interprocess Communications*. Prentice Hall PTR.

Stevens, W. R., Fenner, B., and Rudoff, A. M. (2002). *Unix Network Programming, Volume 1: The Sockets Networking API*. Addison-Wesley Professional.

Tachibana, E. and Mita, A. (2006). "Recent development of structural control and health monitoring in Japan." *The 4th World Conference on Structural Control and Monitoring (4WCSCM)*, University of California, San Diego, San Diego, California.

Theiler, J., Eubank, S., Longtin, A., Galdrikian, B., and Farmer, J. D. (1992). "Testing for nonlinearity in time series: the method of surrogate data." *Physical Review D*, 58, 77–94.

Timmer, J. (1998). "Power of surrogate data testing with respect to non-stationarity." *Physical Review E*, 58, 5153–5156.

Vapnik, V. (1995). *The Nature of Statistical Learning Theory*. Springer, New York.

Vapnik, V. N. (1998). *Statistical Learning Theory*. Wiley, New York.

Wahbeh, A. M., Caffrey, J. P., and Masri, S. F. (2003). "A vision-based approach for the direct measurement of displacements in vibrating systems." *Smart Materials and Structures*, 12, 785–794.

Wahbeh, M., Tasbihgoo, F., Yun, H., Masri, S. F., Caffrey, J. P., and Chassiakos, A. G. (2005). "Real-time earthquake monitoring of large scale bridge structures." *Proceedings of the international workshop on structural health monitoring*.

Wolfe, R. W., Masri, S. F., and Caffrey, J. (2002). "Some structural health monitoring approaches for nonlinear hydraulic dampers." *Journal of Structural Control*, 9(1), 5–8.

Worden, K. and Lane, A. J. (2001). "Damage identification using support vector machines." *Smart Materials and Structures*, 10, 540–547.

Worden, K. and Tomlinson, G. R. (2001). *Nonlinearity in Structural Dynamics: Detection, Identification and Modelling*. Institute of Physics Pub.

Yang, G., Spencer, Jr., B. F., Jung, H.-J., and Carlson, J. D. (2004). "Dynamic modeling of large-scale magnetorheological damper systems for civil engineering applications." *ASCE Journal of Engineering Mechanics*, 130(9), 1107–1114.

Yun, C.-B. (2006). "Structural health monitoring and damage assessment technologies: developments and applications in Korea." *The 4th World Conference on Structural Control and Monitoring (4WCSCM)*, University of California, San Diego, San Diego, California.

Yun, C.-B., Park, S., and Inman, S. (2006). "Health monitoring of railroad tracks using PZT active sensors associated with Support Vector Machines." *Proceedings of 4th China-Japan-US Symposium on Structural Control and Monitoring*, Hangzhou, China.

Yun, H., Nayeri, R., Tasbihgoo, F., Wahbeh, M., Caffrey, J., Wolfe, R., Nigbor, R., Masri, S., Abdel-Ghaffar, A., and Sheng, L.-H. (2007). "Monitoring the collision of a cargo ship with the Vincent Thomas Bridge." *Structural Control and Health Monitoring*.

Yun, H., Tasbihgoo, F., Masri, S. F., Caffrey, J. P., Wolfe, R. W., Makris, N., and Black, C. (2007). "Comparison of modeling approaches for full-scale nonlinear viscous dampers." *Journal of Vibration and Control - JVC Special Issue in honor of Professor Vestroni*.

Zhang, J., Sato, T., and Iai, S. (2006). "Incremental Support Vector Regression for non-linear hysteretic structural identification." *4th World Conference on Structural Control and Monitoring*, San Diego, CA.